FORGE

Fate Of Repository Gases

European Commission FP7

SIMULATION RESULTS OF THE HG-A TEST

FORGE Report D4.23

	Name	Organisation	Signature	Date
Compiled	J. Alcoverro	UPC		June 2013
Verified	RP Shaw	BGS		14th October 2013
Approved	RP Shaw	BGS		14th October 2013

Keywords.

Mont Terri URL; HG-A test; Opalinus Clay; Gas flow; modelling

Bibliographical reference

J. ALCOVERRO, D. ARNEDO, S. OLIVELLA, AND E.E. ALONSO. 2013. SIMULATION RESULTS OF THE HG-A TEST

FORGE Report D4.23. 75pp.

Euratom 7th Framework Programme Project: FORGE

EURATOM

Fate of repository gases (FORGE)

The multiple barrier concept is the cornerstone of all proposed schemes for underground disposal of radioactive wastes. The concept invokes a series of barriers, both engineered and natural, between the waste and the surface. Achieving this concept is the primary objective of all disposal programmes, from site appraisal and characterisation to repository design and construction. However, the performance of the repository as a whole (waste, buffer, engineering disturbed zone, host rock), and in particular its gas transport properties, are still poorly understood. Issues still to be adequately examined that relate to understanding basic processes include: dilational versus visco-capillary flow mechanisms; long-term integrity of seals, in particular gas flow along contacts; role of the EDZ as a conduit for preferential flow; laboratory to field up-scaling. Understanding gas generation and migration is thus vital in the quantitative assessment of repositories and is the focus of the research in this integrated, multi-disciplinary project. The FORGE project is a pan-European project with links to international radioactive waste management organisations, regulators and academia, specifically designed to tackle the key research issues associated with the generation and movement of repository gasses. Of particular importance are the long-term performance of bentonite buffers, plastic clays, indurated mudrocks and crystalline formations. Further experimental data are required to reduce uncertainty relating to the quantitative treatment of gas in performance assessment. FORGE will address these issues through a series of laboratory and field-scale experiments, including the development of new methods for up-scaling allowing the optimisation of concepts through detailed scenario analysis. The FORGE partners are committed to training and CPD through a broad portfolio of training opportunities and initiatives which form a significant part of the project.

Further details on the FORGE project and its outcomes can be accessed at www.FORGEproject.org.

Contact details:

J. Alcoverro, D. Arnedo, S. Olivella, E.E. Alonso

Department of Geotechnical Engineering and Geosciences

Universitat Politècnica de Catalunya

Jordi Girona 1-3

08034 Barcelona

Spain

SIMULATION RESULTS OF THE HG-A TEST

D4.23 - Final report – Simulation results (HG-A)

(Rev 1.01)

J. Alcoverro, D. Arnedo, S. Olivella, E.E. Alonso

Department of Geotechnical Engineering and Geosciences
Universitat Politècnica de Catalunya
Jordi Girona 1-3, 08034 Barcelona

TABLE OF CONTENTS

1 Introduction 2
2 Modelling approach 3
2.1 Balance equations for a porous material with two fluid phases 3
2.2 Equilibrium restrictions 5
2.3 Constitutive relations 6
2.4 Field equations 11
2.5 Transition between saturated and unsaturated states 13
2.6 Simplified approach for saturated conditions 14
3 Modelling of the tunnel excavation 16
3.1 Tunnel excavation 16
3.2 3D model 17
3.2.1 Geometry and coordinate system 17
3.2.2 Initial and boundary conditions 18
3.2.3 Material models 19
3.2.4 Calculation phases 20
3.2.5 Results 21
4 Modelling of the liquid and gas injection tests 29
4.1 Test protocols 30
4.2 2D axisymmetric model 32
4.2.1 Geometry and coordinate system 32
4.2.2 Initial and boundary conditions 34
4.2.3 Material models 36
4.2.4 Calculation phases 38
4.2.5 Calibration results 39
4.2.6 Best fit results 47
4.2.7 Additional results 55
4.3 1D simplified model 60
4.3.1 Geometry and coordinate system 60
4.3.2 Initial and boundary conditions 61
4.3.3 Material models 62
4.3.4 Calculation phases 63
4.3.5 Sensitivity analysis results 63
4.3.6 Best fit results 68
4.3.7 Comparison with 2D axisymmetric model 70
5 Conclusions 73
6 References 75

1 Introduction

The HG-A test is located in the Mont Terri Underground Rock Laboratory, near Saint Ursanne (Jura, Switzerland). It consists of a horizontal borehole of 1.00 m in diameter and 13.00 m in length excavated in the ultra-low permeable Opalinus clay. During the tunnel drilling, the Opalinus clay near the tunnel wall was damaged, giving rise to an EDZ (Excavation Damaged Zone) around the tunnel. After drilling the tunnel, the last 4.00 m at the tunnel end (the test section) were backfilled with gravel. Then, along the next 3.00 m (the megapacker section), an inflatable rubber packer, similar to those used to isolate intervals in a borehole but of 1.00 m in diameter (the megapacker), was installed and inflated, thereby compressing the EDZ that was created during the tunnel excavation. Finally, a steel liner was placed along the remaining 6.00 m close to the tunnel mouth (the liner section) in order to guarantee the tunnel stability. Then test section was filled with de-aired water and care was taken in order to eliminate the air from this tunnel section. Subsequently, a series of water and gas injection tests were carried out with varying megapacker pressure, whereby water or gas was injected into the test section and, due to the very low permeability of the intact Opalinus clay, forced to flow back along the EDZ.

The formation of the EDZ due to the tunnel excavation was modeled using a 3D finite numerical model using CODE_BRIGHT (a finite element code developed at the Geotechnical Engineering Department of the UPC), whereby an anisotropic linear elastic material coupled with a constant anisotropic intrinsic permeability was used to model the Opalinus clay. In order to model the water and gas flow through the EDZ, a two-track approach was followed. On the one hand, a 2D axisymmetric numerical model using CODE_BRIGHT was made. On the other hand, a 1D analytical-numerical model was developed and implemented in an Excel spreadsheet, whereby the field equations defined on a 1D geometrical domain were numerically solved using the finite element method. The 1D model was used to perform sensitivity analyses with respect to model parameters and helped calibrating the 2D axisymmetric model.

2 Modelling approach

The modelling approach is based in Olivella et al. (1994), and has been implemented in CODE_BRIGHT (a finite element code developed at the Geotechnical Engineering Department of the UPC). Both the Opalinus clay and the EDZ will be considered to be porous media, with a solid phase (with one species: clay), a liquid phase (with two species: water and air) and a gas phase (with two species: water and air). In principle, balance of mass, momentum and energy should be established for the various species in the various phases present in the porous medium. However, equilibrium restrictions and constitutive relations will allow dropping some of them.

Exchanges of both species water and species air between the liquid phase and the gas phase will be allowed. However, it will be assumed that they are always in equilibrium. It will be assumed that motions are slow so that terms involving accelerations and products of velocities may be neglected. Finally, it will be assumed that temperature remains constant everywhere.

Combining the balance equations, the equilibrium restrictions and the constitutive relations, we get the field equations with the solid phase displacement $\boldsymbol{u}_s$, the liquid phase pressure p_l and the gas phase pressure p_g as unknown functions of the space position and time.

2.1 Balance equations for a porous material with two fluid phases

Balance equations are general equations (independent of constitutive assumptions) stating fundamental physical principles concerning mass, momentum and energy.

- **Balance of mass**

As explained later, due to the assumption of phase change equilibrium, the balance of mass needs only be considered for the solid phase, for the species water and for the species air

$$\frac{\partial}{\partial t}\{\rho_s(1-\phi)\}+div\{\rho_s(1-\phi)\boldsymbol{v}_s\}=0 \tag{2.1}$$

$$\frac{\partial}{\partial t}\{\omega_l^w\rho_l S_l\phi+\omega_g^w\rho_g S_g\phi\}+div\{\boldsymbol{i}_l^w+\omega_l^w\rho_l\boldsymbol{q}_l+\boldsymbol{i}_g^w+\omega_g^w\rho_g\boldsymbol{q}_g+(\omega_g^w S_g\rho_g+\omega_l^w S_l\rho_l)\phi\boldsymbol{v}_s\}=0 \tag{2.2}$$

$$\frac{\partial}{\partial t}\{\omega_l^a\rho_l S_l\phi+\omega_g^a\rho_g S_g\phi\}+div\{\boldsymbol{i}_l^a+\omega_l^a\rho_l\boldsymbol{q}_l+\boldsymbol{i}_g^a+\omega_g^a\rho_g\boldsymbol{q}_g+(\omega_g^a S_g\rho_g+\omega_l^a S_l\rho_l)\phi\boldsymbol{v}_s\}=0 \tag{2.3}$$

where ρ_s is the density of the solid phase, ρ_l is the density of the liquid phase, ρ_g is the density of the gas phase, ϕ is the void ratio, S_l and S_g are the degree of saturation of the liquid phase and of the gas phase ($S_l+S_g=1$), $\boldsymbol{v}_s$ is the velocity of the solid phase, ω_l^w and ω_l^a are the mass fractions of species water and of species air in the liquid phase ($\omega_l^w+\omega_l^a=1$), ω_g^w and ω_g^a are the mass fractions of species water and of species air in the gas phase ($\omega_g^w+\omega_g^a=1$), $\boldsymbol{q}_l$ and $\boldsymbol{q}_g$ are the volume fluxes of the liquid phase and of the gas phase with respect of the solid phase ($\boldsymbol{q}_l=\phi S_l(\boldsymbol{v}_l-\boldsymbol{v}_s)$ and $\boldsymbol{q}_g=\phi S_g(\boldsymbol{v}_g-\boldsymbol{v}_s)$, where $\boldsymbol{v}_l$ and $\boldsymbol{v}_g$ are the velocities of the liquid phase and of the gas phase), $\boldsymbol{i}_l^w$ and $\boldsymbol{i}_l^a$ are the mass fluxes with respect to the liquid phase of the species water in the liquid phase and of the species air in the

liquid phase ($\boldsymbol{i}_l^w = \rho_l \omega_l^w \phi S_l (\boldsymbol{v}_l^w - \boldsymbol{v}_l)$ and $\boldsymbol{i}_l^a = \rho_l \omega_l^a \phi S_l (\boldsymbol{v}_l^a - \boldsymbol{v}_l)$, where $\boldsymbol{v}_l^w$ and $\boldsymbol{v}_l^a$ are the velocities of the species water in the liquid phase and of the species air in the liquid phase; since $\omega_l^w \boldsymbol{v}_l^w + \omega_l^w \boldsymbol{v}_l^a = \boldsymbol{v}_l$, it follows $\boldsymbol{i}_l^w + \boldsymbol{i}_l^a = \boldsymbol{0}$) and $\boldsymbol{i}_g^w$ and $\boldsymbol{i}_g^a$ are the mass fluxes with respect to the gas phase of the species water in the gas phase and of the species air in the gas phase ($\boldsymbol{i}_g^w = \rho_g \omega_g^w \phi S_g (\boldsymbol{v}_g^w - \boldsymbol{v}_g)$ and $\boldsymbol{i}_g^a = \rho_g \omega_g^a \phi S_g (\boldsymbol{v}_g^a - \boldsymbol{v}_g)$, where $\boldsymbol{v}_g^w$ and $\boldsymbol{v}_g^a$ are the velocities of the species water in the liquid phase and of the species air in the liquid phase; since $\omega_g^w \boldsymbol{v}_g^w + \omega_g^w \boldsymbol{v}_g^a = \boldsymbol{v}_g$, it follows $\boldsymbol{i}_g^w + \boldsymbol{i}_g^a = \boldsymbol{0}$).

The balance of mass of the solid phase (2.1) may be integrated, obtaining

$$J^s \rho_s (1-\phi) = \rho_s^0 (1-\phi^0), \tag{2.4}$$

where J^s is the Jacobian of the motion of the solid phase, ρ_s^0 is the density of the solid phase at the corresponding point in the reference configuration and ϕ^0 is the porosity at the corresponding point in the reference configuration. Using the relation (small strains)

$$J_s = 1 + \varepsilon_{s,vol} \tag{2.5}$$

we arrive to

$$(1+\varepsilon_{s,vol}) \rho_s (1-\phi) = \rho_s^0 (1-\phi^0). \tag{2.6}$$

Because of the assumption of equilibrium of the exchange of the species water and of the species air between the liquid phase and the gas phase, the balance of mass for the species water in the liquid phase, the balance of mass for the species air in the liquid phase, the balance of mass for the species water in the gas phase and the balance of mass for the species air in the gas phase are not needed. However, they allow calculating the mass rates of exchange of the species water and of the species air between the liquid phase and the gas phase, as shown below.

- **Balance of momentum**

If motions are slow, then the balance of momentum for the porous medium as a whole reads

$$div\, \boldsymbol{\sigma} + \rho \boldsymbol{g} = \boldsymbol{0}, \tag{2.7}$$

where $\boldsymbol{\sigma}$ is the (total) stress tensor of the porous medium, ρ is the (total) density of the porous medium ($\rho = (1-\phi)\rho_s + \phi S_l \rho_l + \phi S_g \rho_g$) and $\boldsymbol{g}$ is the gravity acceleration .

The balance of momentum for the liquid and the gas phases will be replaced by generalized Darcy's laws appropriate for unsaturated materials. These laws correspond to the balance of momentum for the liquid phase and for the gas phase and to constitutive assumptions for the stress tensors of each of these phases and for the exchange of momentum of each of these phases with the other phases. They are presented with the constitutive relations. The balance of momentum of the solid phase may be obtained by noting that the sum of the balance of momentum for the solid phase, for the liquid phase and for the gas phase is the balance of

momentum for the porous medium as a whole (2.7), whereby the assumption of slow motions is taken into account.

The balance of momentum for the species water and for the species air in the liquid phase and in the gas phase will be replaced by Fick's laws. These laws correspond to the balance of momentum for the species water and the species air in the liquid phase and in the gas phase and to constitutive assumptions for the stress tensors of the species water and the species air in the liquid phase and in the gas phase and for the exchange of momentum of each of these two species in each of these two phases with the other species in the other phases.

The sum of the balance of momentum of the species water and of the species air in the liquid phase is the balance of momentum of the liquid phase, taking into account the assumption of slow motions. Similarly, the sum of the balance of momentum of the species water and of the species air in the gas phase is the balance of momentum in the gas phase, taking into account the assumption of slow motions.

- **Balance of energy**

Because of the assumption that temperature is everywhere constant, the various balances of energy are not needed.

2.2 Equilibrium restrictions

The processes considered are restricted by certain constraints placed on some variables of the porous medium implied by the assumption of slow motions. The equilibrium conditions considered are: mechanical equilibrium, thermal equilibrium and phase change equilibrium.

- **Mechanical equilibrium**

Due to the assumption of slow motion, inertial terms and terms involving the product of velocities are neglected in the balance of momentum equations.

- **Thermal equilibrium**

We assume that the exchanges of energy between the various species in the various phases are much faster than the evolution of the porous medium, thereby implying that at any space point and time instant their temperatures are equal. Furthermore, we assume that the evolution of the porous medium takes places under isothermal conditions.

- **Phase change equilibrium**

We assume that species water and species air are in equilibrium with respect to phase changes between the liquid phase and the gas phase. In this regard, we will assume that the psychrometric law and Henry's law hold

$$\omega_g^w \rho_g = p_{g0}^w(T) \frac{M_w}{R(273.15+T)} \exp\left(\frac{-(p_g - p_l)M_w}{R(273.15+T)\rho_l} \right) \quad \text{and} \tag{2.8}$$

$$\omega_l^a = (\omega_g^a \rho_g) \frac{R(273.15+T)}{HM_w}, \tag{2.9}$$

where $M_w = 0.018\,kg/mol$ is the molar mass of water, $M_a = 0.02895\,kg/mol$ is the molar mass of air, $R = 8.3144521\times10^{-6}\,MPa\cdot m^3/(°K\cdot mol)$ is the ideal gases constant, T is the temperature in °C, $H = 10^4\,MPa$ is Henry's constant and $p_{g0}^w(T)$ is the water vapour pressure in equilibrium with liquid water through a planar surface, whose expression has been taken to be

$$p_{g0}^w(T) = 136075\exp\left(\frac{-5239.7}{273.15+T}\right), \tag{2.10}$$

where $p_{g0}^w(T)$ is in MPa and T is in °C.

Due to the assumed phase change equilibrium, the exchanges of the species water and of the species air between the liquid phase and the gas phase may be computed by establishing the balances of mass of species water in the liquid phase, the balance of species air in the liquid phase, the balance of species water in the gas phase and the balance of species air in the gas phase

$$\frac{\partial}{\partial t}\{\omega_l^w\rho_l S_l\phi\} + div\{\boldsymbol{i}_l^w + \omega_l^w\rho_l\boldsymbol{q}_l + \omega_l^w S_l\rho_l\phi\boldsymbol{v}_s\} = f_l^w, \tag{2.11}$$

$$\frac{\partial}{\partial t}\{\omega_g^w\rho_g S_g\phi\} + div\{\boldsymbol{i}_g^w + \omega_g^w\rho_g\boldsymbol{q}_g + \omega_g^w S_g\rho_g\phi\boldsymbol{v}_s\} = f_g^w, \tag{2.12}$$

$$\frac{\partial}{\partial t}\{\omega_l^a\rho_l S_l\phi\} + div\{\boldsymbol{i}_l^a + \omega_l^a\rho_l\boldsymbol{q}_l + \omega_l^a S_l\rho_l\phi\boldsymbol{v}_s\} = f_l^a \quad \text{and} \tag{2.13}$$

$$\frac{\partial}{\partial t}\{\omega_g^a\rho_g S_g\phi\} + div\{\boldsymbol{i}_g^a + \omega_g^a\rho_g\boldsymbol{q}_g + \omega_g^a S_g\rho_g\phi\boldsymbol{v}_s\} = f_g^a, \tag{2.14}$$

where f_l^w and f_g^w are the mass rates of species water being converted to the liquid and gas phases (equations (2.11), (2.13) and the balance of the species water (2.2) imply $f_l^w + f_g^w = 0$) and f_l^a and f_g^a are the mass rates of species air being converted to the liquid and gas phases (equations (2.12), (2.14) and the balance of the species air (2.3) imply $f_l^a + f_g^a = 0$).

2.3 Constitutive relations

Constitutive relations characterize the material properties of the components of the considered porous medium as well as their interactions.

- **Constitutive relations for the porous medium**

The water retention curve determines the degree of saturation S_l of the porous medium as a function of the pressure of the liquid phase p_l and the pressure of the gas phase p_g. We have used van Genuchten's water retention curve

$$S_l = \begin{cases} \left(1+\left(\dfrac{p_g - p_l}{P_0}\right)^{\frac{1}{1-\lambda}}\right)^{-\lambda} & p_g > p_l \\ 1 & p_g \le p_l \end{cases}, \tag{2.15}$$

where λ ($0<\lambda<1$) is a model parameter and P_0 ($P_0>0$) depends on the intrinsic permeability tensor $\boldsymbol{k}$ according to the expression

$$P_0 = \frac{C}{\sqrt[3]{k}}, \tag{2.16}$$

where k is the maximum of the eigenvalues of the intrinsic permeability tensor $\boldsymbol{k}$ and C ($C>0$) is a constant. In order to determine this constant, we use the expression

$$C = P_{0\,matrix}\sqrt[3]{k_{matrix}}, \tag{2.17}$$

where $P_{0\,matrix}$ and k_{matrix} are the values of P_0 and k for the matrix of the material, that is, without cracks (see equation (2.24) below).

We use a generalization of Darcy's law to unsaturated conditions for the motion of the liquid and gas phases with respect to the solid phase.

$$\boldsymbol{q}_l = -\frac{k_{rl}(S_l)\boldsymbol{k}(\varepsilon_{vol})}{\mu_l}\, grad(p_l) - \rho_l \boldsymbol{g} \quad \text{and} \tag{2.18}$$

$$\boldsymbol{q}_g = -\frac{k_{rg}(S_g)\boldsymbol{k}(\varepsilon_{vol})}{\mu_g}\left[grad(p_g) - \rho_g \boldsymbol{g}\right], \tag{2.19}$$

where $\boldsymbol{k}(\varepsilon_{vol})$ is the intrinsic permeability tensor, $k_{rl}(S_l)$ is the relative permeability of the liquid phase and $k_{rg}(S_g)$ is the relative permeability of the gas phase.

The relative permeability of the liquid phase is given by one of the following laws

$$k_{rl}(S_l) = S_l^{1/2}\left[1-(1-S_l^{1/\lambda_l})^{\lambda_l}\right]^2 \quad \text{(Van Genuchten's law) or} \tag{2.20}$$

$$k_{rl}(S_l) = A_l S_l^{n_l} \quad \text{(generalised power law),} \tag{2.21}$$

where λ_l, n_l and A_l are model parameters. The relative permeability of the gas phase is given by the following law

$$k_{rg}(S_g) = A_g S_g^{n_g} \quad \text{(generalised power law),} \tag{2.22}$$

where n_g and A_g are model parameters.

The intrinsic permeability tensor $\boldsymbol{k}(\varepsilon_{vol})$ is given by one of the following laws

$$\boldsymbol{k}(\varepsilon_{vol}) = \boldsymbol{k} \qquad \text{(constant) or} \tag{2.23}$$

$$\boldsymbol{k}(\varepsilon_{vol}) = \boldsymbol{k}_{matrix} + \frac{1}{12a}[b(\varepsilon_{vol})]^3 \boldsymbol{I} \qquad \text{(deformation-dependent, Olivella et al. (2008)).} \tag{2.24}$$

In the first law, $\boldsymbol{k}$ is the intrinsic permeability tensor such that, at a given space point, remains constant. In the second law, the intrinsic permeability tensor is the sum of the contribution from the matrix (uniform flow) and an isotropic contribution from the cracks (Poiseuille flow depending on the crack aperture), where $\boldsymbol{k}_{matrix}$ is the matrix intrinsic permeability tensor such that, at a given space point, remains constant, $\boldsymbol{I}$ is the identity tensor, a is the mean spacing between cracks and $b(\varepsilon_{vol})$ denotes the crack aperture as a function of ε_{vol} defined by

$$b(\varepsilon_{vol}) = \begin{cases} b_0 & \varepsilon_{vol} \le \varepsilon_{vol0} \\ b_0 + (\varepsilon_{vol} - \varepsilon_{vol0})a & \varepsilon_{vol0} \le \varepsilon_{vol} \le \varepsilon_{vol0} + (b_{max} - b_0)/a \\ b_{max} & \varepsilon_{vol0} + (b_{max} - b_0)/a \le \varepsilon_{vol} \end{cases} \tag{2.25}$$

where ε_{vol0} is the volumetric deformation at which the crack aperture starts increasing, b_0 is the minimum crack aperture, b_{max} is the maximum crack aperture and a is the mean spacing between cracks. Note that, if $b_0 = 0$ and $b_{max} = 0$, then $b(\varepsilon_{vol}) = 0$ and the second law reduces to the first law with $\boldsymbol{k} = \boldsymbol{k}_{matrix}$.

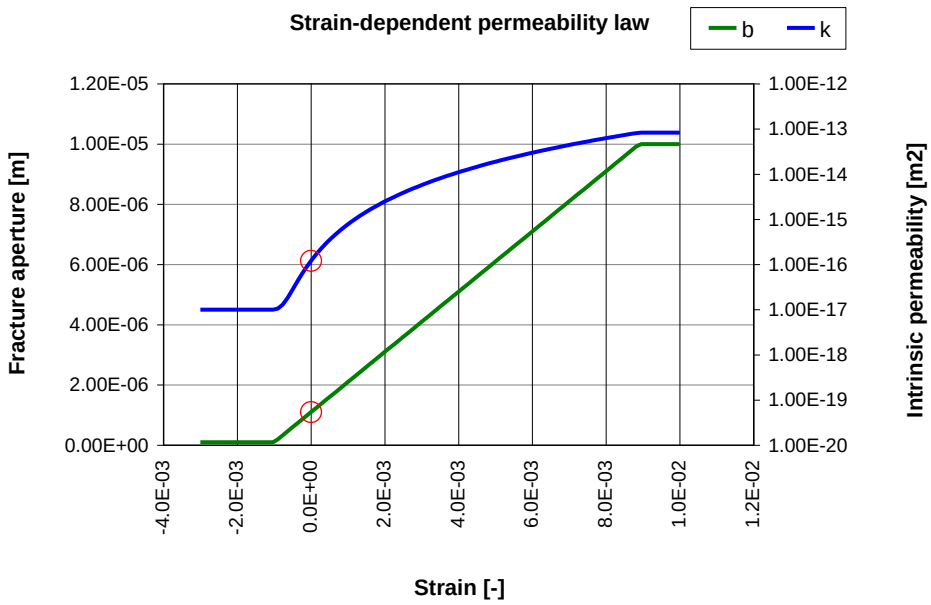

Figure 2-1. Crack aperture (left vertical axis) and intrinsic permeability (right vertical axis, logarithmic scale) as functions of volumetric deformation ($\boldsymbol{k}_{matrix} = 10^{-17}\boldsymbol{I}\, m^2$, $b_0 = 10^{-7} m$, $b_{\max} = 10^{-5} m$, $a = 10^{-3} m$, $\varepsilon_{vol0} = -10^{-3}$). Circles indicate the initial state, at $\varepsilon = 0$.

The dependency of the intrinsic permeability on the crack aperture, which is related to the volumetric deformation of the porous medium, is very important for the modelling of the HG-A test. Figure 2-1 shows an example of the dependency of the intrinsic permeability (in logarithmic scale) and of the crack aperture with the volumetric deformation, whereby the parameters have values suitable for the HG-A test. Note the large variations in the intrinsic permeability induced by the volumetric deformations.

Finally, we use Fick's law for the motion of the water and air species with respect to the liquid and gas phases.

$$\boldsymbol{i}_l^w = -\rho_l(\phi S_l D_l^w \boldsymbol{I} + \boldsymbol{D}_l')grad(\omega_l^w) \quad \text{(negligible term with respect to conduction)} \tag{2.26}$$

$$\boldsymbol{i}_l^a = -\rho_l(\phi S_l D_l^a \boldsymbol{I} + \boldsymbol{D}_l')grad(\omega_l^a) \quad \text{(important term)} \tag{2.27}$$

$$\boldsymbol{i}_g^w = -\rho_g(\phi S_g D_g^w \boldsymbol{I} + \boldsymbol{D}_g')grad(\omega_g^w) \tag{2.28}$$

$$\boldsymbol{i}_g^a = -\rho_g(\phi S_g D_g^a \boldsymbol{I} + \boldsymbol{D}_g')grad(\omega_g^a), \tag{2.29}$$

where the diffusion coefficients of the water species in the liquid and gas phases are given by

$$D_l^w = D_l^a = D_l \exp\left(\frac{-Q_l}{R(273.15+T)}\right) \tag{2.30}$$

$$D_g^w = D_g^a = D_g \frac{(273.15+T)^{Q_g}}{p_g} \tag{2.31}$$

where D_l and Q_l (resp. D_g and Q_g) are model parameters for the liquid (resp. gas) phase and the dispersion tensors are given by

$$\boldsymbol{D}_l' = d_l^t\,|\boldsymbol{q}_l|\,\boldsymbol{I} + (d_l^l - d_l^t)\frac{1}{|\boldsymbol{q}_l|}\boldsymbol{q}_l \otimes \boldsymbol{q}_l \quad \text{(in 1D flow, } \boldsymbol{D}_l'\boldsymbol{e}_z = d_l^l\,|\boldsymbol{q}_l|\,\boldsymbol{e}_z\text{)} \tag{2.32}$$

$$\boldsymbol{D}_g' = d_g^t\,|\boldsymbol{q}_g|\,\boldsymbol{I} + (d_g^l - d_g^t)\frac{1}{|\boldsymbol{q}_g|}\boldsymbol{q}_g \otimes \boldsymbol{q}_g, \quad \text{(in 1D flow, } \boldsymbol{D}_g'\boldsymbol{e}_z = d_g^l\,|\boldsymbol{q}_g|\,\boldsymbol{e}_z\text{)} \tag{2.33}$$

where d_l^l and d_l^t (resp. d_g^l and d_g^t) are the longitudinal and transversal dispersivity coefficients of the liquid (resp. gas) phase.

- **Constitutive relations for the solid phase**

It has been assumed that the solid phase has only one species. The solid phase has been assumed to be incompressible

$$\rho_s = const\,. \tag{2.34}$$

- **Constitutive relations for the liquid phase**

The liquid phase has also been assumed to be a mixture of two species (liquid water and dissolved air). However, their properties have been assumed to be independent of the amount of dissolved air.

$$\rho_l(T) = 1002.6\exp(4.5\times10^{-5}(p_l - 0.1) - 3.4\times10^{-4}T) \tag{2.35}$$

$$\mu_l(T) = 2.1\times10^{-12}\exp(1808.5/(273.15+T)) \tag{2.36}$$

where ρ_l is in kg/m^3 , $\mu_l(T)$ is in MPa·s p_l is in MPa and T is in °C.

- **Constitutive relations for the gas phase**

The gas phase has been assumed to be a mixture of two species (water vapour and dry air). It has been assumed that each species (water vapour and dry air) is an ideal gas and that Dalton's law holds.

$$\mu_g(T) = 1.48\times10^{-12}\sqrt{(273.15+T)/(1+119/(273.15+T))} \tag{2.37}$$

$$p_g = p_g^a + p_g^w \qquad \text{Dalton's law} \tag{2.38}$$

$$p_g^a = \omega_g^a \rho_g \frac{R(273.15+T)}{M_a} \qquad \text{ideal gas law for dry air} \tag{2.39}$$

$$p_g^w = \omega_g^w \rho_g \frac{R(273.15+T)}{M_w} \qquad \text{ideal gas law for water vapour} \tag{2.40}$$

where $\mu_g(T)$ is in MPa·s and T is in °C.

- **Constitutive relations for the solid skeleton**

Finally, we will also assume that a generalized form of Terzaghi's effective stress principle holds and the deformation stress tensor of the solid phase $\boldsymbol{\varepsilon}$ depends on the total stress tensor $\boldsymbol{\sigma}$, the liquid phase pressure p_l and the gas phase pressure p_g through the effective stress tensor $\boldsymbol{\sigma}'$ defined (using the continuum mechanics sign convention) by the expression.

$$\boldsymbol{\sigma}' = \boldsymbol{\sigma} + p^* \boldsymbol{I}, \tag{2.41}$$

where the effective fluid pressure p^* is defined by

$$p^* = \max(p_l, p_g). \tag{2.42}$$

For the solid skeleton, we will assume isotropic linear poroelasticity or cross-anisotropic linear poroelasticity. In both cases, at a given point, their properties (elastic moduli and orientation of the isotropy plane) remain constant.

For isotropic linear poroelasticiy, using a Cartesian coordinate system, the components of the strain tensor ε_{ij} and of the variation of the effective stress tensor $\Delta\sigma'_{ij}$ are related by the following expressions

$$\begin{aligned}
\varepsilon_{11} &= +\frac{1}{E'}\Delta\sigma'_{11} - \frac{\nu'}{E'}\Delta\sigma'_{22} - \frac{\nu'}{E'}\Delta\sigma'_{33} & \varepsilon_{12} &= \frac{(1+\nu')}{E'}\Delta\sigma'_{12} \\
\varepsilon_{22} &= -\frac{\nu'}{E'}\Delta\sigma'_{11} + \frac{1}{E'}\Delta\sigma'_{22} - \frac{\nu'}{E'}\Delta\sigma'_{33} & \varepsilon_{23} &= \frac{(1+\nu')}{E'}\Delta\sigma'_{23} \\
\varepsilon_{33} &= -\frac{\nu'}{E'}\Delta\sigma'_{11} - \frac{\nu'}{E'}\Delta\sigma'_{22} + \frac{1}{E'}\Delta\sigma'_{33} & \varepsilon_{31} &= \frac{(1+\nu')}{E'}\Delta\sigma'_{31}
\end{aligned} \tag{2.43}$$

where E' is the effective Young's modulus and ν' is the effective Poisson's ratio.

For cross-anisotropic linear poroelasticity, using a Cartesian coordinate system oriented so that direction 3 is orthogonal to the isotropy plane, the components of the strain tensor ε_{ij} and of the variation of the effective stress tensor $\Delta\sigma'_{ij}$ are related by the following expressions

$$\begin{aligned}
\varepsilon_{11} &= +\frac{1}{E'_{\|}}\Delta\sigma'_{11} - \frac{\nu'_{\|}}{E'_{\|}}\Delta\sigma'_{22} - \frac{\nu'_{\|\perp}}{E'_{\perp}}\Delta\sigma'_{33} & \varepsilon_{12} &= \frac{(1+\nu'_{\|})}{E'_{\|}}\Delta\sigma'_{12} \\
\varepsilon_{22} &= -\frac{\nu'_{\|}}{E'_{\|}}\Delta\sigma'_{11} + \frac{1}{E'_{\|}}\Delta\sigma'_{22} - \frac{\nu'_{\|\perp}}{E'_{\perp}}\Delta\sigma'_{33} & \varepsilon_{23} &= \frac{1}{2G_{\|\perp}}\Delta\sigma'_{23} \\
\varepsilon_{33} &= -\frac{\nu'_{\|\perp}}{E'_{\perp}}\Delta\sigma'_{11} - \frac{\nu'_{\|\perp}}{E'_{\perp}}\Delta\sigma'_{22} + \frac{1}{E'_{\perp}}\Delta\sigma'_{33} & \varepsilon_{31} &= \frac{1}{2G_{\|\perp}}\Delta\sigma'_{31}
\end{aligned} \tag{2.44}$$

where $E'_{\|}$, $\nu'_{\|}$, $E'_{\perp}$, $\nu'_{\|\perp}$ and $G_{\|\perp}$ are 5 effective elastic moduli, whose meaning follows from the above relations. Note that, if $E'_{\|} = E'$, $E'_{\perp} = E'$, $\nu'_{\|} = \nu'$, $\nu'_{\|\perp} = \nu'$ and $G_{\|\perp} = E'/[2(1+\nu')]$, then these relations reduce to the relations for isotropic linear poroelasticity.

2.4 Field equations

Combining the balance equations, the equilibrium restrictions and the constitutive relations we get a system of differential equations with the displacement vector of the solid skeleton $\boldsymbol{u}_s$, the pressure of the liquid phase p_l and the pressure of the gas phase p_g as unknown functions of the space position and time.

The balance of mass of the solid phase (using $\rho_s = const$) and the balance of water mass read

$$\frac{\partial\phi}{\partial t} + div(\phi\boldsymbol{v}_s) = div(\boldsymbol{v}_s) \tag{2.45}$$

$$\begin{aligned}
&\phi\frac{\partial}{\partial t}(\omega_l^w\rho_l S_l + \omega_g^w\rho_g S_g) + (\omega_l^w\rho_l S_l + \omega_g^w\rho_g S_g)\frac{\partial\phi}{\partial t} + div(\boldsymbol{i}_l^w + \omega_l^w\rho_l\boldsymbol{q}_l + \boldsymbol{i}_g^w + \omega_g^w\rho_g\boldsymbol{q}_g) \\
&\quad + (\omega_g^w S_g\rho_g + \omega_l^w S_l\rho_l)div(\phi\boldsymbol{v}_s) + (\phi\boldsymbol{v}_s)grad(\omega_g^w S_g\rho_g + \omega_l^w S_l\rho_l) = 0
\end{aligned} \tag{2.46}$$

Combining these equations, we get

$$\phi\left\{\frac{\partial}{\partial t}(\omega_l^w\rho_l S_l+\omega_g^w\rho_g S_g)+\boldsymbol{v}_s grad(\omega_l^w\rho_l S_l+\omega_g^w\rho_g S_g)\right\}+ \\ +(\omega_l^w\rho_l S_l+\omega_g^w\rho_g S_g)div(\boldsymbol{v}_s)+div(\boldsymbol{i}_l^w+\omega_l^w\rho_l\boldsymbol{q}_l+\boldsymbol{i}_g^w+\omega_g^w\rho_g\boldsymbol{q}_g)=0 \tag{2.47}$$

Neglecting the second term and using the relation (small strains)

$$div(\boldsymbol{v}_s)=\frac{\partial\varepsilon_{s,vol}}{\partial t} \tag{2.48}$$

we arrive to

$$\phi\frac{\partial}{\partial t}(\omega_l^w\rho_l S_l+\omega_g^w\rho_g S_g)+(\omega_l^w\rho_l S_l+\omega_g^w\rho_g S_g)\frac{\partial\varepsilon_{s,vol}}{\partial t} \\ +div(\boldsymbol{i}_l^w+\omega_l^w\rho_l\boldsymbol{q}_l+\boldsymbol{i}_g^w+\omega_g^w\rho_g\boldsymbol{q}_g)=0 \tag{2.49}$$

Similarly, the balance of mass of the solid phase (using $\rho_s=const$) and the balance of air mass, yield

$$\phi\frac{\partial}{\partial t}(\omega_l^a\rho_l S_l+\omega_g^a\rho_g S_g)+(\omega_l^a\rho_l S_l+\omega_g^a\rho_g S_g)\frac{\partial\varepsilon_{s,vol}}{\partial t} \\ +div(\boldsymbol{i}_l^a+\omega_l^a\rho_l\boldsymbol{q}_l+\boldsymbol{i}_g^a+\omega_g^a\rho_g\boldsymbol{q}_g)=0 \tag{2.50}$$

On the other hand, using $\rho_s=const$ in the integrated form (2.6) of the balance of mass of the solid phase, we arrive to

$$1-\phi=\frac{1-\phi^0}{1+\varepsilon_{s,vol}}. \tag{2.51}$$

This relation allows to express the porosity ϕ as a function of the derivatives of the displacement vector of the solid phase $\boldsymbol{u}_s$.

Therefore, upon using the rest of the balance equations, the equilibrium restrictions and the constitutive relations, the balance of mass of the species water, the balance of mass of the species air and the balance of momentum of the porous medium

$$\phi\frac{\partial}{\partial t}(\omega_l^w\rho_l S_l+\omega_g^w\rho_g S_g)+(\omega_l^w\rho_l S_l+\omega_g^w\rho_g S_g)\frac{\partial\varepsilon_{s,vol}}{\partial t} \\ +div(\boldsymbol{i}_l^w+\omega_l^w\rho_l\boldsymbol{q}_l+\boldsymbol{i}_g^w+\omega_g^w\rho_g\boldsymbol{q}_g)=0 \tag{2.52}$$

$$\phi\frac{\partial}{\partial t}(\omega_l^a\rho_l S_l+\omega_g^a\rho_g S_g)+(\omega_l^a\rho_l S_l+\omega_g^a\rho_g S_g)\frac{\partial\varepsilon_{s,vol}}{\partial t} \\ +div(\boldsymbol{i}_l^a+\omega_l^a\rho_l\boldsymbol{q}_l+\boldsymbol{i}_g^a+\omega_g^a\rho_g\boldsymbol{q}_g)=0 \tag{2.53}$$

$$div(\boldsymbol{\sigma}'-p*\boldsymbol{I})+\rho\boldsymbol{g}=\boldsymbol{0}, \tag{2.54}$$

may be written in terms of the displacement vector of the solid skeleton $\boldsymbol{u}_s$, the pressure of the liquid phase p_l and the pressure of the gas phase p_g and their partial derivatives.

This system of differential equations in the unknown functions $\boldsymbol{u}_s$, p_l and p_g will be referred to as the system of field equations. In order to solve this system of differential equations, suitable initial and boundary conditions reflecting the conditions of the HG-A test must be provided. Once the unknown functions are determined as a function of the space point and of time, all the functions of interest are found from them.

2.5 Transition between saturated and unsaturated states

As already mentioned, the unknown functions $\boldsymbol{u}_s$, p_l and p_g are defined at every point of the geometric domain and at all times and are found by solving the system of field equations with suitable initial and boundary conditions.

On the other hand, using the psychrometric law and Henry's law as equilibrium restrictions (stating the phase change equilibrium of water species and of air species between the gas phase and the liquid phase made of these two species), the ideal gases law for the water vapor, the ideal gases law for dry air and Dalton's law, it is possible to express p_g, ρ_g, ω_g^w and ω_g^a as a function of p_l, ρ_l, ω_l^w and ω_l^a or, conversely, to express p_l, ρ_l, ω_l^w and ω_l^a as a function of p_g, ρ_g, ω_g^w and ω_g^a.

We note that the water retention curve is a continuous function $S_l = f(p_g - p_l)$ such that $S_l = 1$ (saturated state) if and only if $p_g \le p_l$ and $S_l < 1$ if and only if $p_g > p_l$. This has the following consequences

- **Mechanical.** The effective fluid pressure $p^* = f(p_l, p_g)$ is a continuous function of p_l and p_g, such that $p^* = p_l$ if and only if $p_g \le p_l$ and $p^* = p_g$ if and only if $p_g \ge p_l$. Consequently, the effective stress tensor $\boldsymbol{\sigma}'$ is Terzaghi's effective stress tensor $\boldsymbol{\sigma} + p_l \boldsymbol{I}$ if and only if $p_g \le p_l$ and is the net stress tensor $\boldsymbol{\sigma} + p_g \boldsymbol{I}$ if and only if $p_g \ge p_l$.

- **Hydraulic.** The relative permeability of the gas phase is a continuous function $k_{rg} = f(1 - S_l)$ of S_l such that $k_{rg} = 0$ if and only if $S_l = 1$. If $S_l = 1$, then Darcy's law for the gas phase yields $\boldsymbol{q}_g = \boldsymbol{0}$. The mechanical dispersion tensor of the gas phase is a continuous function $\boldsymbol{D'}_g = f \ \boldsymbol{q}_g$ such that $\boldsymbol{D'}_g = \boldsymbol{0}$ when $\boldsymbol{q}_g = \boldsymbol{0}$. Finally, if $\boldsymbol{q}_g = \boldsymbol{0}$ then Fick's law for the water species and for the air species in the gas phase yield $\boldsymbol{i}_g^w = \boldsymbol{0}$ and $\boldsymbol{i}_g^a = \boldsymbol{0}$. Consequently, if $p_g \le p_l$ then $S_g = 0$ and $\boldsymbol{q}_g = \boldsymbol{i}_g^w = \boldsymbol{i}_g^a = \boldsymbol{0}$. In this case, all terms pertaining to the gas phase disappear from the balance of mass equations.

The water retention curve determines whether the porous medium is saturated or unsaturated, but in the field equations some terms vanish if the porous medium is saturated. More precisely

- **Saturated porous medium.** If $p_g \le p_l$, then the porous medium saturates ($S_l = 1$) and the terms $\boldsymbol{q}_g$, $\boldsymbol{i}_g^w$ and $\boldsymbol{i}_g^a$ disappear from the field equations, which reduce to the field equations of a saturated porous medium (recall that the liquid phase is made of the species water and the species air) with $\boldsymbol{\sigma}' = \boldsymbol{\sigma} + p_l \boldsymbol{I}$ being Terzaghi's effective stress

$$\phi \frac{\partial}{\partial t}(\omega_l^w \rho_l) + (\omega_l^w \rho_l)\frac{\partial \varepsilon_{s,vol}}{\partial t} + div(\boldsymbol{i}_l^w + \omega_l^w \rho_l \boldsymbol{q}_l) = 0 \tag{2.55}$$

$$\phi \frac{\partial}{\partial t}(\omega_l^a \rho_l) + (\omega_l^a \rho_l S_l)\frac{\partial \varepsilon_{s,vol}}{\partial t} + div(\boldsymbol{i}_l^a + \omega_l^a \rho_l \boldsymbol{q}_l) = 0 \tag{2.56}$$

$$div(\boldsymbol{\sigma}' - p_l \boldsymbol{I}) + \rho \boldsymbol{g} = \boldsymbol{0} \tag{2.57}$$

Using (2.11) and (2.13) in the two first equations, it follows that $f_l^w = 0$ and $f_l^a = 0$. That is, there are no mass contributions from the non-existent gas phase. As explained earlier, the pressure of the gas phase p_g at a point of the porous medium and at a time instant is the pressure of a gas (made of species water and species air) which is in equilibrium (with respect to exchanges of species water and of species air) with the liquid phase (made of species water and species air) at the considered point of the porous medium and at the considered time instant.

- **Unsaturated porous medium.** If $p_g > p_l$, then the porous medium desaturates ($S_l < 1$), the terms $\boldsymbol{q}_g$, $\boldsymbol{i}_g^w$ and $\boldsymbol{i}_g^a$ appear in the field equations, which are the field equations of an unsaturated porous medium (the liquid phase and the gas phase have the species water and the species air) with $\boldsymbol{\sigma}' = \boldsymbol{\sigma} + p_g \boldsymbol{I}$ being the net stress

$$\begin{aligned}\phi \frac{\partial}{\partial t}(\omega_l^w \rho_l S_l + \omega_g^w \rho_g S_g) + (\omega_l^w \rho_l S_l + \omega_g^w \rho_g S_g)\frac{\partial \varepsilon_{s,vol}}{\partial t} \\ + div(\boldsymbol{i}_l^w + \omega_l^w \rho_l \boldsymbol{q}_l + \boldsymbol{i}_g^w + \omega_g^w \rho_g \boldsymbol{q}_g) = 0\end{aligned} \tag{2.58}$$

$$\begin{aligned}\phi \frac{\partial}{\partial t}(\omega_l^a \rho_l S_l + \omega_g^a \rho_g S_g) + (\omega_l^a \rho_l S_l + \omega_g^a \rho_g S_g)\frac{\partial \varepsilon_{s,vol}}{\partial t} \\ + div(\boldsymbol{i}_l^a + \omega_l^a \rho_l \boldsymbol{q}_l + \boldsymbol{i}_g^a + \omega_g^a \rho_g \boldsymbol{q}_g) = 0\end{aligned} \tag{2.59}$$

$$div(\boldsymbol{\sigma}' - p_g \boldsymbol{I}) + \rho \boldsymbol{g} = \boldsymbol{0}\,. \tag{2.60}$$

2.6 Simplified approach for saturated conditions

If we have reasons to believe that in the domain of the problem to be solved all points remain saturated, it is possible to simplify the set of field equations of the general approach: we drop the balance of mass of species air and, in the remaining filed equations, we set $p_g = p_g^{const}$ (p_g^{const} is a constant value), $\omega_l^a = 0$, $\omega_l^w = 1$ (there is no dissolved air in the liquid phase and Fick's laws yield $\boldsymbol{i}_l^w = \boldsymbol{i}_l^a = \boldsymbol{0}$) and $\omega_g^a = 1$, $\omega_g^w = 0$ (there is no water vapour in the gas phase and Fick's laws yield $\boldsymbol{i}_l^w = \boldsymbol{i}_l^a = \boldsymbol{0}$). Therefore, the field equations reduce to

$$\phi \frac{\partial}{\partial t}(\rho_l S_l) + (\rho_l S_l)\frac{\partial \varepsilon_{s,vol}}{\partial t} + div(\rho_l \boldsymbol{q}_l) = 0 \tag{2.61}$$

$$div(\boldsymbol{\sigma}' - p * \boldsymbol{I}) + \rho \boldsymbol{g} = \boldsymbol{0} \tag{2.62}$$

and the unknown functions of space and time are the displacement vector of the solid skeleton $\boldsymbol{u}_s$ and the pressure of the liquid phase p_l. In saturated conditions these equations reduce to

$$\phi \frac{\partial \rho_l}{\partial t} + \rho_l \frac{\partial \varepsilon_{s,vol}}{\partial t} + div(\rho_l \boldsymbol{q}_l) = 0 \tag{2.63}$$

$$div(\boldsymbol{\sigma}' - p_l \boldsymbol{I}) + \rho \boldsymbol{g} = \boldsymbol{0} \tag{2.64}$$

Comparing these equations with the corresponding ones of the general approach in saturated conditions, we see that they correspond to neglect the dissolved air (i.e. $\omega_l^w = 1$ and $\boldsymbol{i}_l^w = \boldsymbol{0}$) in those equations. Note that, if the constant value p_g^{const} is chosen appropriately (for instance, the atmospheric pressure), and at some point the solution of the field equations of the simplified approach for saturated conditions is such that $p_l < p_g^{const}$, then the considered water retention curve implies that desaturation occurs and this is an indication that the hypothesis of saturation does not hold at that point.

3 Modelling of the tunnel excavation

The goal was to simulate the excavation process of the HG-A tunnel, including the formation of the EDZ. In view of the presence of bedding planes in the Opalinus clay, a cross-anisotropic linear poroelastic model with a cross-anisotropic intrinsic permeability was used for the solid skeleton, whereby in both cases the isotropy planes were parallel to the bedding planes. Although the cross-anisotropic linear poroelastic model cannot reproduce the formation of the EDZ, it is believed that the distribution of effective stresses and deformations will give indications of where it will form.

Since the bedding planes of the host Opalinus clay have a strike line parallel to the tunnel axis, a 3D model was used, in which gravity was also taken into account. On the other hand, in view of the very low permeability of the Opalinus clay and the short period in which the tunnel was excavated, saturated conditions were assumed. Furthermore, isothermal conditions were also assumed.

The assumption of saturated conditions was implemented by using the simplified approach for saturated conditions, whereby, as explained earlier, the field equation corresponding to the balance of mass of species air was dropped and the following settings were made $p_g = p_g^{const}$ (we used $p_g^{const} = 0.1\ \text{MPa}$), $\omega_l^a = 0$, $\omega_l^w = 1$ (no dissolved air in the liquid phase; Fick's laws yield $\boldsymbol{i}_l^w = \boldsymbol{i}_l^a = \mathbf{0}$) and $\omega_g^a = 1$, $\omega_g^w = 0$ (no water vapour in the gas phase; Fick's laws yield $\boldsymbol{i}_l^w = \boldsymbol{i}_l^a = \mathbf{0}$). Therefore, the displacement vector of the solid skeleton $\boldsymbol{u}_s$ and the pressure of the liquid phase p_l were the unknown functions of space and time to be determined.

3.1 Tunnel excavation

The tunnel is 13.0 m long, 1.0 m in diameter and was excavated in 7 days using an auger rig, as shown in Figure 3-1. As already mentioned, because of the low permeability of the Opalinus clay and the fast excavation rate, the assumption of saturated conditions was adopted. The tunnel excavation induced rapid changes in both (total) stresses and liquid phase pressures. Due to the dissipation of the excess liquid phase pressures generated during the excavation, the effective stresses evolved with time, thereby inducing changes in the displacement field of the solid skeleton.

Figure 3-1. Excavation of the microtunnel with an auger rig, Trick et al. (2007).

3.2 3D model

A 3D model was prepared using CODE_BRIGHT and assuming saturated and isothermal conditions. After setting the initial and boundary conditions, the tunnel excavation and the subsequent generation and dissipation of excess liquid phase pressures were simulated.

3.2.1 Geometry and coordinate system

The zone modelled was an orthogonal prism 18.0 m long with a square base 10.0 m × 10.0 m, as shown in Figure 3-2. The tunnel axis passed through the centres of the square bases, and the tunnel mouth was on one of the square bases. With these dimensions, the 5 faces of the prism that do not contain the tunnel mouth were at 8.5 diameters from the tunnel lateral wall and from the tunnel end vertical wall, allowing to consider the boundary conditions on those 5 five faces as remote. Also shown in Figure 3-2 is the finite element mesh, which was made of 8-noded linear hexahedra with selective integration. In total, there were 17712 elements and 18685 nodes.

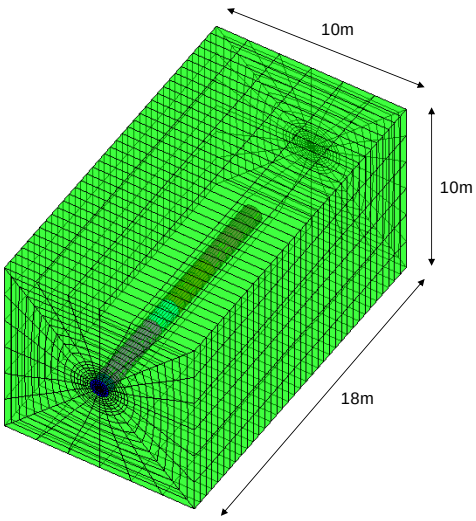

Figure 3-2. Modelled zone, system of coordinates and finite element mesh.

3.2.2 Initial and boundary conditions

The initial porosity of the Opalinus clay was assumed to be constant $\phi^0 = 0.14$. The initial displacements were zero $u_x^0 = 0.0\,m$, $u_y^0 = 0.0\,m$, $u_z^0 = 0.0\,m$. The initial liquid phase pressure and stresses fields were computed by prescribing boundary conditions and using a calculation phase in order to reach mechanical and hydraulic equilibrium.

Concerning the mechanical boundary conditions, the faces of the finite element mesh were assumed to be orthogonal to the principal directions of the in situ stress field. The figure below shows the in situ stress field and the applied boundary conditions. Constant total tractions orthogonal to three faces of the mesh were applied and the displacements orthogonal to the three opposite faces were prescribed to be zero. The values used for the in situ stress field were chosen according to the available measurements.

Concerning the hydraulic boundary conditions, hydrostatic conditions were assumed. The figure below shows the applied liquid phase pressures. They were constant on horizontal planes and varied linearly with depth. The values used for the liquid phase pressure field were chosen according to the available measurements.

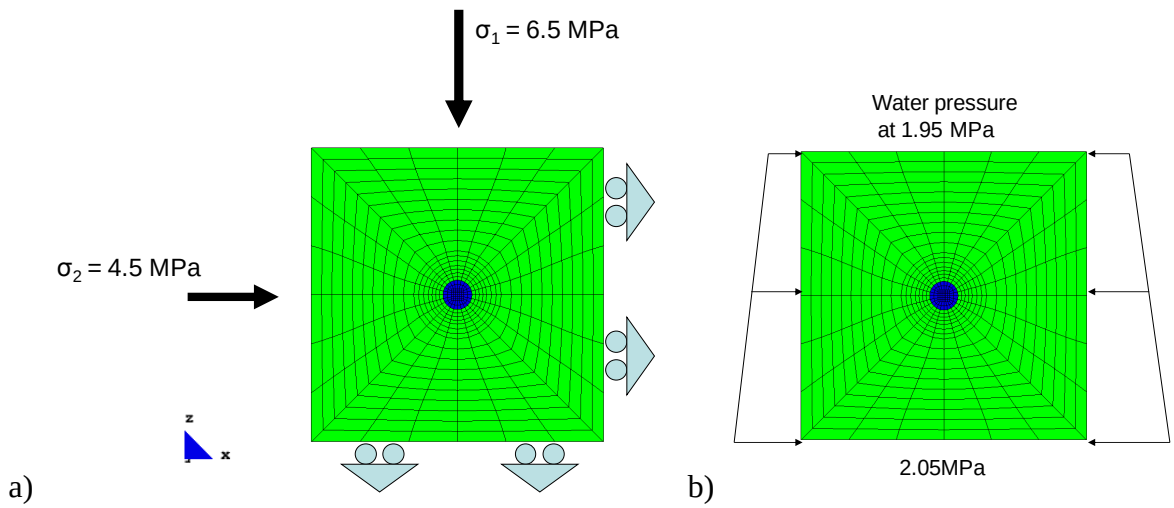

Figure 3-3. Boundary conditions: a) mechanical (principal stresses $\sigma_1 = 6.5\,\text{MPa}$, $\sigma_2 = 4.5\,\text{MPa}$, $\sigma_3 = 2.5\,\text{MPa}$); b) hydraulic (upper face $p_l = 1.95\,\text{MPa}$, lower face $p_l = 2.05\,\text{MPa}$).

Finally, it is recalled that in this model the gas phase pressure p_g was not computed and a constant value of 0.1 MPa was imposed.

3.2.3 Material models

The Opalinus clay was assumed to be a cross-anisotropic linear poroelastic material with constant (matrix) cross-anisotropic intrinsic permeability (no isotropic contribution from the cracks). The isotropy planes were assumed to coincide with the bedding planes, with strike line parallel to the tunnel axis and dip angle of 45°, as shown in the following figure.

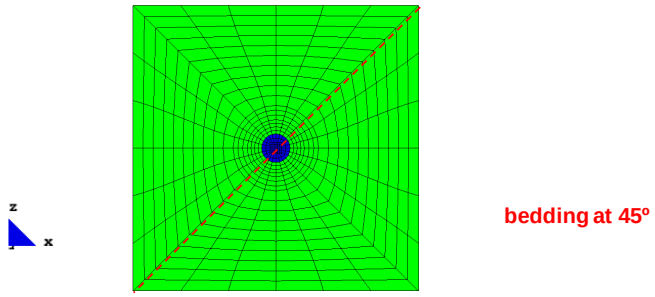

Figure 3-4. Orientation of the bedding planes (isotropy planes).

The effective moduli of the cross-anisotropic linear poroelastic model and the eigenvalues of the cross-anisotropic intrinsic permeability are shown in the following table, where the subscript $\|$ refers to the isotropy plane and the subscript $\perp$ refers to the direction orthogonal to the isotropy plane. Recall that temperature is the only parameter of the considered constitutive relations for the liquid phase (density and viscosity).

Table 3-1. Values used for the parameters of the constitutive relations.

Porous medium					
$k_{\|}$	5.0×10^{-20}	m^2	$k_{\perp}$	5.0×10^{-21}	m^2
Solid and liquid phases					
ρ_s	2700	kg/m^3	T	20	$°C$
Solid skeleton					
$E'_{\|}$	10000	MPa	$\nu'_{\|}$	0.27	–
$E'_{\perp}$	4000	MPa	$\nu'_{\|\perp}$	0.27	–
$G_{\|\perp}$	1575	MPa			

3.2.4 Calculation phases

Three modeling phases were considered in the simulation of the tunnel excavation, as shown in the table below.

Table 3-2. Modelling phases.

days	description
0-100	Stress equilibrium and pore water pressure equalisation
100-107	Microtunnel excavation
107-217	Tunnel drainage ($p_l = 0.10\ MPa$ on microtunnel wall)

The first phase of 100 days was used to generate the initial stress field and the initial liquid phase pressure field. The second phase of 7 days was used to excavate the HG-A tunnel, whereby, as shown in Figure 3-5, the considered evolution of the excavation followed quite close the real one. The tunnel excavation was simulated by removing elements from the finite element mesh and, on the newly created surfaces, applying a total pressure of 0.1 MPa and a liquid phase pressure p_l of 0.1 MPa (atmospheric pressure). Finally, the third phase of 110 days was used to determine the evolution of the state of the Opalinus clay near the HG-A tunnel.

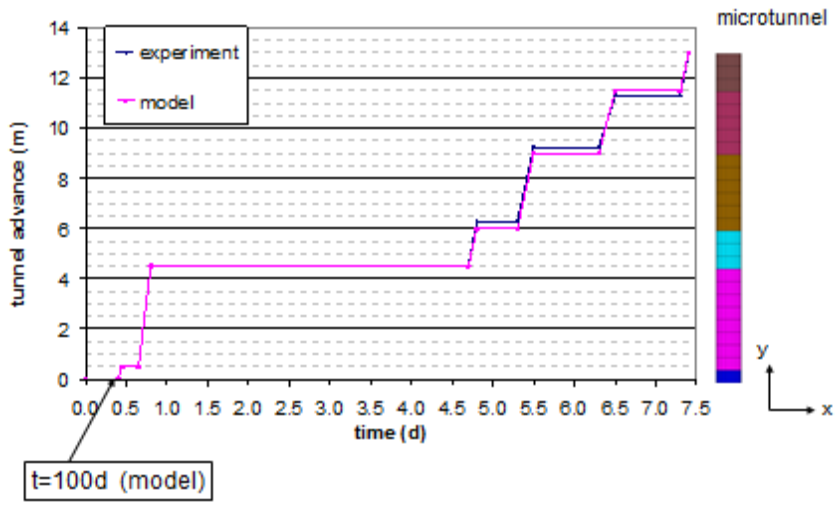

Figure 3-5. Real and modeled evolution of the excavation of the HG-A tunnel.

3.2.5 Results

In this section, a selection of the results obtained is presented, including evolutions and distributions of the following variables

- liquid phase pressure
- solid skeleton displacements
- porosity
- stresses

In some cases, the computed results have been compared with measurements recorded by installed sensors.

The evolution of the liquid phase pressure at the various isolated intervals in boreholes BHG-A2 and BHG-A3 drilled before the excavation of the tunnel has been recorded, and it is interesting to compare them with the modelling results. Figure 3-6 shows the location of the boreholes with respect to the tunnel and the measured evolutions at borehole BGH-A2, located 1.50 m above the tunnel, (sensor B-A02PE1 for interval 1, sensor B-A02PE2 for interval 2 and sensor B-A02PE3 for interval 3) and at borehole BGH-A3, located at 0.50 m to the left of the tunnel (sensor B-A03PE1 for interval 1, sensor B-A03PE2 for interval 2 and sensor B-A03PE3 for interval 3).

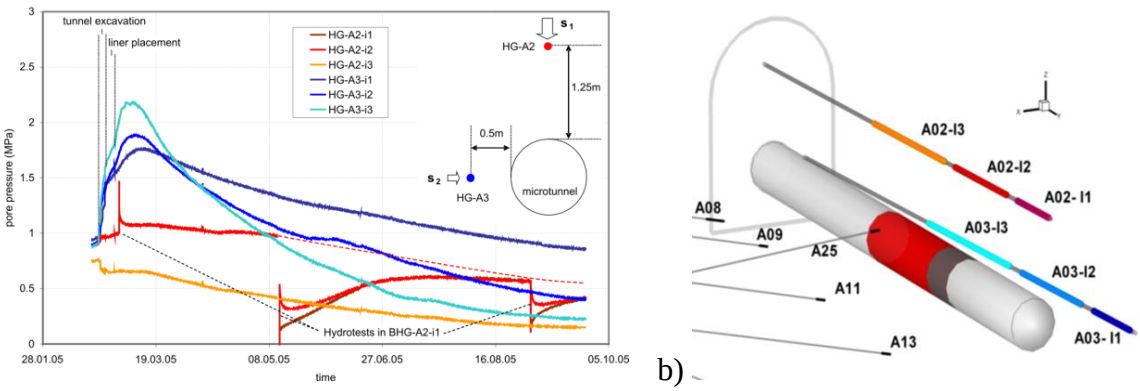

Figure 3-6. Measured evolution of the liquid pressure at the isolated intervals in boreholes BHG-A2 and BHG-A3, Marschall et al. (2006).

The corresponding evolutions of liquid pressure at those 6 points located in the isolated intervals of boreholes BHG-A2 and BHG-A3 computed using the described model are shown in Figure 3-7. These evolutions exhibit the fast generation of excess liquid phase pressures due to the tunnel excavation and their slow dissipation.

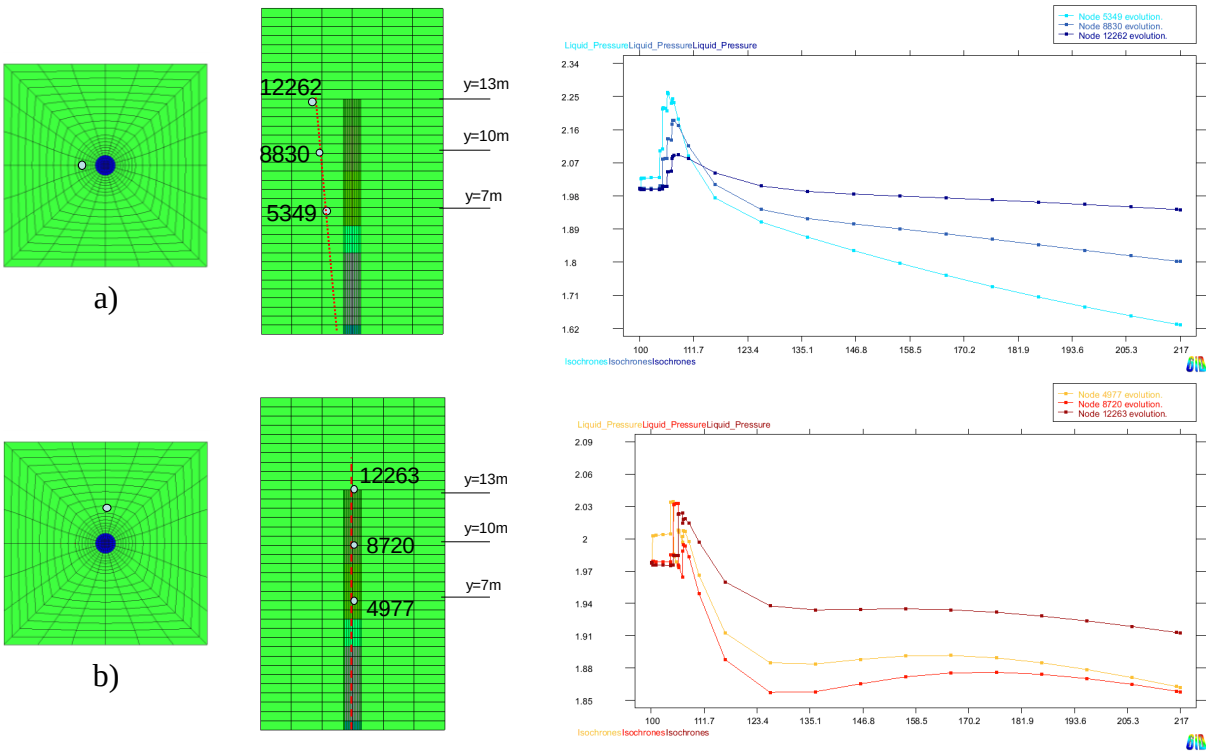

Figure 3-7. Evolutions of liquid phase pressures: a) nodes within intervals i1, i2 and i3 of BHG-A3; b) nodes within intervals i1, i2 and i3 of BHG-A2.

In Figure 3-8, measured and computed evolutions are compared, using similar colors for corresponding evolutions. It may be seen that calculated and measured evolutions are qualitatively similar, but their values are quite different.

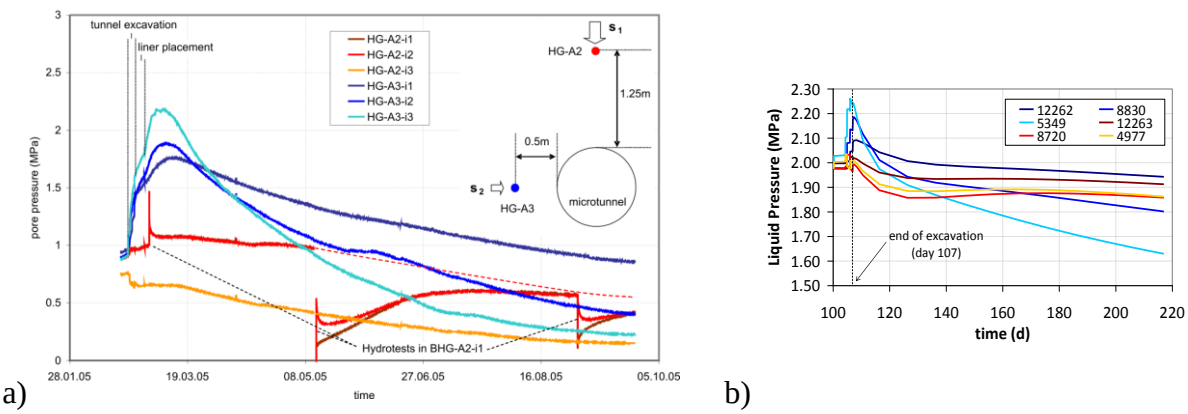

Figure 3-8. Evolutions of liquid pressure at the isolated intervals in boreholes HG-A2 (above the tunnel) and HG-A3 (at the left of the tunnel), that are subparallel to the tunnel; a) measured by the installed sensors, Marschall et al. (2006); b) computed using the model. Note that the same colours are used for corresponding evolutions in a) and b), but time and pressure scales used on b) double those used on a).

Figure 3-9 shows the distributions of liquid phase pressures on a vertical plane at 7 m, whereby the effect of the anisotropy of the Opalinus clay due to the bedding planes is evident.

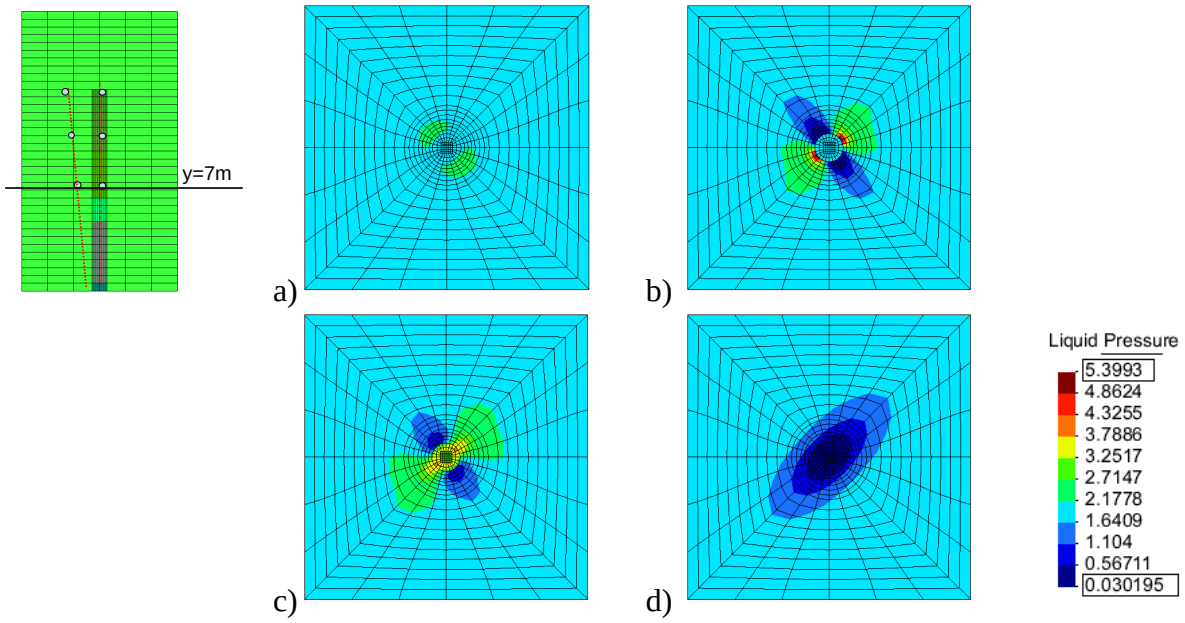

Figure 3-9. Distributions of liquid pressures on a vertical plane at 7 m at: a) 104.9 days, just before passage of tunnel; b) 104.928 days, passage of tunnel; c) 107 days; and d) 217 days.

In order to better understand the liquid pressure field arising from the tunnel excavation, Figure 3-10 shows the evolution of the liquid phase pressure at 8 points located on a vertical plane at 7 m and at 0.5 m from the tunnel wall. These evolutions, which are symmetric with respect to the bedding planes, exhibit large variations at points 2, 6 (decrements), 4 and 8 (increments), but small variations at points 1, 5 (increments), 3 and 7 (decrements). Therefore, a change in the considered dip angle of the bedding planes would improve the predictions at the isolated intervals of boreholes HG-A2 and HG-A3.

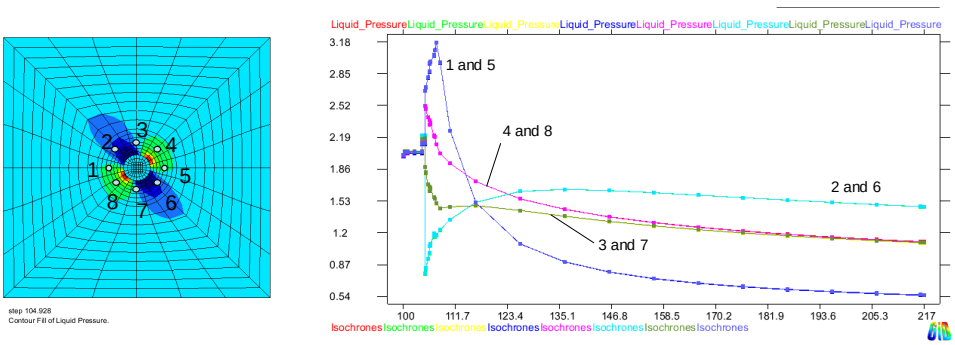

Figure 3-10. Evolutions of liquid phase pressures at 8 points distant 0.50 m from the tunnel wall on a vertical plane at 7 m.

Figure 3-11 shows the distributions of liquid pressures on a plane perpendicular to the bedding plane and passing through the tunnel axis and corresponding to several time instants. Figures a) to g) correspond to tunnel excavation, when excess liquid phase pressures originate. Figures h) and i) correspond to excess liquid phase pressures dissipation.

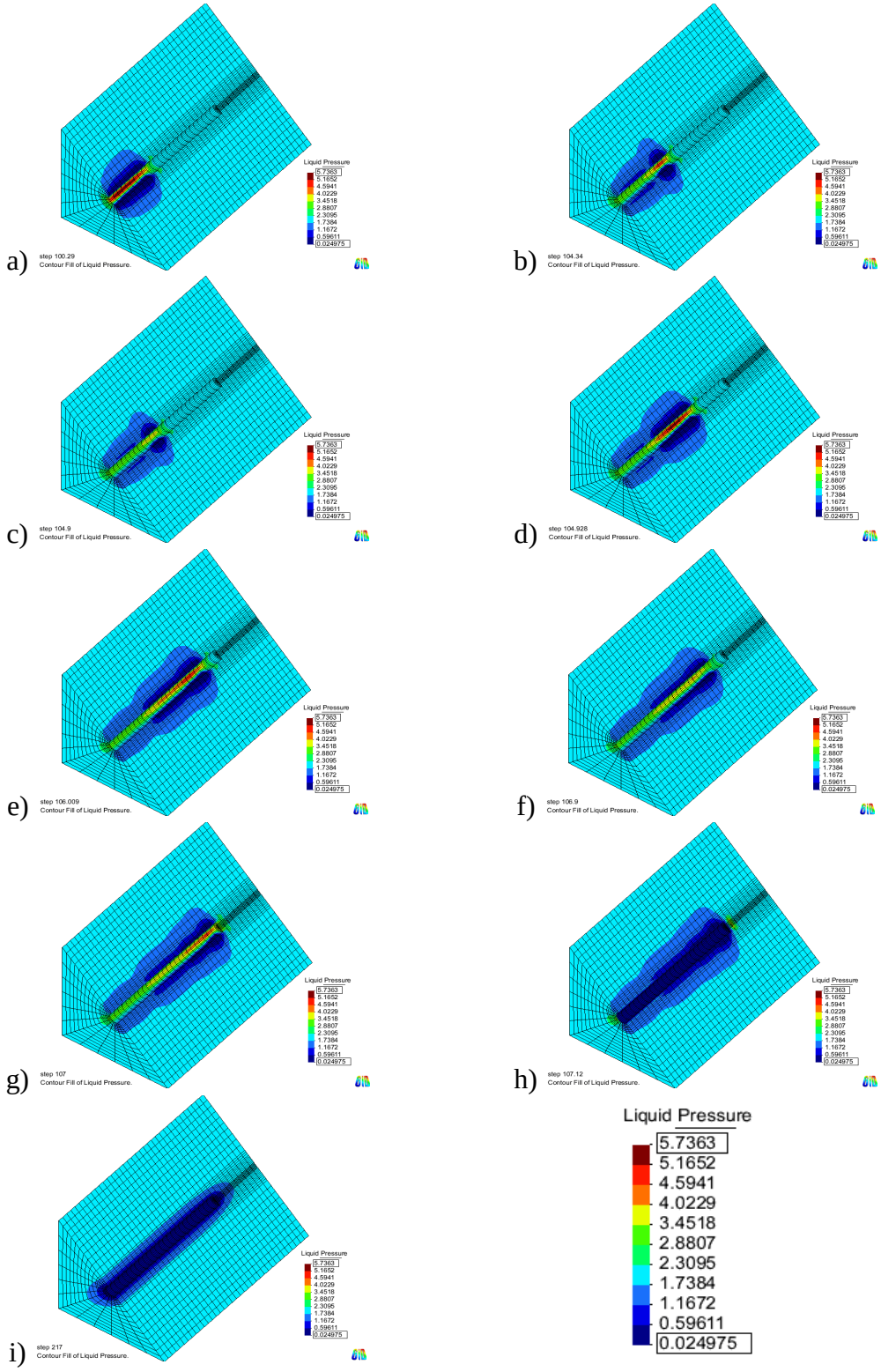

Figure 3-11. Distributions of liquid pressures on a plane perpendicular to the bedding plane and passing through the tunnel axis at time instants: a) 100.29 days, 0.29 days after the start of tunnel excavation; b) 104.34 days; c) 104.9 days; d) 104.928 days; e) 106.009 days; f) 106.9 days; g) 107 days, end of tunnel excavation; h) 107.12 days; and i) 217 days.

Figure 3-12 shows the distribution of the displacement modulus on a vertical plane at y = 7 m just after the tunnel excavation and 110 days later, and Figure 3-13 shows the evolutions of the vertical and horizontal components of the displacements at two points located on a vertical plane at y = 7 m, close to the tunnel. The effects of excess liquid phase pressure dissipation and of the anisotropy are evident. Figure 3-14 shows the measured evolutions of the vertical and horizontal components of the displacements at boreholes BHG-A4 and BHG-A6.

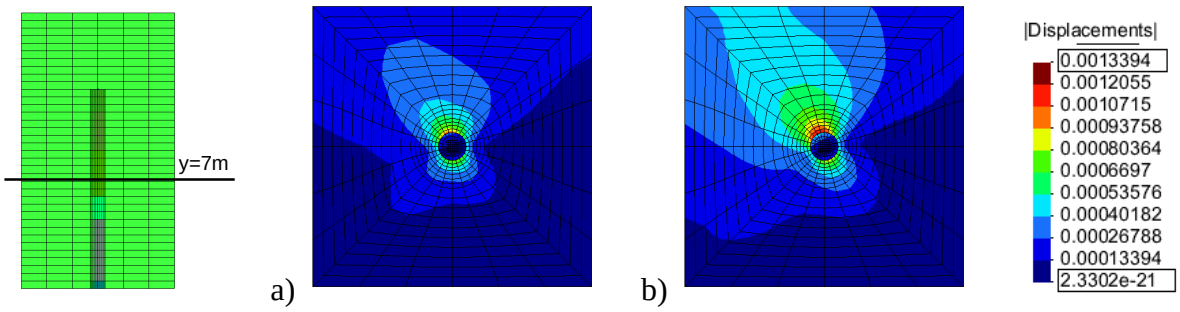

Figure 3-12. Computed distributions of displacement modulus (in m) on a vertical plane at y = 7 m at: a) 107 days (end of tunnel excavation); and b) 217 days.

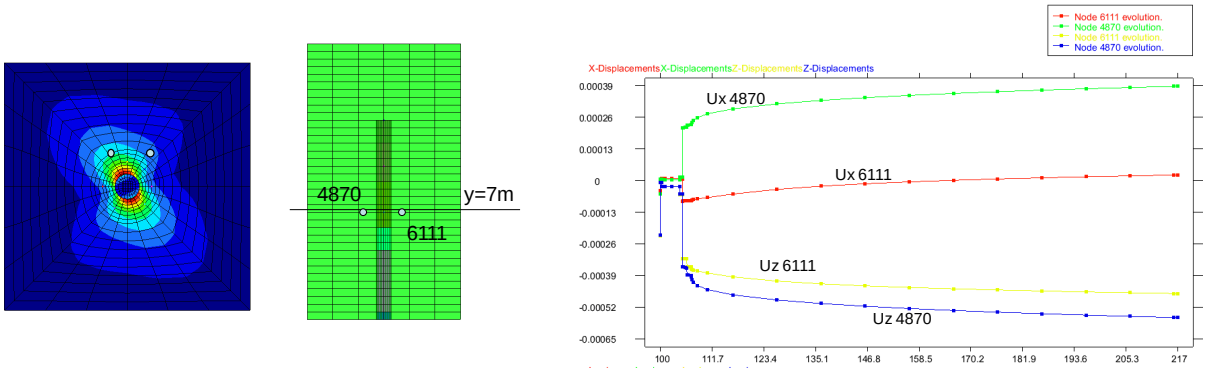

Figure 3-13. Computed evolution of horizontal (Ux) and vertical (Uz) displacements (in m) of two points on a vertical plane at y = 7 m.

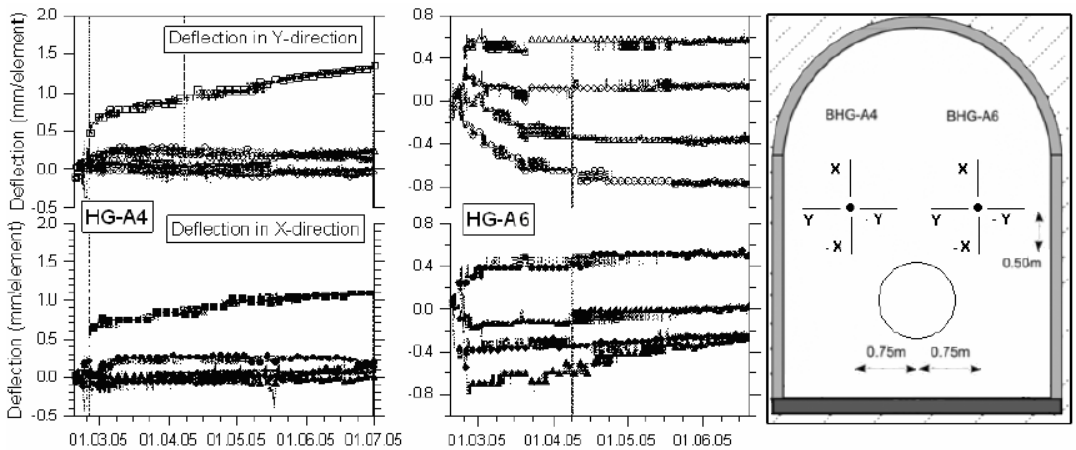

Figure 3-14. Deflections measured in boreholes BHG-A4 (left), BHG-A6 (center) and their position relative to the microtunnel (right), Trick et al. (2007).

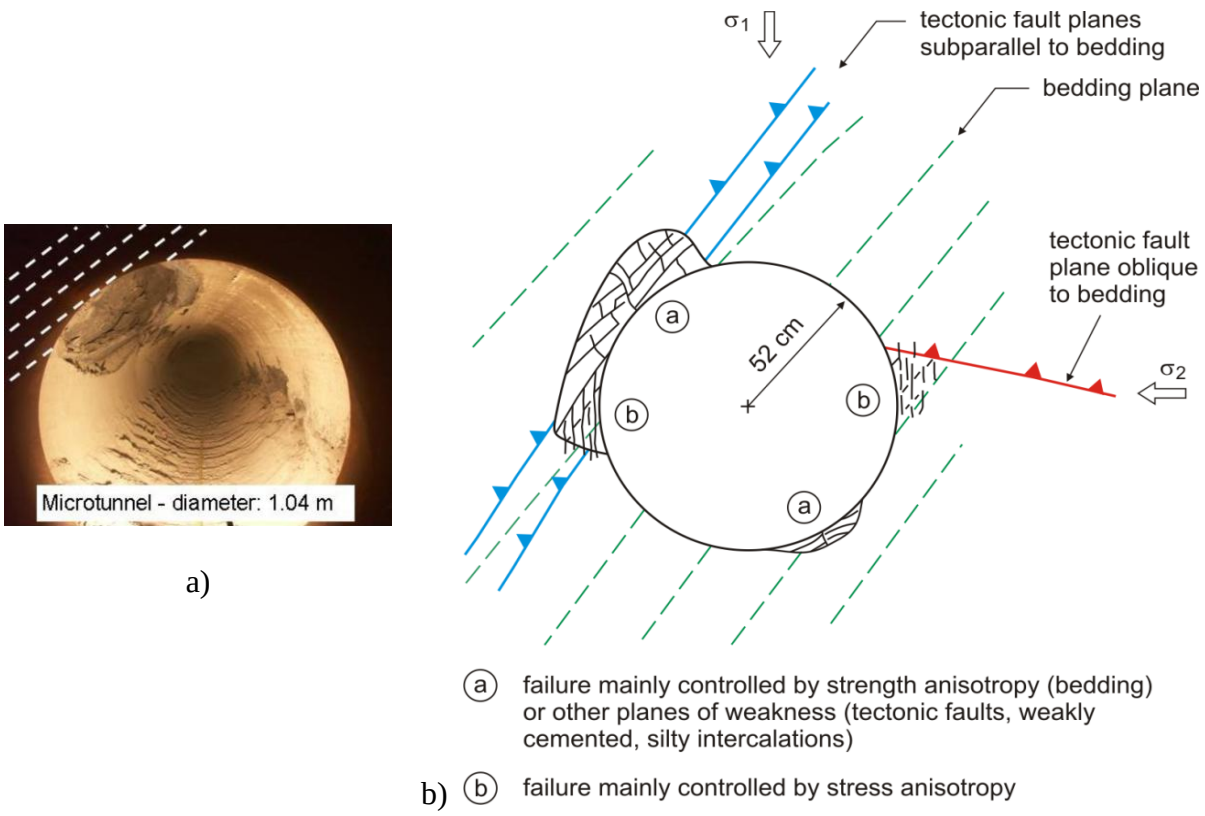

Figure 3-15. Damage zones around de HG-A tunnel: a) observed, after Marschall et al. (2008): (dashed lines indicate bedding direction) the upper left breakout is about 1.5 m long (about y = 6.0 m – 7.5 m, after the steel liner); and b) interpretation, after Marschall et al. (2006): slablike breakouts on the upper left side are due to extensile failure along tectonic fractures; wedge-like breakouts on the right side.

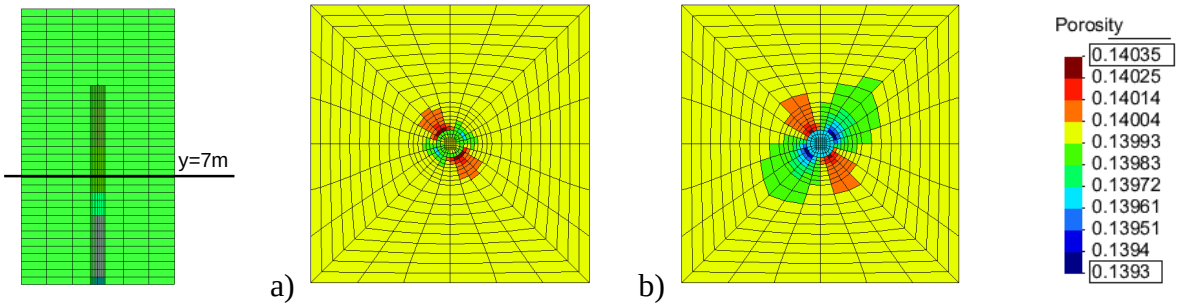

Figure 3-16. Computed distributions of porosity on a vertical plane at y = 7 m at: a) 107 days (end of tunnel excavation); and b) 217 days.

Figure 3-15 shows the damaged zones observed around the HG-A tunnel, and an interpretation of the involved mechanisms. Figure 3-16 shows the distribution of porosity on a vertical plane at y = 7 m just after the tunnel excavation and 110 days later. Although a cross-anisotropic linear poroelastic model has been used, the zones with higher porosity are located where the larger damaged zones have been observed. The effect of excess liquid phase pressure dissipation is also clear in Figure 3-17, which shows the corresponding distributions of porosity on a plane orthogonal to the bedding planes and passing through the tunnel axis.

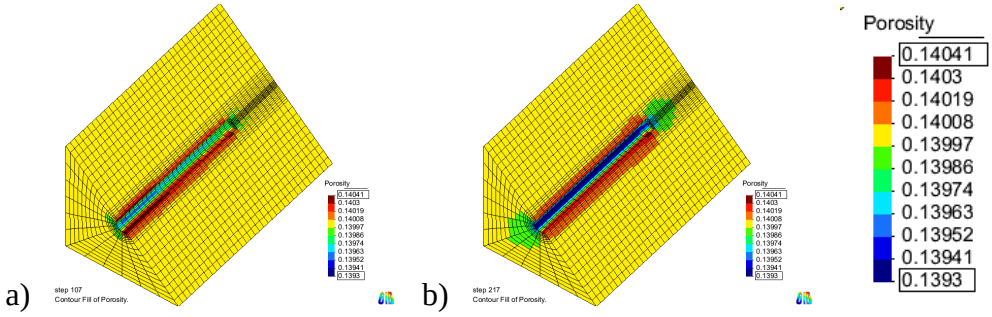

Figure 3-17. Computed distributions of porosity on a plane orthogonal to the bedding planes and passing through the tunnel axis at: a) 107 days (end of tunnel excavation); and b) 217 days.

The computed distributions of σ_1 just after the tunnel excavation and 110 days later on a vertical plane at y = 7 m and on a plane orthogonal to the bedding planes and passing through the tunnel axis are shown in Figure 3-17 and in Figure 3-18, respectively.

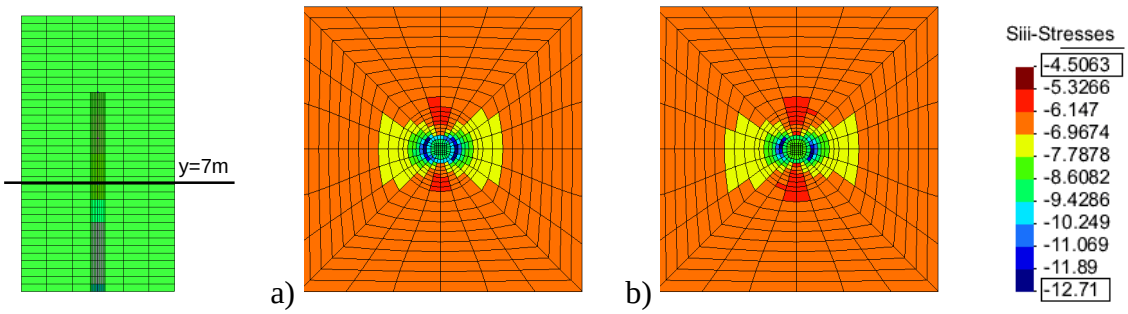

Figure 3-18. Computed distributions of σ_1 (in MPa) on a vertical plane at y = 7 m at: a) 107 days (end of tunnel excavation); and b) 217 days.

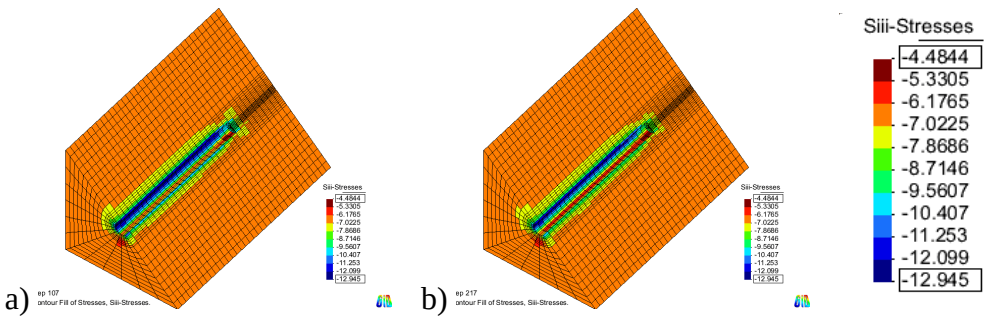

Figure 3-19. Computed distributions of σ_1 (in MPa) on a plane orthogonal to the bedding planes and passing through the tunnel axis at: a) 107 days (end of tunnel excavation); and b) 217 days.

Finally, the computed distributions of σ_3 just after the tunnel excavation and 110 days later on a vertical plane at y = 7 m and on a plane orthogonal to the bedding planes and passing through the tunnel axis are shown in Figure 3-20 and in Figure 3-21, respectively. Note the changes due to excess liquid phase pressure dissipation.

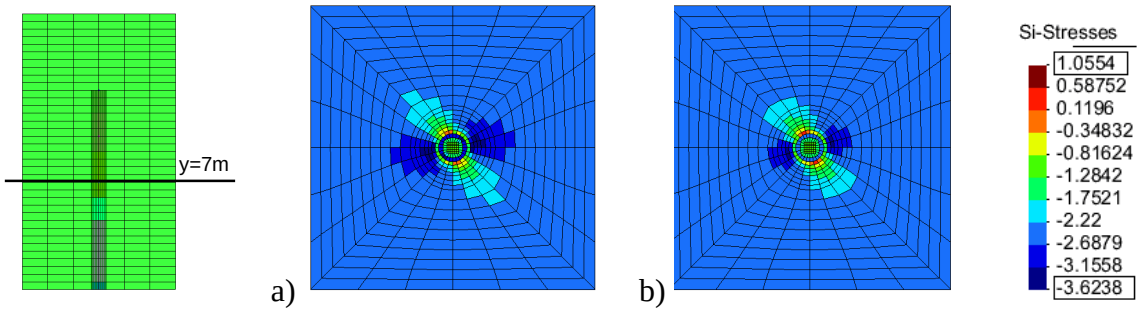

Figure 3-20. Computed distributions of σ_3 (in MPa) on a vertical plane at y = 7 m at: a) 107 days (end of tunnel excavation); and b) 217 days.

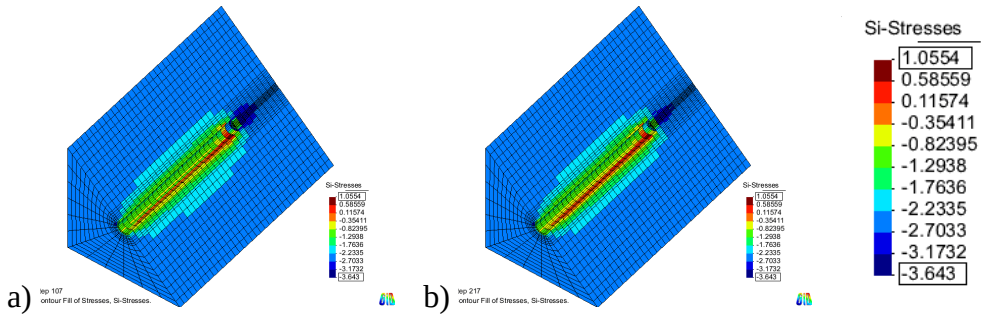

Figure 3-21. Computed distributions of σ_3 (in MPa) on a plane orthogonal to the bedding planes and passing through the tunnel axis at: a) 107 days (end of tunnel excavation); and b) 217 days.

4 Modelling of the liquid and gas injection tests

The modelling strategy has been to generate a model as simple as possible, as we believe that this will lead to an understanding of the HG-A test, and to a reduction of the computational effort. In this regard, based on the available information, we select a priori the physical processes that we expect that are more relevant to the HG-A test. If, after parameter calibration, the model reproduces the main trends of the observed behaviour, then we may claim that the selected physical processes explain the observed behaviour. If this is not the case, then the model misses some physical process, which is relevant to the HG-A test. Therefore, we view modelling as an iterative process that helps us in understanding the physical processes that take place in the HG-A test.

As a result of the tunnel excavation, an EDZ was created around the tunnel. Because of the low permeability of the (undamaged) Opalinus clay, the liquid and gas injected into the test section during the liquid and gas injection tests were forced to flow back along the EDZ. As shown in the previous section, there is evidence that the EDZ is anisotropic and inhomogeneous, whereby some zones were detached (and subsequently repaired) and localized zones of relatively high conductivity were observed, as explained in Lanyon et al. (2008) and in Marschall et al. (2008). Additional documentation for the HG-A test includes Marschall et al. (2005), Marschall et al. (2006) and Trick et al. (2007).

Based on the available documentation, we can deduce some features of the HG-A test.

- **Liquid and gas flows.** The intrinsic permeability of the (undamaged) Opalinus clay is about $k^{OPA} = 10^{-19} m^2$, whereas the intrinsic permeability of the EDZ is about $k^{EDZ} = 1.1 \times 10^{-15} m^2$. Therefore, there is a contrast of about 4 orders of magnitude, and we expect that flows of the liquid and gas phases, will essentially take place in the EDZ.

- **Deformation**. The stiffness of the (undamaged) Opalinus clay is at least about $K'^{OPA} = 2900\ MPa$ ($K'^{OPA} = E'^{OPA} / (3(1-2\nu'^{OPA}))$, $E'^{OPA} = 4000\ MPa$, $\nu'^{OPA} = 0.27$) and the stiffness of the EDZ is about $K'^{EDZ} = 400\ MPa$ ($K'^{EDZ} = (S^{EDZ} / \rho_w g - \beta_w \phi^{EDZ})^{-1}$, $S^{EDZ} = 3 \times 10^{-5} m^{-1}$, $\phi^{EDZ} = 0.11$, $g = 9.81\, m/s^2$, $\rho_w = 10^3\ kg/m^3$, $\beta_w = 4.5 \times 10^{-4}\ MPa^{-1}$). Thus, there is a contrast of about 1 order of magnitude, and we expect that the deformation of the (undamaged) Opalinus clay surrounding the HG-A should have a non-negligible mechanical influence on the EDZ.

Concerning the material behaviour, we have made the following preliminary considerations

- **EDZ**. As shown by the detailed inspection of the tunnel surface, the extent of the EDZ is not uniform, and the mechanical and hydraulic responses of the EDZ are heterogeneous and anisotropic. However, in view of the uncertainties in the material behaviour of the EDZ and in its initial state, we have decided to assume the EDZ to be a homogeneous and isotropic material, with a uniform thickness (0.20 m was considered to be appropriate).

- **(undamaged) Opalinus clay**. As the mechanical properties of the EDZ will tend to mask the mechanical properties of the surrounding (undamaged) Opalinus clay, we have assumed that the surrounding Opalinus clay is a homogeneous and isotropic material, thereby neglecting the anisotropy due to the bedding planes.

Further modelling assumptions allow reducing the number of geometric dimensions of the model for the HG-A test. In this regard, two models were prepared (both using the same constitutive laws).

- **2D axisymmetric model**. We note that: (1) the geometry of the HG-A test is essentially axisymmetric about the tunnel axis; (2) the inputs to the HG-A tests (injection of liquid and gas into the test section and the megapacker pressure applied to the tunnel wall) are roughly axisymmetric about the tunnel axis; and (3) gravity is expected to have a small influence (particularly on liquid and gas flows). These considerations lead to the 2D axisymmetric model (2 geometric dimensions), for which CODE_BRIGHT was used.

- **1D simplified model**. Besides the assumptions leading to the 2D axisymmetric model, it is possible to make additional simplifying assumptions, which are found to be appropriate for the HG-A test. These considerations lead to the 1D simplified model, (1 geometric dimension), which was implemented on a Excel spreadsheet..

4.1 Test protocols

The considered test input protocol consists of polygonal approximations to the records (measured by the appropriate test sensors) of (1) megapacker pressure (sensor M-PAMegapacker); (2) liquid phase volume injection rate (sensor M-Flow); and (3) gas phase volume injection rate (sensor M-GasFlow), as shown in Figure 4-1. For representation purposes, the 15th of April 2006 was taken as day 0.

The test input protocol applied to the test section is stated as evolutions with time of the liquid phase volume injection rate $Q_l(t)$ (in ml/min) and gas phase volume injection rate $Q_g(t)$ (in mln/min). However, in the followed approach the boundary conditions considered are stated as water mass injection rate $M_w(t)$ (in kg/s) and air mass injection rate $M_a(t)$ (in kg/s), since they are naturally associated to the balance of mass of species water equation and to the balance of mass of species air equation, respectively. As explained in Alcoverro et al. (2012), the following transformation expressions were used

$$M_w(t)\frac{kg}{s} = Q_l(t)\frac{ml}{min}\times\frac{1min}{60s}\times\rho_l(T)\frac{kg}{m^3}\times\frac{1m^3}{1000l}\times\frac{1l}{1000ml}\times(1-\omega_{l\ ext}^{a}) + Q_g(t)\frac{mln}{min}\times\frac{1min}{60s}\times\frac{M_a\frac{kg}{mol}\times 0{,}1MPa}{R\frac{MPa\cdot m^3}{°K\cdot mol}\times(273.15+T)°K}\times\frac{1m^3n}{1000ln}\times\frac{1ln}{1000mln}\times\omega_{g\ ext}^{w} \tag{4.1}$$

$$M_a(t)\frac{kg}{s} = Q_l(t)\frac{ml}{min}\times\frac{1min}{60s}\times\rho_l(T)\frac{kg}{m^3}\times\frac{1m^3}{1000l}\times\frac{1l}{1000ml}\times\omega_{l\ ext}^{a} + Q_g(t)\frac{mln}{min}\times\frac{1min}{60s}\times\frac{M_a\frac{kg}{mol}\times 0{,}1MPa}{R\frac{MPa\cdot m^3}{°K\cdot mol}\times(273.15+T)°K}\times\frac{1m^3n}{1000ln}\times\frac{1ln}{1000mln}\times(1-\omega_{g\ ext}^{w}) \tag{4.2}$$

where $\omega_{l\ ext}^{a}$ is the air mass fraction in the liquid phase at the injection point and $\omega_{g\ ext}^{w}$ is the water mass fraction in the gas phase at the injection point, M_w and M_a are the molar mass of water and air and R is the constant of gases.

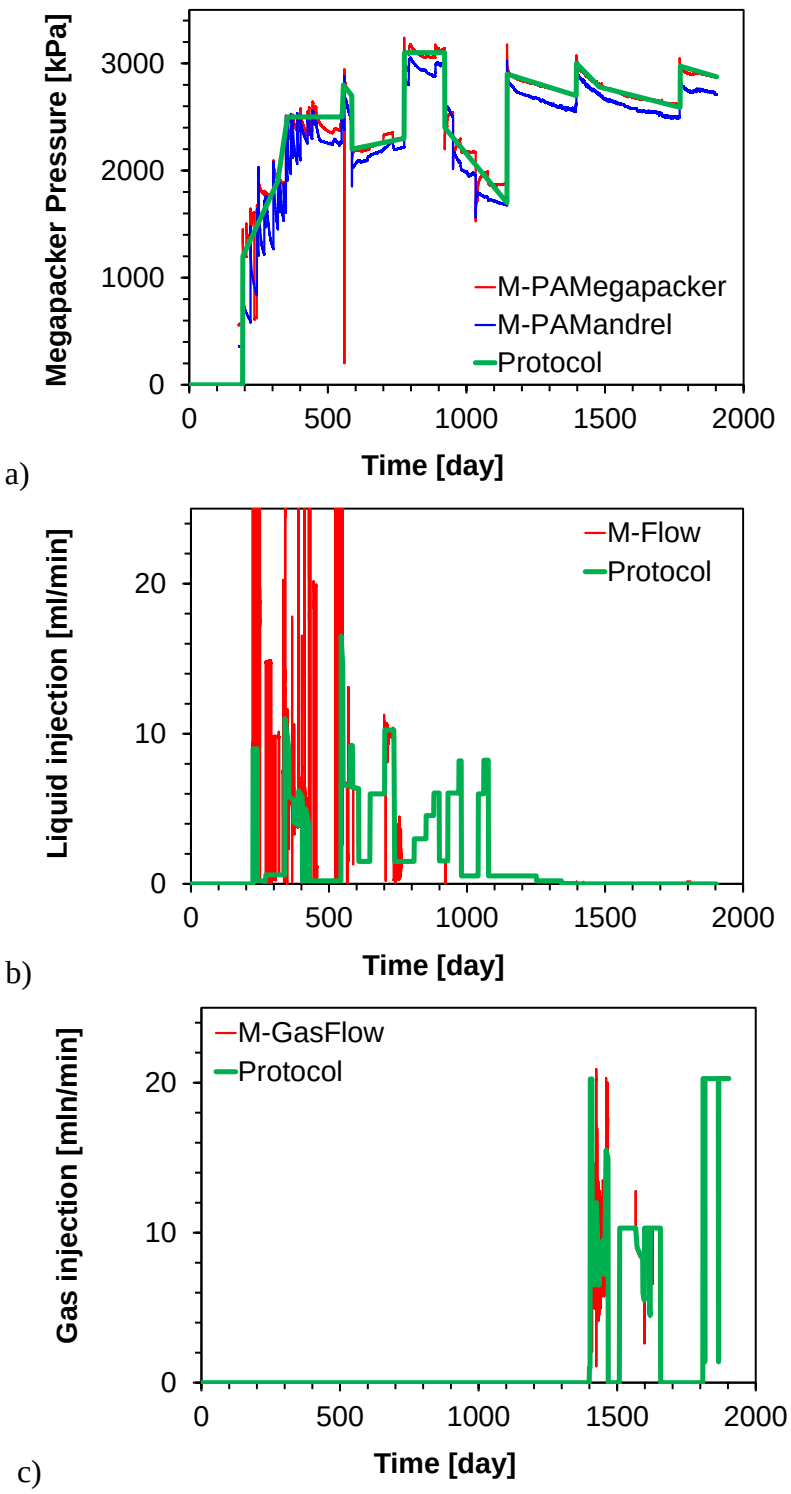

Figure 4-1. Measured input evolutions and model polygonal approximations: a) megapacker pressure; b) liquid volume injection rate; and c) gas volume injection rate.

4.2 2D axisymmetric model

As already mentioned, in an effort to keep the modeling as simple as possible, the anisotropy induced by the bedding planes of the Opalinus clay was not taken into account, and the effect of gravity was neglected. In view of the HG-A test geometry, this approach leads to a 2D axisymmetric model, which corresponds to an average behavior of the EDZ. Indeed, there is evidence that the EDZ is anisotropic and inhomogeneous, whereby some zones were detached (and subsequently repaired) and localized zones of relatively high conductivity have been observed. In this section, a summary of the main features of the 2D axisymmetric model, which was implemented using CODE_BRIGHT, and the obtained results, including the calibration, is presented.

4.2.1 Geometry and coordinate system

Figure 4-2 a) shows a detail of the geometry around the megapacker section. Because of the assumed axisymmetry, the problem is 2D and its generating surface is shown in Figure 4-2 b). It is a rectangle measuring 18.0 m in the tunnel axis direction (y-axis) and 5.0 m in the radial direction (x-axis), from which a rectangle measuring 9.0 m in the tunnel axis direction and 0.5 m in the radial direction (corresponding to the megapacker and liner sections) was removed. The y-axis coincides with the axis of the tunnel, which is also the axisymmetry axis. The EDZ (in blue) is 0.20 m thick and the test section (in pink) is 4.0 m long and 0.5 m thick.

The finite element mesh is shown in Figure 4-2 c). It is made of 4-noded linear quadrilateral elements with selective integration. In total, there were 1330 elements and 1428 nodes. Note the smaller size of the elements around the EDZ, including the test section.

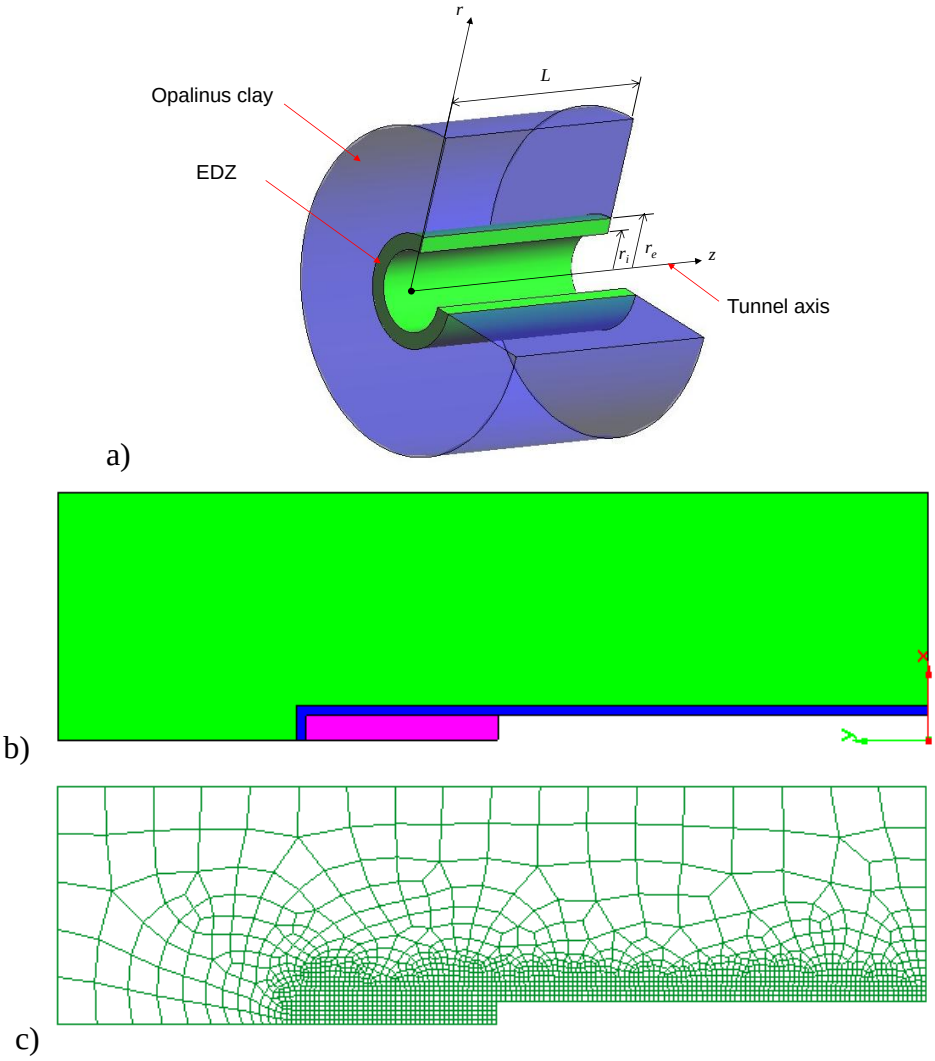

Figure 4-2. a) Geometry around the megapacker section and system of coordinates; b) modelled region and materials: (undamaged) Opalinus clay (green), EDZ (blue) and gravel (pink); the tunnel axis is the axisymmetry axis; and c) finite element mesh.

4.2.2 Initial and boundary conditions

The following values have been assumed for the initial conditions.

- **(undamaged) Opalinus clay**

  Solid skeleton displacements $u_r^0 = 0.0\,m$, $u_y^0 = 0.0\,m$, $u_\theta^0 = 0.0\,m$.
  Liquid phase pressure $p_l^0 = 0.1\,MPa$
  Gas phase pressure $p_g^0 = 0.1\,MPa$ (atmospheric)
  Porosity $\phi^0 = 0.12$
  Principal stresses $\sigma_r^0 = -5.5\,MPa$, $\sigma_y^0 = -2.5\,MPa$, $\sigma_\theta^0 = -5.5\,MPa$.

- **EDZ**

  Solid skeleton displacements $u_r^0 = 0.0\,m$, $u_y^0 = 0.0\,m$, $u_\theta^0 = 0.0\,m$.
  Liquid phase pressure $p_l^0 = 0.1\,MPa$
  Gas phase pressure $p_g^0 = 0.1\,MPa$ (atmospheric)
  Porosity $\phi^0 = 0.12$
  Principal stresses $\sigma_r^0 = -5.5\,MPa$, $\sigma_y^0 = -2.5\,MPa$, $\sigma_\theta^0 = -5.5\,MPa$.

- **Gravel (after being backfilled in the test section)**

  Solid skeleton displacements $u_r^0 = 0.0\,m$, $u_y^0 = 0.0\,m$, $u_\theta^0 = 0.0\,m$.
  Liquid phase pressure $p_l^0 = 1.0\,MPa$
  Gas phase pressure $p_g^0 = 0.1\,MPa$ (atmospheric)
  Porosity $\phi^0 = 0.30$
  Principal stresses $\sigma_r^0 = -0.1\,MPa$, $\sigma_y^0 = -0.1\,MPa$, $\sigma_\theta^0 = -0.1\,MPa$.

Boundary conditions are of mechanical and hydraulic type, and are schematically shown in Figure 4-3. The megapacker pressure is taken into account as a (line) boundary condition (roller). The liquid or gas injection rates are converted into mass of species water and mass of species air rates, and are taken into account as (point) boundary conditions. The steel liner is replaced by a (line) boundary condition (roller, with liquid and gas pressures prescribed to the values at the Mont Terri URL).

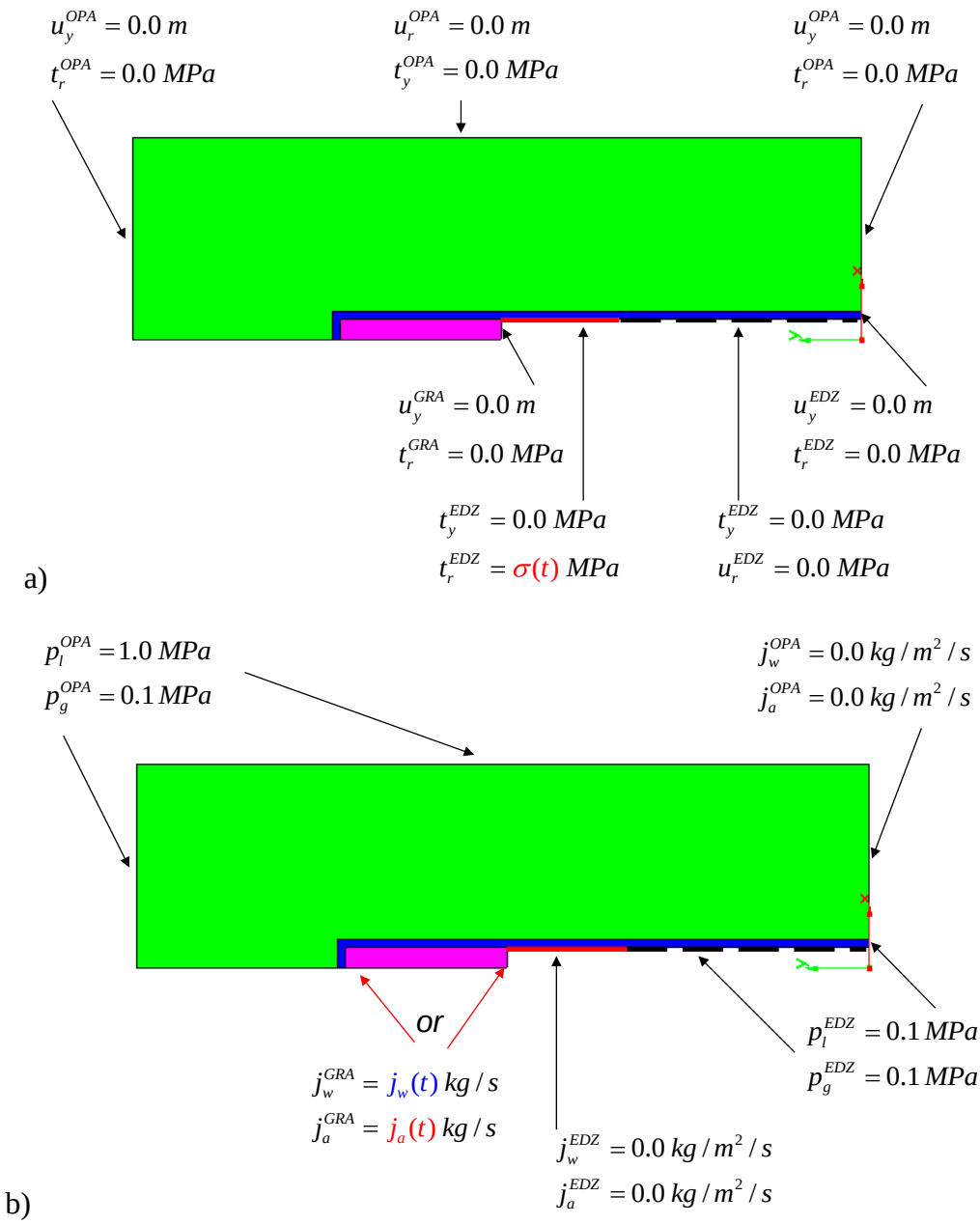

Figure 4-3. Boundary conditions: a) mechanical (u_y are and u_r are the components of the displacement; t_y are and t_r are the components of the (total) traction); b) hydraulic (j_w are and j_a are mass rates of species water and species air).

4.2.3 Material models

Three materials have been considered in the model: EDZ, (undamaged) Opalinus clay and gravel. Their positions and dimensions in the modelled zone are indicated in Figure 4-2 b) using different colours. The colour and constitutive laws used for each material are summarized below.

EDZ. (blue) Linear poroelastic, Van Genuchten retention curve, isotropic permeability depending on volumetric deformation, Van Genuchten liquid phase relative permeability and generalised power law gas phase relative permeability.

Opalinus clay. (green) Linear poroelastic, Van Genuchten retention curve, isotropic permeability, Van Genuchten liquid phase relative permeability and generalised power law gas phase relative permeability.

Gravel. (pink) Linear poroelastic, Van Genuchten retention curve, isotropic permeability, generalised power law liquid phase relative permeability and generalised power law gas phase relative permeability.

Table 4-1 shows the values used for the constitutive parameters corresponding to the best fit.

Table 4-1. Values used for the constitutive parameters. Parameters with values in boldface have been varied during the process of calibration, and the values indicated correspond to the best fit, denominated case 6 (unsat). (*) Q_l is measured in $MPa{\cdot}m^3/mol$; (**) D_g is measured in $m^2/s{\cdot}MPa{\cdot}°K^{-Q_g}$.

Elastic effective properties							
E'^{EDZ}	**0.8×10^3**	MPa	E'^{OPA}	4.0×10^3	MPa	E'^{GRA}	0.1×10^3 MPa
ν'^{EDZ}	0.30	–	ν'^{OPA}	0.30	–	ν'^{GRA}	0.30 –
Water retention curve							
λ^{EDZ}	0.33	–	λ^{OPA}	0.33	–	λ^{GRA}	0.60 –
P_0^{EDZ}	0.243	MPa	P_0^{OPA}	10	MPa	P_0^{GRA}	0.01 MPa
Intrinsic permeability							
k_{matrix}^{EDZ}	**1.0×10^{-17}**	m^2	k^{OPA}	1.0×10^{-20}	m^2	k^{GRA}	1.0×10^{-14} m^2
b_0^{EDZ}	1.0×10^{-7}	m					
b_{max}^{EDZ}	**1.0×10^{-5}**	m					
a^{EDZ}	1.0×10^{-3}	m					
ε_0^{EDZ}	**-2.5×10^{-3}**	–					
Relative permeabilities							
λ_l^{EDZ}	0.33	–	λ_l^{OPA}	0.33	–		
						A_l^{GRA}	1 –
						n_l^{GRA}	3 –
A_g^{EDZ}	**1**	–	A_g^{OPA}	100	–	A_g^{GRA}	1 –
n_g^{EDZ}	3	–	n_g^{OPA}	1	–	n_g^{GRA}	3 –
Diffusion coefficients							
D_l^{EDZ}	1.4×10^{-4}	m^2/s	D_l^{OPA}	1.4×10^{-4}	m^2/s	D_l^{GRA}	1.4×10^{-4} m^2/s
Q_l^{EDZ}	2.54×10^{-2}	(*)	Q_l^{OPA}	2.54×10^{-2}	(*)	Q_l^{GRA}	2.54×10^{-2} (*)
D_g^{EDZ}	5.9×10^{-12}	(**)	D_g^{OPA}	5.9×10^{-12}	(**)	D_g^{GRA}	5.9×10^{-12} (**)
Q_g^{EDZ}	2.3	–	Q_g^{OPA}	2.3	–	Q_g^{GRA}	2.3 –

4.2.4 Calculation phases

The initial state was considered to be just after the tunnel has been excavated. Three modeling phases were considered in the simulation of the liquid and gas injection tests, as shown in the table below. The first phase of 100 days was used to generate the initial stress field and the initial liquid phase pressure field. During the second phase of 100 days the backfilling with gravel of the test section and the installation of the liner were simulated. The third phase was used to simulate the test set up (megapacker inflated to 1.70 MPa and liquid phase in the test section pressurized at 0.20 MPa, in order to resaturate the tunnel surroundings) and the test input protocol (evolution of the megapacker pressure applied to the tunnel wall and of the liquid and gas injection rates into the test section).

Table 4-2. Modelling phases.

days	description
0-100	Stress and liquid phase pressure equilibrium
100-200	Backfilling with gravel and liner installation
200-end	Test set up and test input protocols

The pressurisation of the test section at 0.20 MPa was modelled by applying that liquid phase pressure at a point situated on the centre of the tunnel cross section in contact with the gravel. Since gravel is highly permeable, this pressure propagates everywhere in the test section.

4.2.5 Calibration results

It should be mentioned that, in order to calibrate the model parameters, the 1D simplified model (see below) proved to be convenient for carrying out the pertinent sensitivity analyses. On the other hand, since calibration was focused on the liquid injection tests, the polygonal approximations to the megapacker pressure protocol and to the liquid injection rate protocol were quite accurate (shown in Figure 4-1 a) and b), respectively), but the polygonal approximation to the gas injection rate protocol was simplified (in Figure 4-11 a) to g) the schemes of the considered polygonal approximations are included).

As shown in Table 4-3, a number of cases were run using the 2D axisymmetric model. At first, the gravel in the test section was considered to be saturated and the liquid injection tests were used to calibrate the parameters related to liquid phase flow and deformation (i.e. k_{matrix}^{EDZ}, ε_0^{EDZ}, E'^{EDZ}, …). Afterwards, the gravel was changed from initially saturated to unsaturated to better capture the early liquid phase pressure variations induced by liquid injection.

Table 4-3. Cases considered for the 2D axisymmetric model. In parentheses it is indicated whether the test section was initially assumed to be saturated (sat) or unsaturated (unsat).

Case	k_{matrix}^{EDZ}	ε_0^{EDZ}	b_{max}^{EDZ}	E'^{EDZ}	A_g^{EDZ}	**Graphs**
	m^2	–	m	MPa	–	
1 (sat)	1.0×10^{-18}	-1.0×10^{-3}	1.0×10^{-4}	400	100	Figure 4-4
2 (sat)	1.0×10^{-18}	-2.0×10^{-3}	1.0×10^{-5}	400	100	Figure 4-5
3 (sat)	1.0×10^{-17}	-2.5×10^{-3}	1.0×10^{-5}	400	100	Figure 4-6
4 (sat)	1.0×10^{-16}	-2.5×10^{-3}	1.0×10^{-5}	400	100	Figure 4-7
4 (unsat)	1.0×10^{-16}	-2.5×10^{-3}	1.0×10^{-5}	400	100	Figure 4-8
5 (unsat)	1.0×10^{-17}	-2.5×10^{-3}	1.0×10^{-5}	800	100	Figure 4-9
6 (unsat)	1.0×10^{-17}	-2.5×10^{-3}	1.0×10^{-5}	800	1	Figure 4-10

The evolution of the liquid and gas pressures was compared with the evolution of the readings of sensor M-PEFloor, situated at the bottom of the test section, near the megapacker end. The following figures present such a comparison for each of the considered cases, and the evolution of the intrinsic permeability at a point located in the middle of the EDZ, close to the megapacker end.

Case 6 (unsat) corresponds to the best fit model and distributions of some relevant fields at several times are presented in the next section. As explained in a later section, this model was improved by taking into account a quite accurate polygonal approximation to the gas injection rate protocol (shown in Figure 4-1 c)) and the venting before gas injection tests (before starting a gas injection test, liquid was circulated through the test section in order to eliminate entrapped gas).

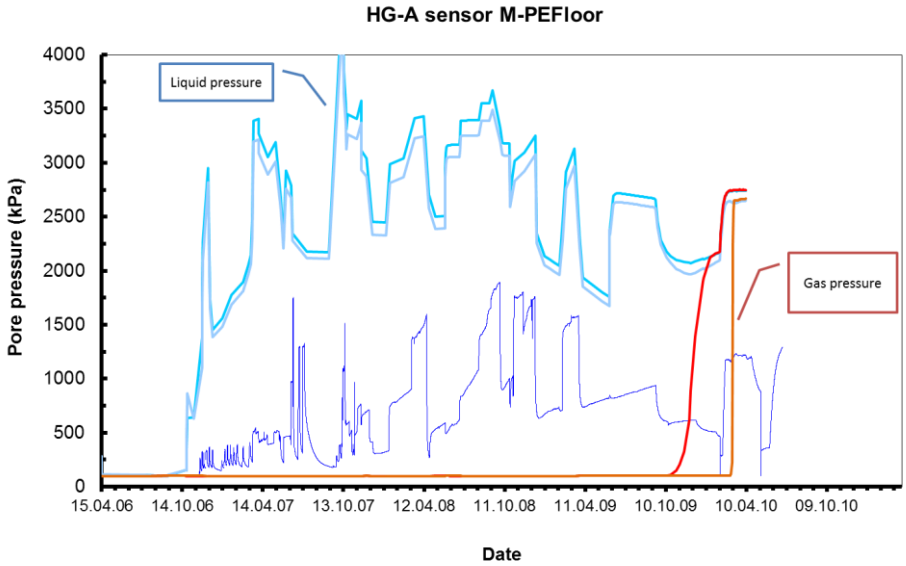

a)

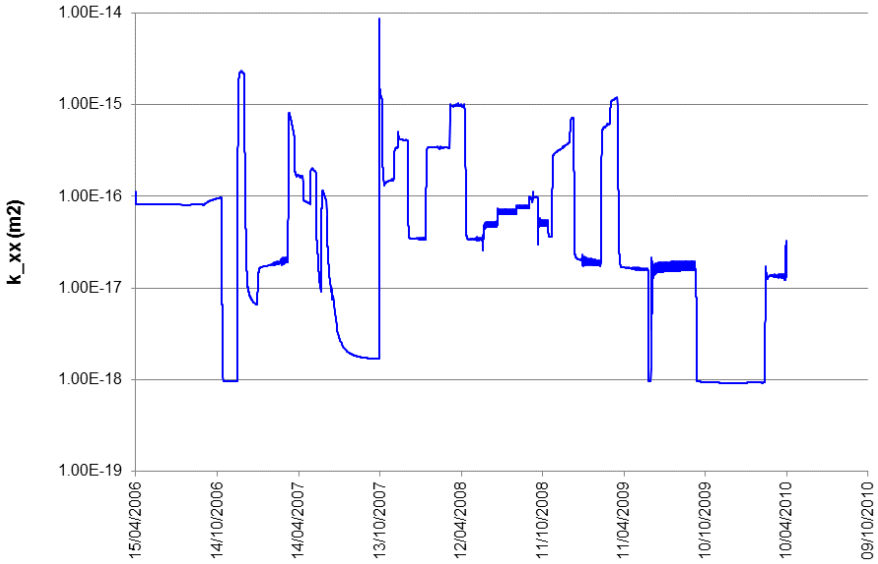

b)

Figure 4-4. Case 1 (sat): evolutions of: a) liquid and gas pressures; and b) intrinsic permeability.

Comments

Case 1 assumes initial saturation of the gravel. Computed liquid pressures are too high.

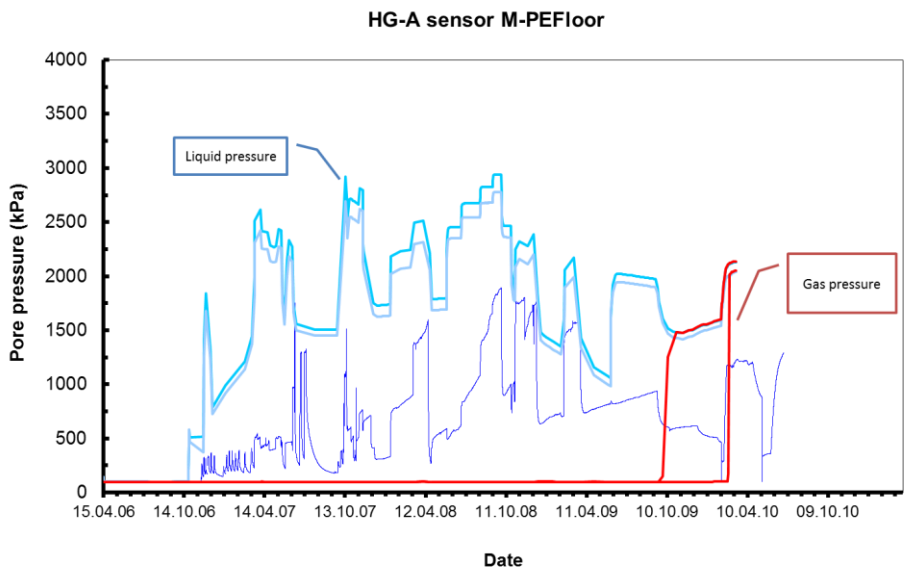

a)

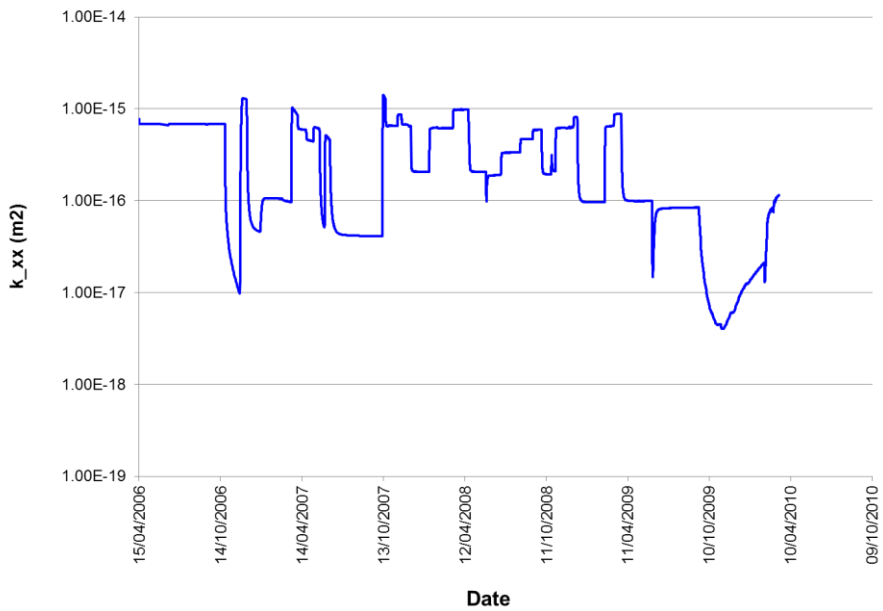

b)

Figure 4-5. Case 2 (sat): evolutions of: a) liquid and gas pressures; and b) intrinsic permeability.

Comments

With respect to case 1 (sat), the changes made were $\varepsilon_0^{EDZ} = -1.0\times10^{-3} \rightarrow -2.0\times10^{-3}$ and $b_{max}^{EDZ} = 1.0\times10^{-4} m \rightarrow 1.0\times10^{-5} m$. As a result, liquid pressures improve, but they are still too high.

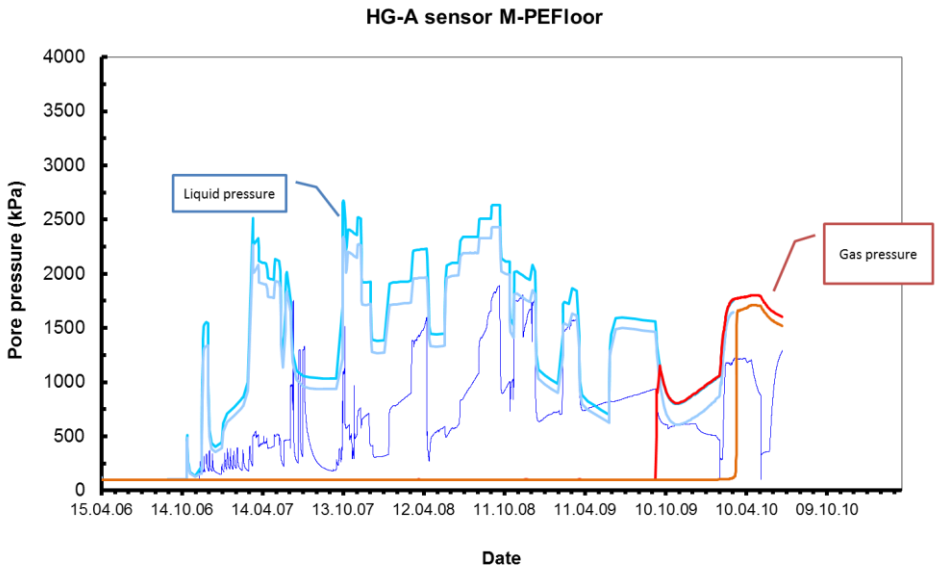

a)

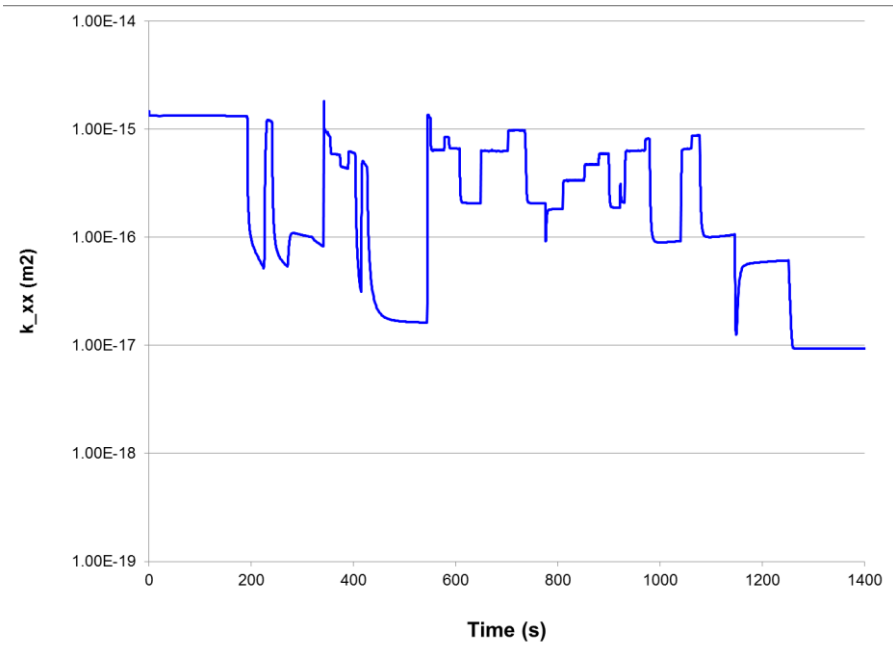

b)

Figure 4-6. Case 3 (sat): evolutions of: a) liquid and gas pressures; and b) intrinsic permeability.

Comments

With respect to case 2 (sat), the changes made were $k_{matrix}^{EDZ} = 1\times10^{-18} m^2 \rightarrow 1\times10^{-17} m^2$ and $\varepsilon_0^{EDZ} = -2.0\times10^{-3} \rightarrow -2.5\times10^{-3}$. As a result, liquid pressures are high, but not all the time.

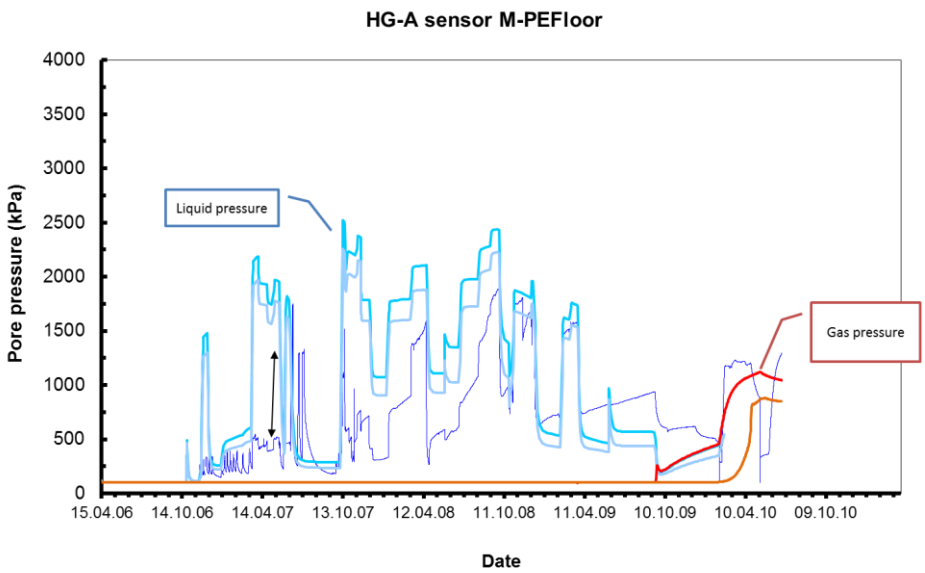

a)

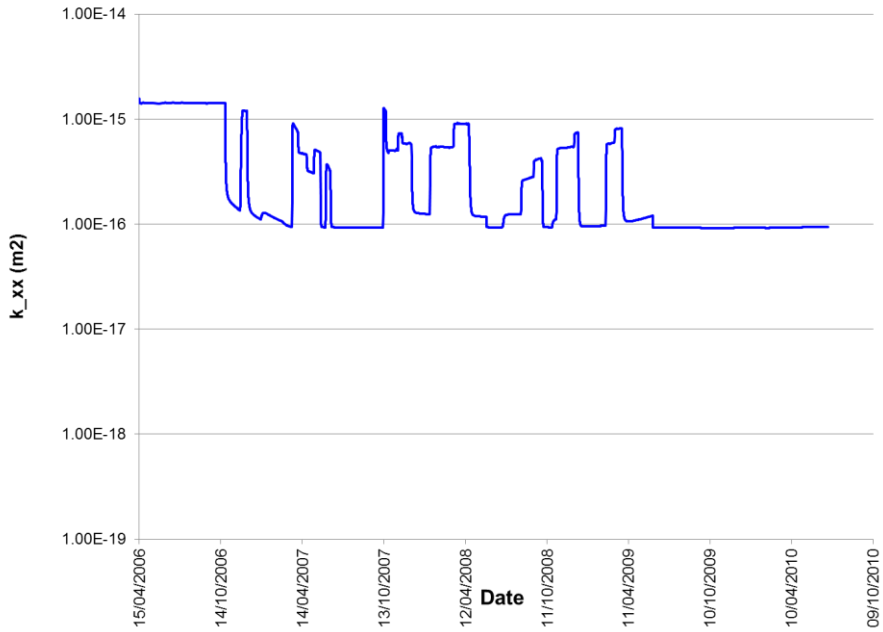

b)

Figure 4-7. Case 4 (sat): evolutions of: a) liquid and gas pressures; and b) intrinsic permeability.

Comments

With respect to case 3 (sat), the changes made were $k_{matrix}^{EDZ} = 1\times10^{-17} m^2 \rightarrow 1\times10^{-16} m^2$. As a result, liquid pressures are high but not all the time. Note that the intrinsic permeability reaches its lower bound, which is the permeability of the matrix.

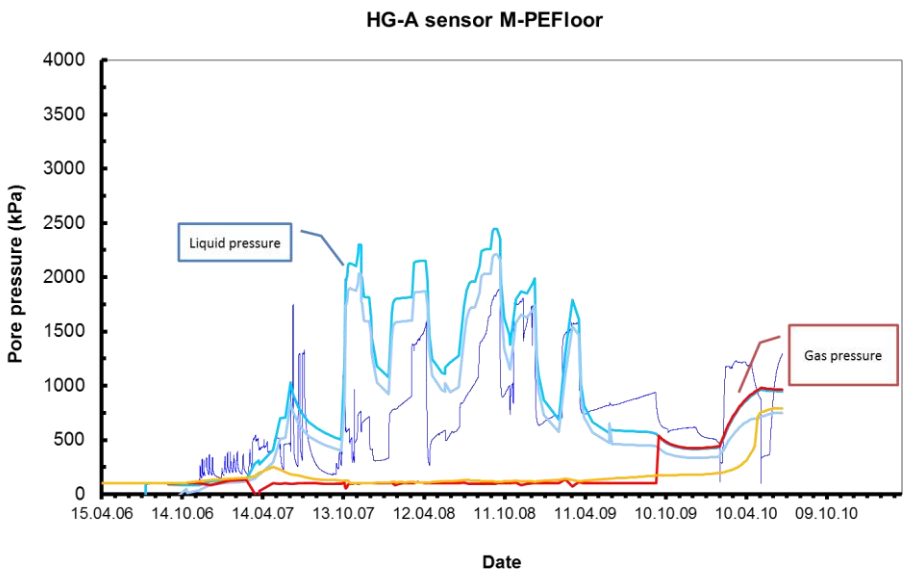

a)

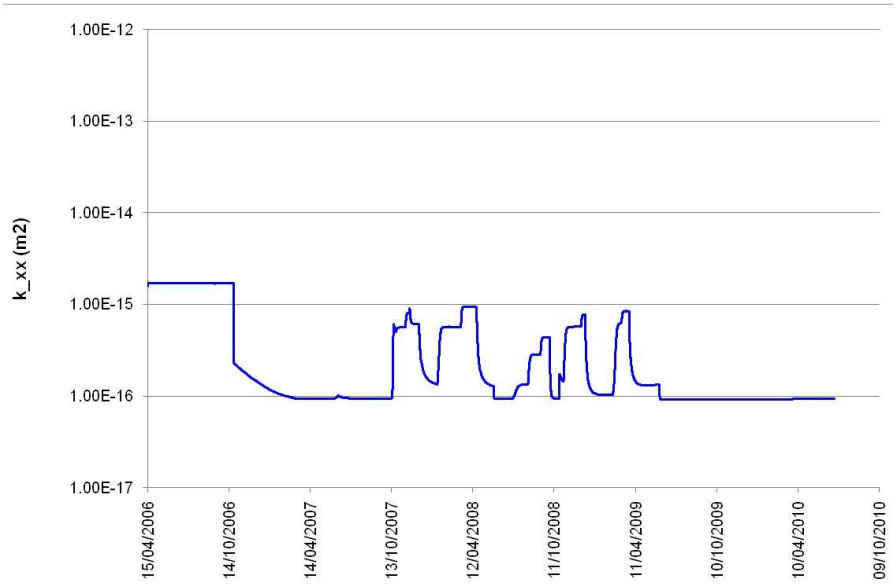

b)

Figure 4-8. Case 4 (unsat): evolutions of: a) liquid and gas pressures; and b) intrinsic permeability.

Comments

With respect to case 4 (sat), the changes made were to consider that the gravel was initially unsaturated. As a result, liquid pressures are high but not all the time. Note that the intrinsic permeability reaches its lower bound, which is the permeability of the matrix.

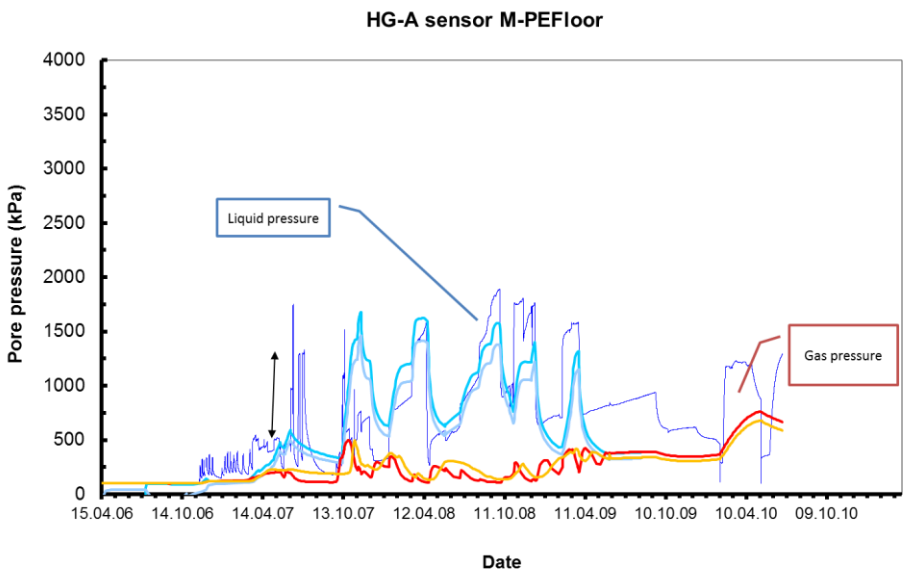

a)

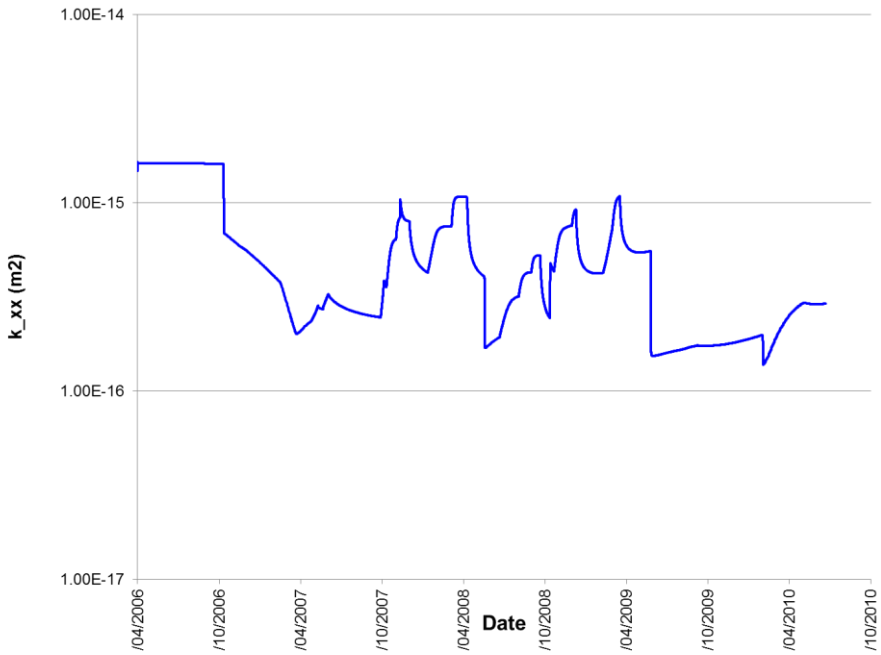

b)

Figure 4-9. Case 5 (unsat): evolutions of: a) liquid and gas pressures; and b) intrinsic permeability.

Comments

With respect to case 4 (unsat), the changes made were $k_{matrix} = 1\times10^{-16} m^2 \rightarrow 1\times10^{-17} m^2$ and $E'^{EDZ} = 400MPa \rightarrow 800MPa$. As a result, liquid pressures decrease and the intrinsic permeability does not reach its lower bound.

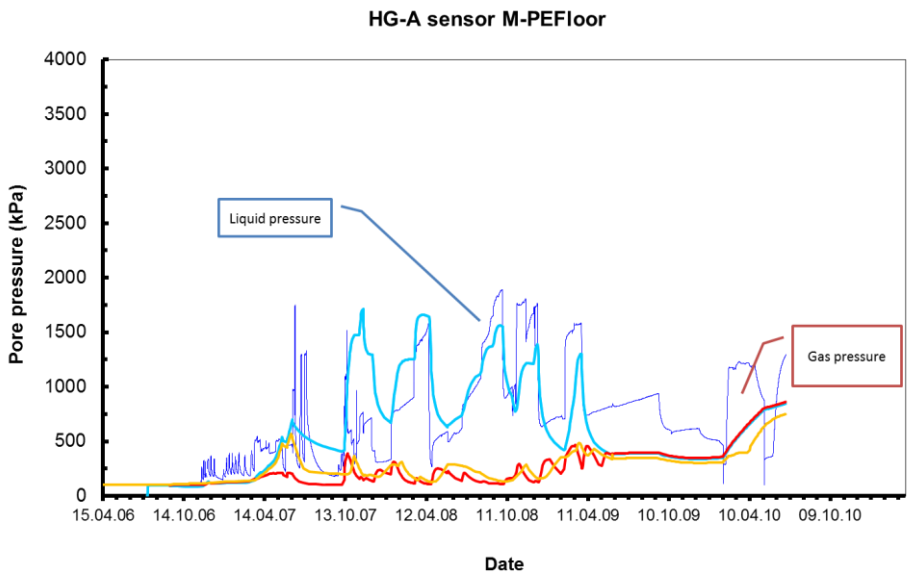

a)

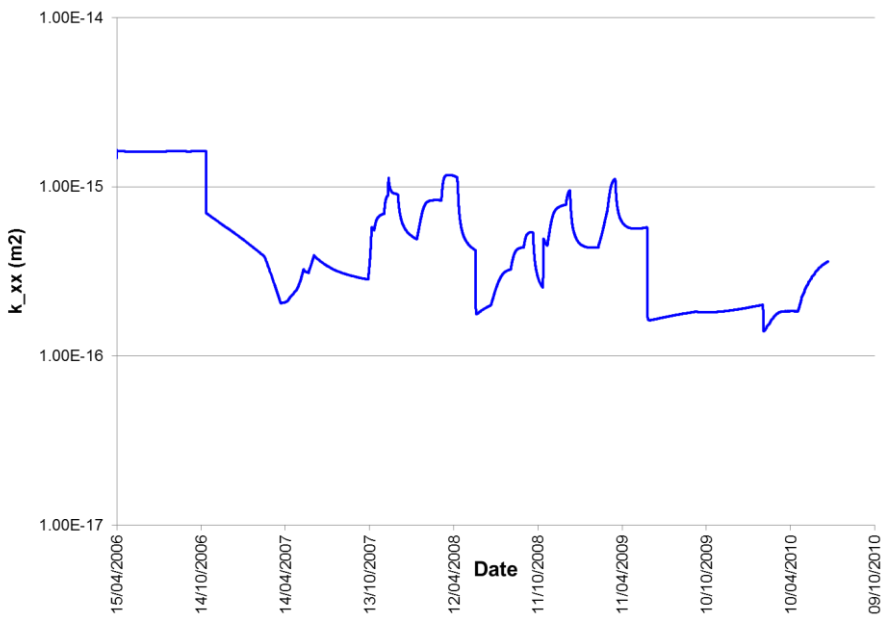

b)

Figure 4-10. Case 6 (unsat): evolutions of: a) liquid and gas pressures; and b) intrinsic permeability.

Comments

With respect to case 5 (unsat), the changes made were $A_g^{EDZ} = 100 \rightarrow 1$. As a result, gas pressures slightly improve. This case was considered to correspond to the best fit.

4.2.6 Best fit results

Besides the evolutions of the liquid and gas pressures compared with sensor M-PEFloor and the evolution of the intrinsic permeability in the EDZ close to the test section for the best fit case 6 (unsat) shown in Figure 4-10, the following figures show, at times 260 days, 350 days, 600 days, 700 days, 800 days, 1400 days and 1500 days, the distributions of:

- Volumetric deformation (positive values indicate compression)
- Liquid phase pressure
- Module of the liquid volumetric flow (in logarithmic scale)
- Gas phase pressure
- Module of the gas volumetric flow (in logarithmic scale)

Additionally, for each of those times, a scheme of the megapacker pressure evolution (green) and a scheme of the volumetric liquid injection rate evolution (blue) and gas injection rate evolution (red), each with a vertical dashed line indicating the corresponding time, are shown in order to facilitate the interpretation of the results. Because this stage of the modelling was focused on the liquid injection tests, a detailed liquid injection rate evolution was used, whereas a simplified gas injection rate evolution was used. A detailed gas injection rate evolution was used in the series of additional models (denoted G1, G2 and G3), that are presented later on.

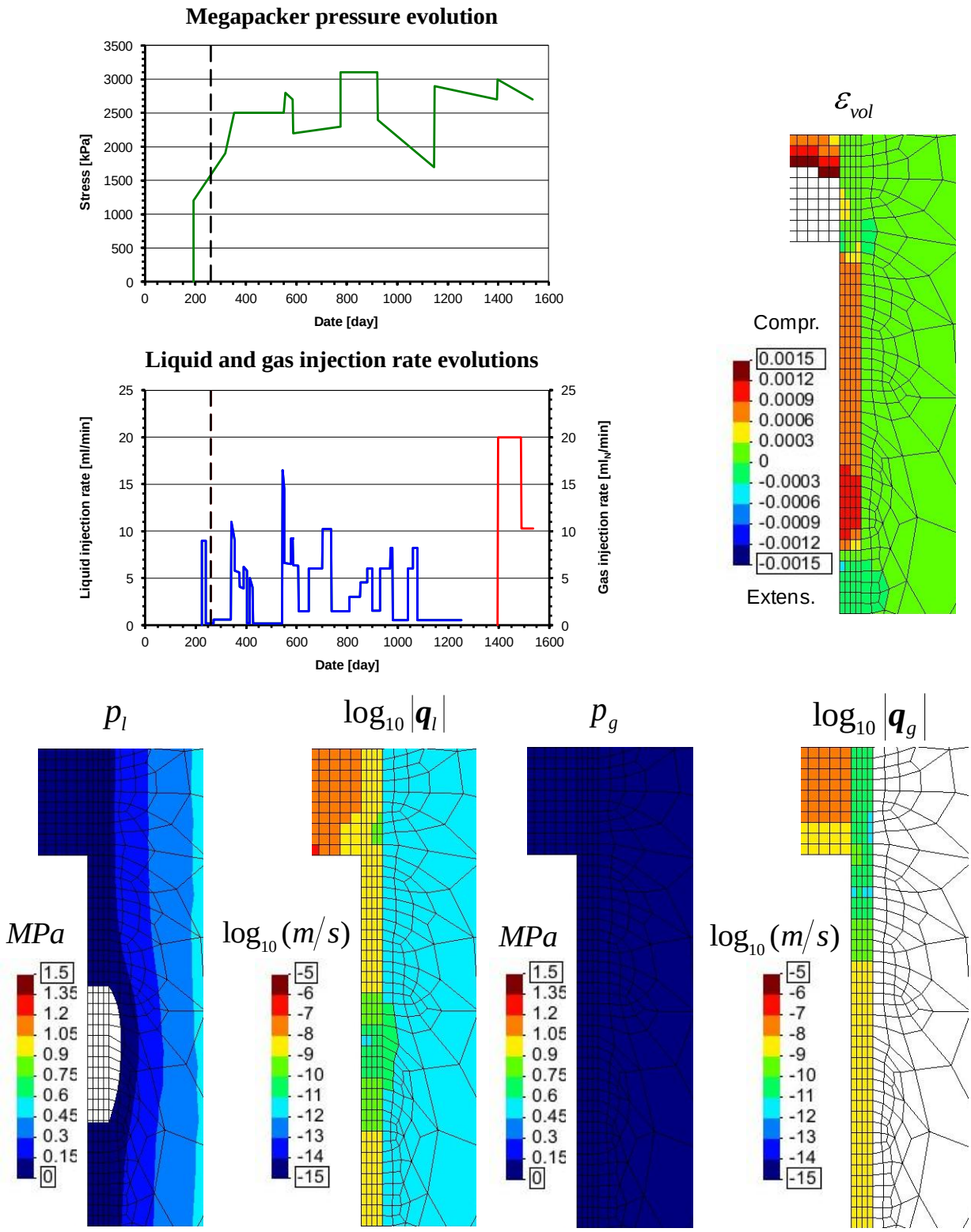

Figure 4-11a. Case 6 (unsat): distributions of some relevant fields near the half of the megapacker end close to the test section at $t = 260$ days .

Comments

Liquid and gas pressures are small, liquid and (dissolved) gas flow through the EDZ and compressions occur in the EDZ.

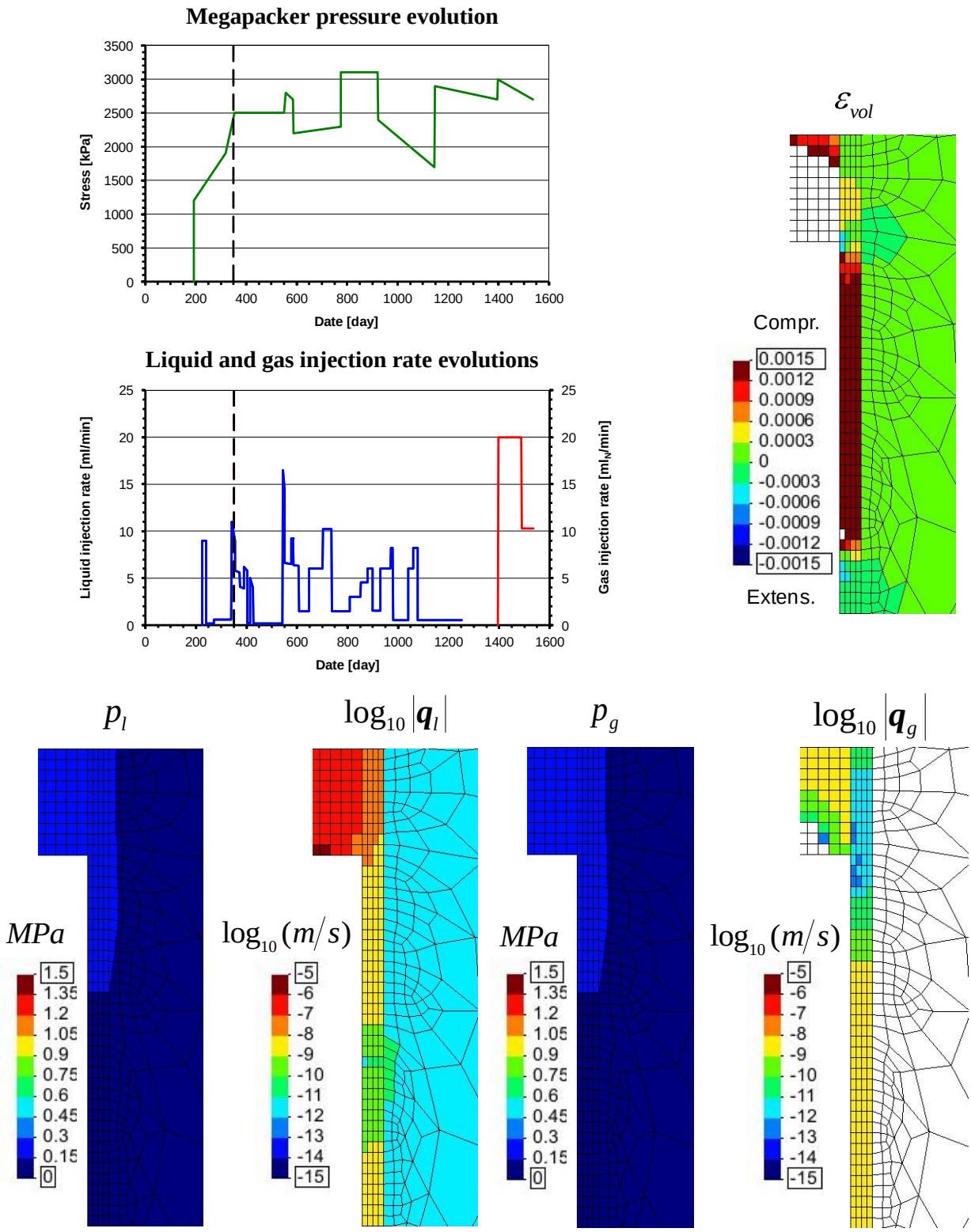

Figure 4-11b. Case 6 (unsat): distributions of some relevant fields near the half of the megapacker end close to the test section at $t = 350$ days.

Comments

Liquid and gas pressures increase slightly, liquid and gas fluxes increase slightly and there appear important compressions on the EDZ

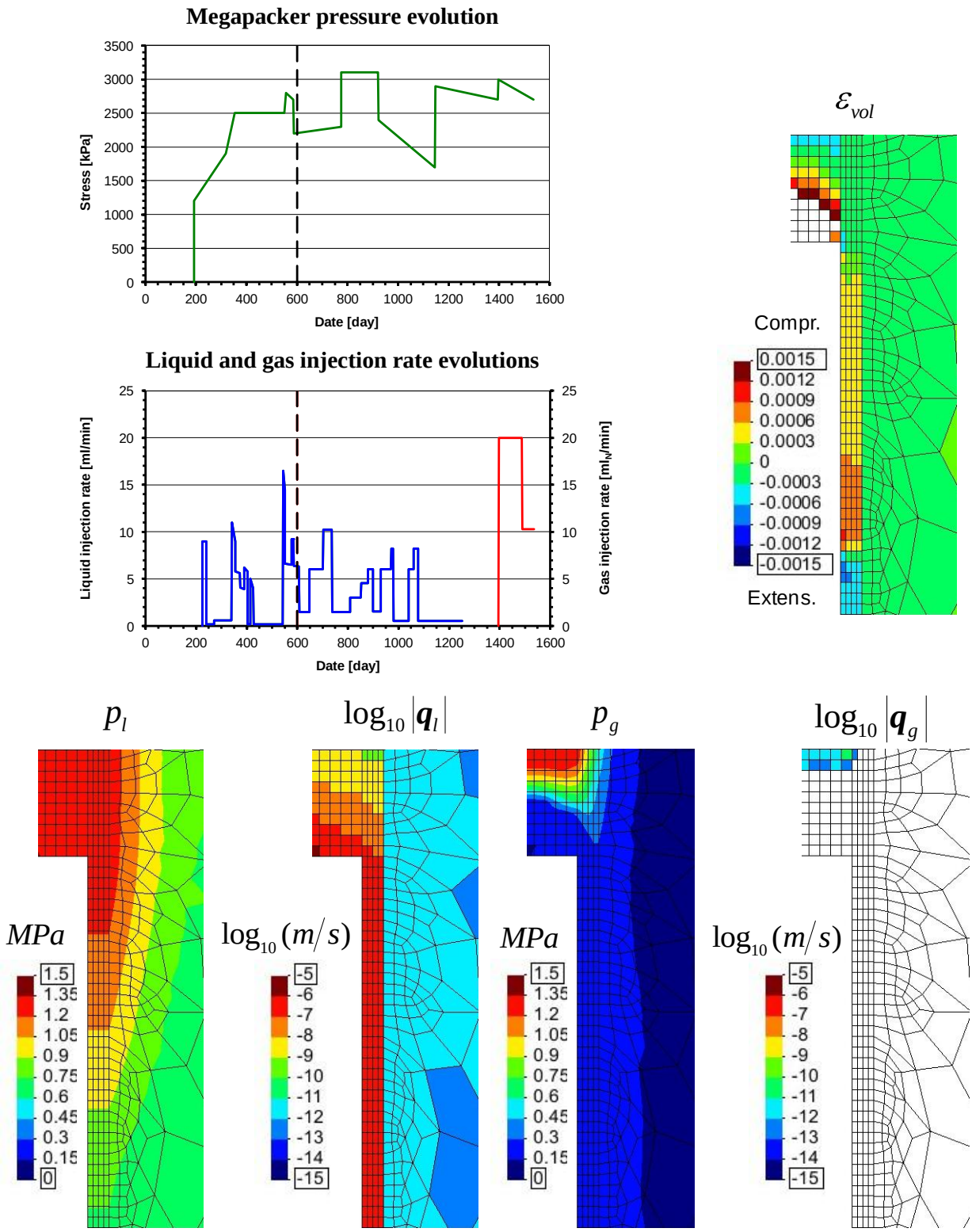

Figure 4-11c. Case 6 (unsat): distributions of some relevant fields near the half of the megapacker end close to the test section at $t = 600$ days.

Comments

Liquid and gas pressures increase (especially on the test section), there is an important flux of liquid flux, nearly no gas flux and compressions on the EDZ decrease.

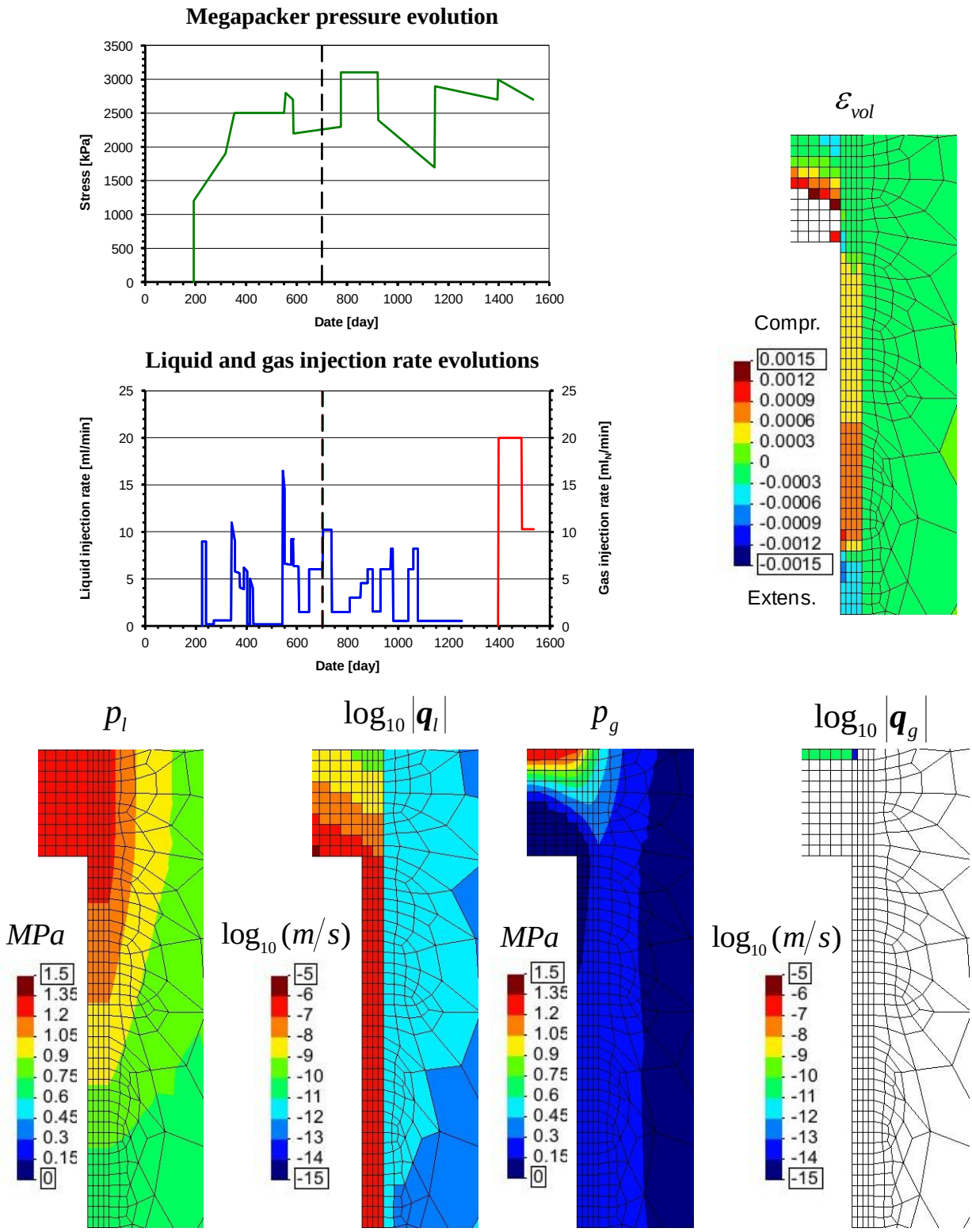

Figure 4-11d. Case 6 (unsat): distributions of some relevant fields near the half of the megapacker end close to the test section at $t = 700$ days.

Comments

Only small variations with respect to the previous figure occur.

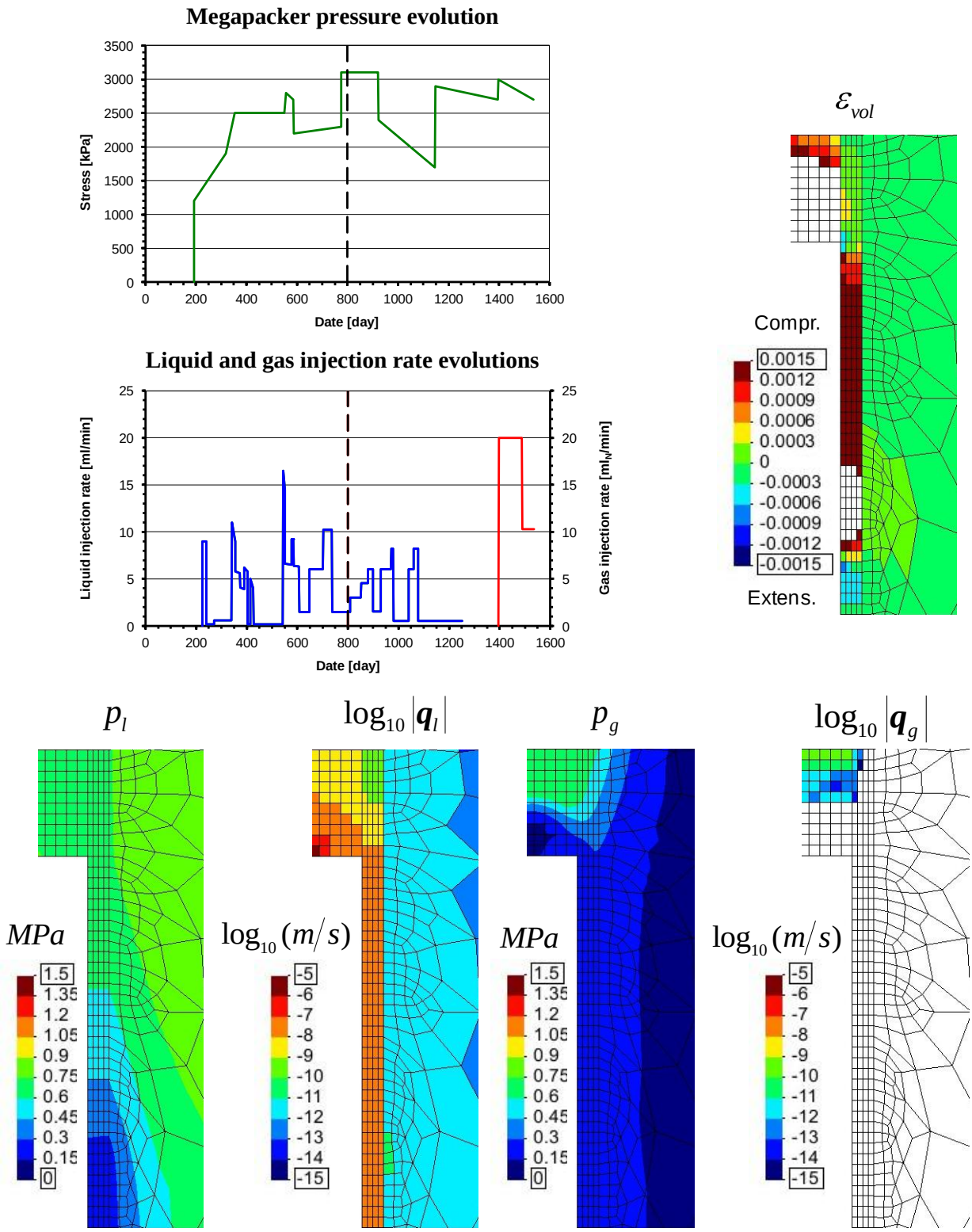

Figure 4-11e. Case 6 (unsat): distributions of some relevant fields near the half of the megapacker end close to the test section at $t = 800$ days.

Comments

Liquid and gas pressures decrease, the liquid flux decreases, nearly there is no gas flux and compressions increase on the EDZ.

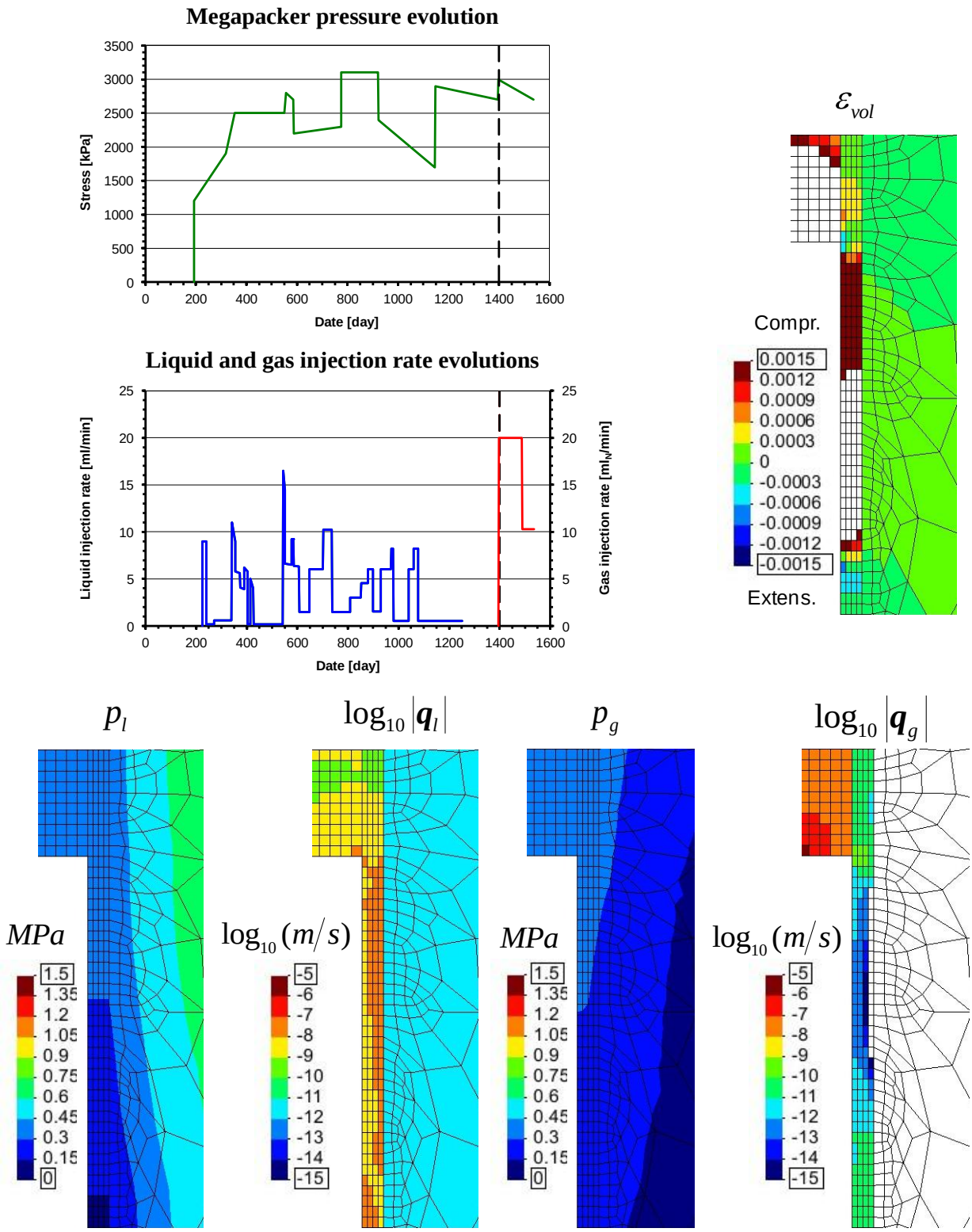

Figure 4-11f. Case 6 (unsat): distributions of some relevant fields near the half of the megapacker end close to the test section at $t = 1400$ days.

Comments

Liquid and gas pressures decrease, liquid flux increases slightly, there appear a gas flux (due to the gas injection tests) and compressions decrease slightly on the EDZ.

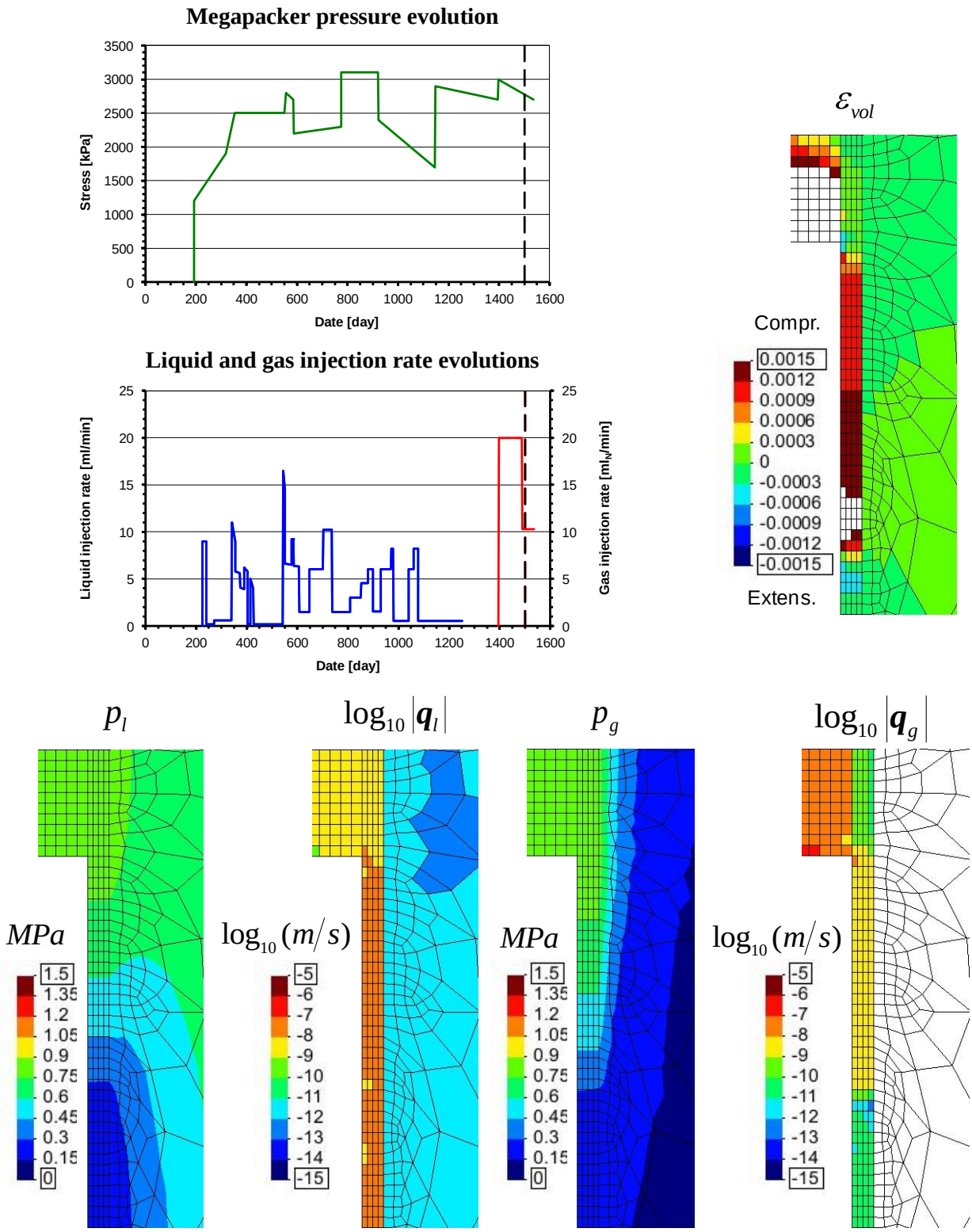

Figure 4-11g. Case 6 (unsat): distributions of some relevant fields near the half of the megapacker end close to the test section at $t = 1500$ days.

Comments

Liquid and gas pressures increase, liquid flux increases slightly, gas flux increases and volumetric deformations decrease on the EDZ.

4.2.7 Additional results

Since the model is axisymmetric and the gravity was neglected, it was difficult to get rid of the gas bubble present in the test section, due to an initially unsaturated state of the gravel and to the gas injection tests. In reality, gas tends to move towards the upper part of the test section and, due to the injection of liquid, gas was pushed away from the test section. In axisymmetric conditions, however, this is not possible.

As shown in Table 4-4, variations of the base model case 6 (unsat) were considered in order to improve the modeling results, by considering the polygonal approximations to the input protocols shown in Figure 4-1 (improved gas injection rate protocol) and by changing the location of the injection point into the test section from close to the megapacker to close to the tunnel end (to eliminate the gas entrapped at the tunnel end; recall that gravity is neglected) and incorporating venting before gas injection tests (before starting a gas injection test, liquid was circulated through the test section in order to eliminate entrapped gas). Note that in these additional cases the best fit parameters of case 6 (unsat) were used.

Table 4-4. Variations of case 6 (unsat).

Case	Description	Graphs
G1 (unsat)	Injection point near megapacker	Figure 4-12
G2 (unsat)	Injection point at tunnel end	Figure 4-13
G3 (unsat)	Injection point near megapacker and venting	Figure 4-14

The effects of the changes incorporated in these additional cases are shown for the evolution of liquid and gas pressures in the test section and for the evolution of the intrinsic permeability in the EDZ, close to the megapacker end in contact with the test section. These figures may be compared with the corresponding ones obtained during the parameter calibration.

The problem with the entrapped gas may be appreciated in Figure 4-15, which shows the distribution of the degree of saturation at 1250 days for the three cases considered. The entrapped gas in the test section is clearly seen in cases G1 and G3.

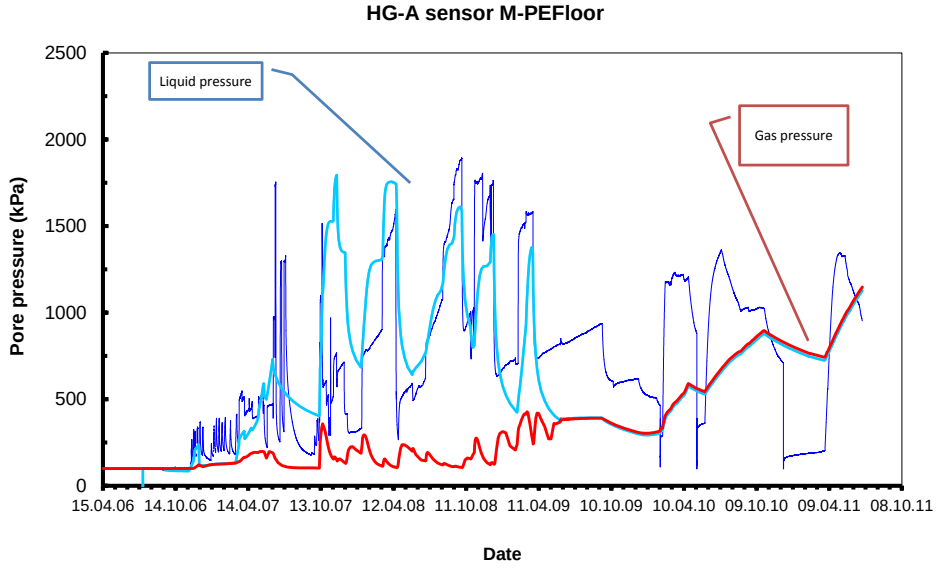

a)

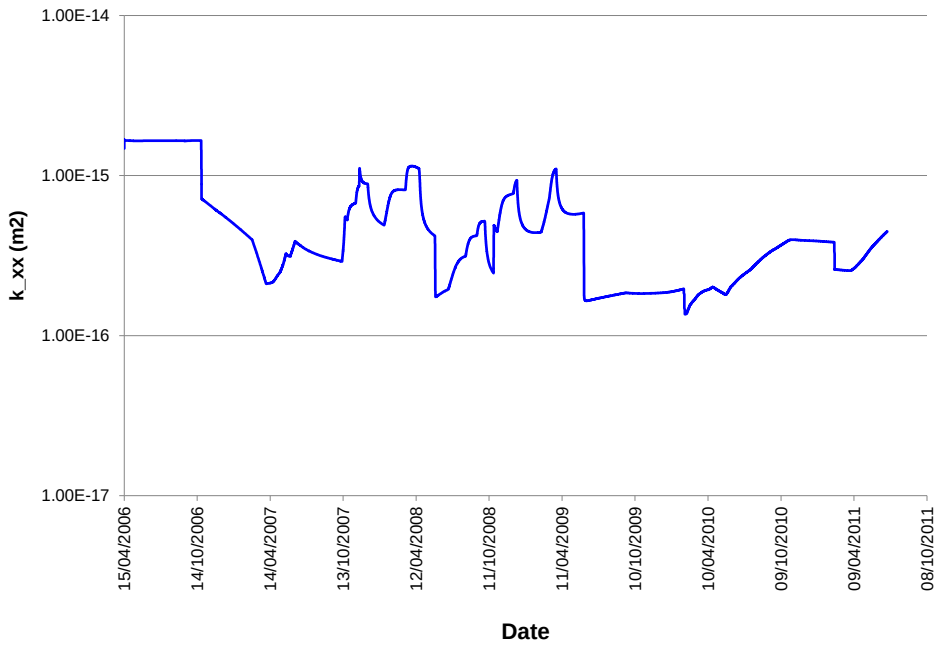

b)

Figure 4-12. Case G1 (injection point near megapacker).

Comments

Gas pressure remains small until desaturation occurs due to the gas injection tests.

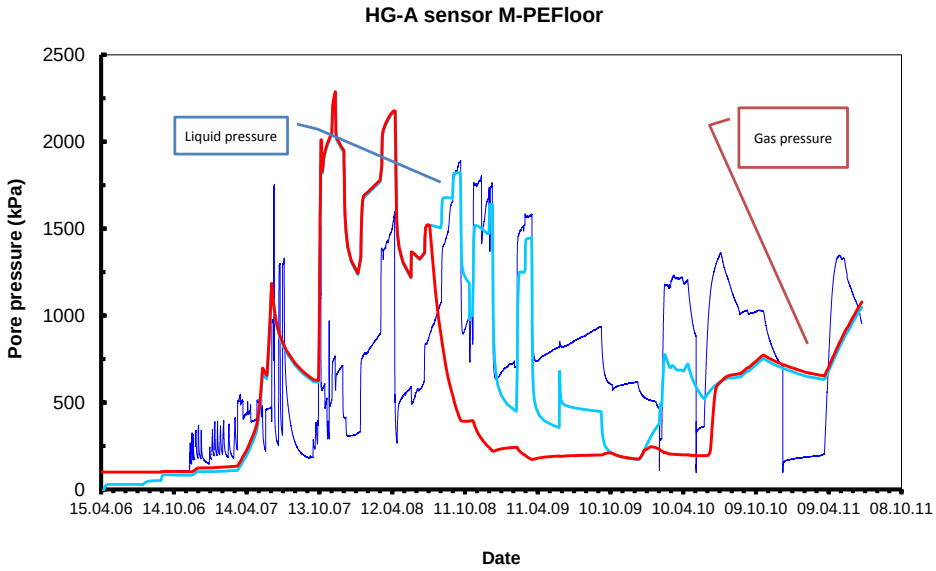

a)

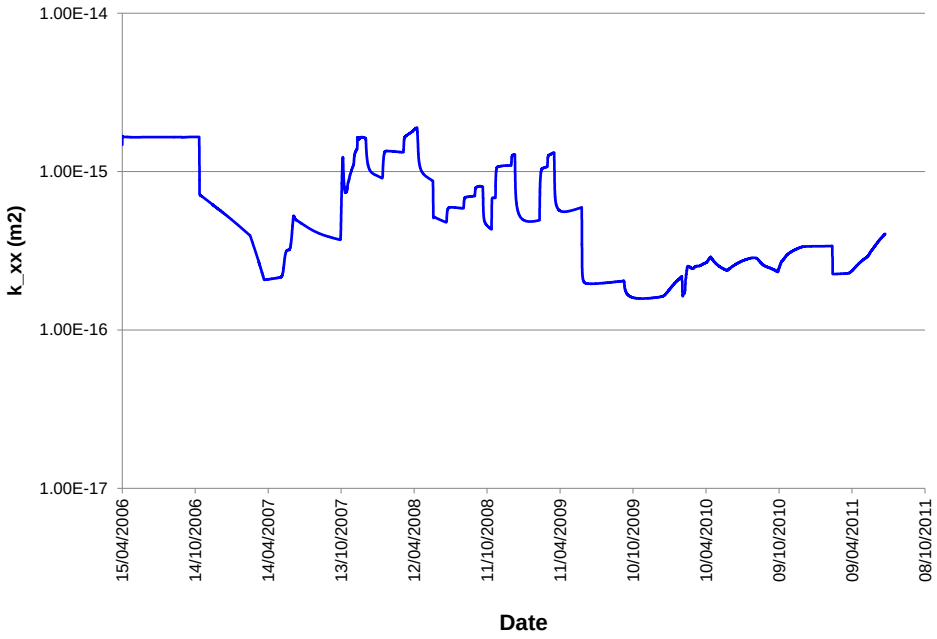

b)

Figure 4-13. Case G2 (injection point at tunnel end).

Comments

Gas pressure is increased during the first part of the considered period.

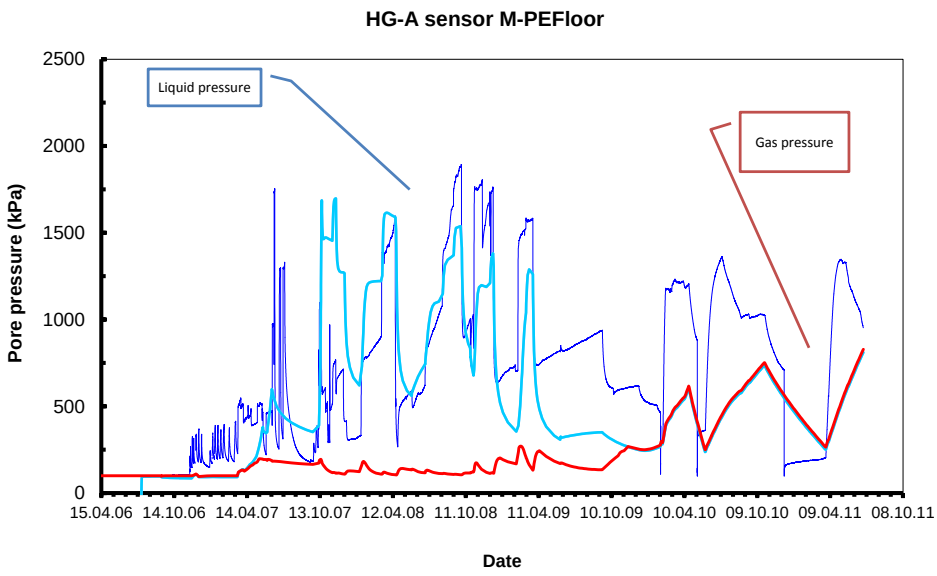

a)

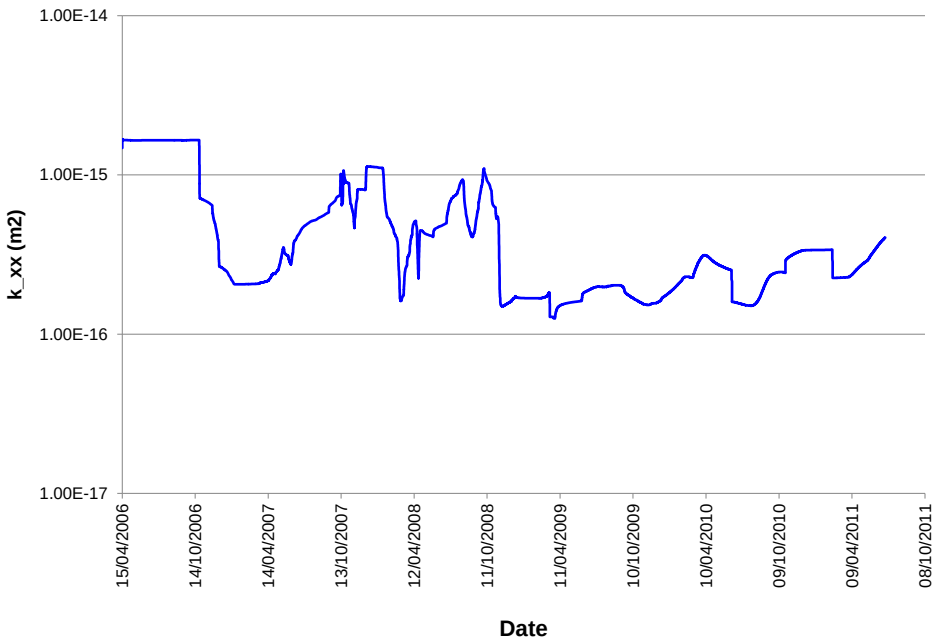

b)

Figure 4-14. Case G3 (Injection point near megapacker and venting).

Comments

Temporal decreases of the liquid and gas pressures occur during the venting process. This case corresponds to the best predictions obtained using the 2D axisymmetric model.

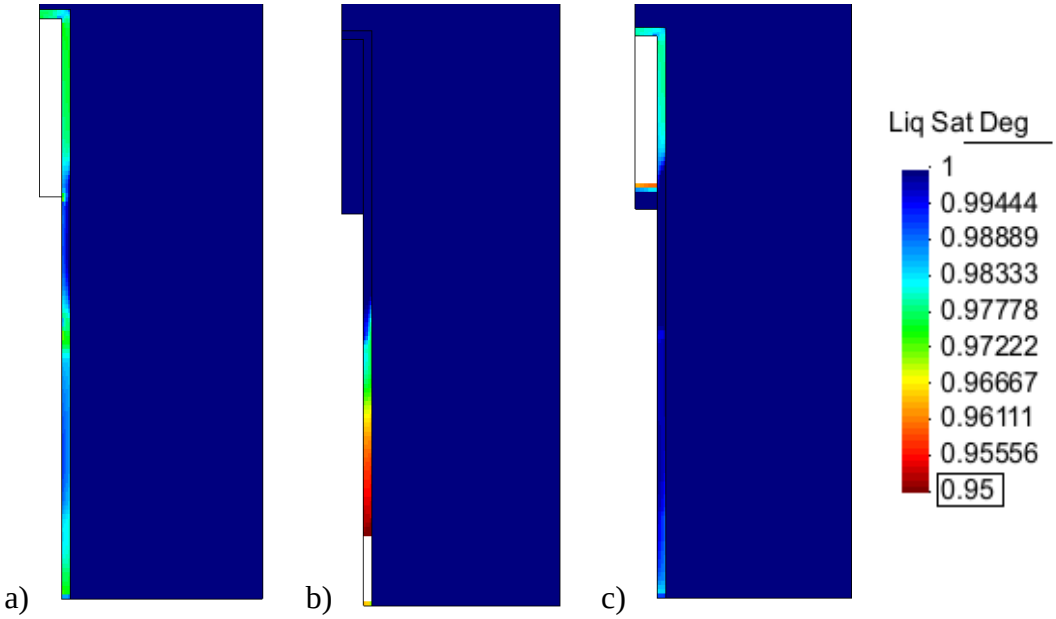

Figure 4-15. Gas entrapped during water flow which is not completely eliminated. Distributions of degree of saturation at 1250 days: a) case G1; b) case G2; and c) case G3.

Comments

In cases G1 and G3 (injection point near the megapacker), entrapped gas in the test section is apparent. In case G2 (injection point at the tunnel end), there is no entrapped gas in the test section.

4.3 1D simplified model

A comprehensive description of the formulation and the numerical solution of this model may be found in Alcoverro et al. (2012). In this section, a summary of the main features of the 1D simplified model and the obtained results, including a parameter sensitivity analysis, is presented.

By use of simplifying assumptions, it is possible to reduce the problem to a coupled system of two differential equations in two unknown functions of a geometric variable z defined on a 1D domain, representing the part of the EDZ in contact with the megapacker, and of time t. Besides considering the liquid phase density ρ_l to be independent of the liquid phase pressure p_l, the aforementioned assumptions are

Mechanical. Both on the EDZ and on the Opalinus clay, it will be assumed that (1) there is axisymmetry about the tunnel axis (z axis); (2) there are no volume forces (gravity is neglected); and (3) slices $z = const$ move independently and in plane strain.

Hydraulic. Both on the EDZ and on the Opalinus clay, it will be assumed that (1) there is axisymmetry about the tunnel axis (z axis); and (2) there are no volume forces (gravity is neglected). Furthermore, on the EDZ, it will be assumed that $(3)^{EDZ}$ the flows of the liquid phase and of the gas phase are parallel to the tunnel axis (z axis); and, on the Opalinus clay, it will be assumed that $(3)^{OPA}$ there is no gas phase (saturated state), there is no flow of the liquid phase (undrained conditions) and there is no air in the liquid phase.

In essence, slices perpendicular to the tunnel axis can move independently and in plane strain but they are hydraulically connected. This allows restricting the model to the zone between two planes perpendicular to the tunnel axis and passing through the megapacker ends. Using the simplifying assumptions, it may be proven that, on the one hand, the pressure of the liquid phase and the pressure of the gas phase depend only on the axial coordinate and on time and, on the other hand, the balance of momentum in both the EDZ and in the (undamaged) Opalinus clay may be solved in closed form in terms of those pressures. Consequently, the field equations reduce to the balance of mass of the water species and the balance of mass of the air species, with the pressure of the liquid phase and the pressure of the gas phase as unknown fields of the axial coordinate and time. This coupled system of equations is solved using the FEM. Once the two unknown functions of the geometric 1D variable and of time are known, all the field variables both on the Opalinus clay and on the EDZ are determined in closed form using those two unknown functions.

4.3.1 Geometry and coordinate system

As already mentioned, the modelled zone is located between two planes perpendicular to the tunnel axis and passing through both ends of the megapacker and extends up to the infinity. However, because the problem can be reduced to a 1D geometry (a segment 3.00 m long, the length of the megapacker), the finite element mesh was also 1D. The mesh was made of 10 linear finite elements (each 0.30 m long) and 11 nodes. A scheme of the modelled zone and the FEM mesh are shown in Figure 4-16 below.

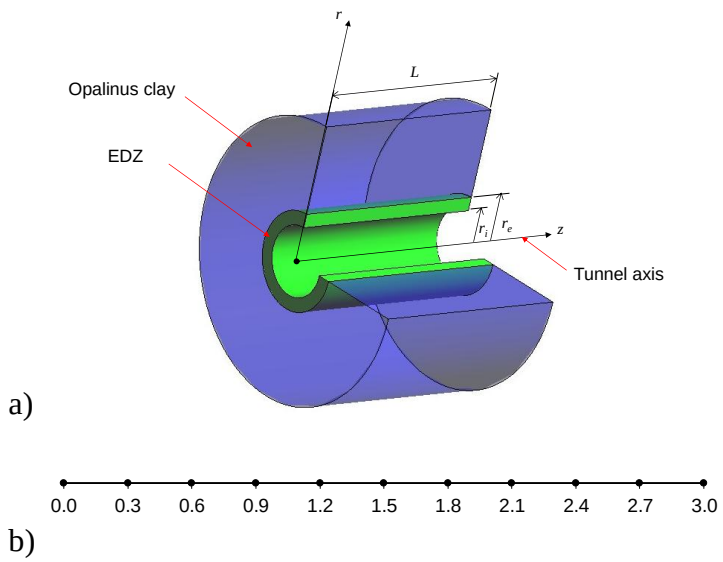

Figure 4-16. a) Geometry around the megapacker section and system of coordinates; the modeled zone is limited by two planes perpendicular to the tunnel axis and passing through both ends of the megapacker (the Opalinus clay extends up to the infinity); materials: (undamaged) Opalinus clay (blue) and EDZ (green); the tunnel axis is the axisymmetry axis; and b) finite element mesh.

4.3.2 Initial and boundary conditions

The following values have been assumed for the initial conditions: (1) porosity $\phi^0 = 0.12$; (2) solid skeleton displacements $u_r^0 = 0.0\,m$, $u_y^0 = 0.0\,m$, $u_\theta^0 = 0.0\,m$; and (3) principal stresses $\sigma_r^0 = -5.5\,MPa$, $\sigma_y^0 = -2.5\,MPa$, $\sigma_\theta^0 = -5.5\,MPa$.

The (point) boundary conditions at the boundary close to the test section are mass injection rates of species water and of species air derived from the liquid phase volume injection rate and of the gas phase volume injection rate protocols. The boundary conditions at the boundary close to the liner are generalized conditions involving the mass rates of the liquid phase and of the gas phase and the values of the external pressures of the liquid phase and of the gas phase. These generalised conditions, that include two further model parameters, try to compensate for the fact that the simplifying assumptions do not hold near the megapacker ends. The quite high values of 1000 1/(MPa·m^2) chosen for these parameters tend to impose the external (at the Mont Terri URL) values of liquid phase pressure and gas phase pressure at the considered boundary. It should be mentioned that the megapacker pressure protocol is transformed into a body term on the 1D domain, so it is not a boundary condition.

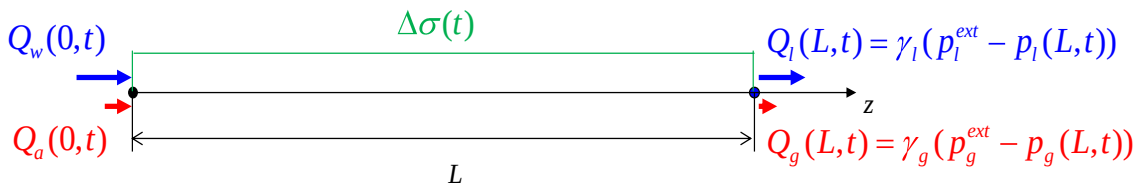

Figure 4-17. The 1D domain represents the EDZ in front of the megapacker, which is bounded to the left by the test section and to the right by the liner section. Generalised boundary conditions are applied at the right boundary point.

4.3.3 Material models

Two materials have been considered in the model: EDZ and (undamaged) Opalinus clay, since the gravel in the test section was not included in the modelled zone, and its effect was taken into account as a boundary condition. Their positions and dimensions in the modelled zone are indicated in Figure 4-16 a) using different colours. The colour and constitutive laws used for each material are summarized below. It should be mentioned that, although the field equations are the balances of mass of species water and of species air, these equations depend also on the properties of the Opalinus clay.

EDZ. (green) Linear poroelastic, undrained conditions.

Opalinus clay. (blue) Linear poroelastic, Van Genuchten retention curve, isotropic permeability, Van Genuchten liquid phase relative permeability and generalised power law gas phase relative permeability.

Table 4-5 shows the values used for the constitutive parameters corresponding to the best fit, which are the same as those used in cases 6 (unsat), G1 (unsat), G2 (unsat) and G3 (unsat) of the 2D axisymmetric model.

Table 4-5. Values used for the constitutive parameters.

Elastic effective properties					
E'^{OPA}	4.0×10^{3}	MPa	ν'^{OPA}	0.30	–
E'^{EDZ}	0.8×10^{3}	MPa	ν'^{EDZ}	0.30	–
Water retention curve					
λ^{EDZ}	0.33	–	P_0^{EDZ}	0.243	MPa
Intrinsic permeability					
k_{matrix}^{EDZ}	1.0×10^{-17}	m^2			
b_0^{EDZ}	1.0×10^{-7}	m	b_{max}^{EDZ}	1.0×10^{-5}	m
a^{EDZ}	1.0×10^{-3}	m	ε_0^{EDZ}	-2.5×10^{-3}	–
Relative permeabilities					
λ_l^{EDZ}	0.33	–			
A_g^{EDZ}	1.00	–	n_g^{EDZ}	3.00	–
Diffusion coefficients					
D_l^{EDZ}	1.4×10^{-4}	m^2/s	Q_l^{EDZ}	2.54×10^{-2}	$MPa\cdot m^3/mol$
D_g^{EDZ}	5.9×10^{-12}	$m^2/s\cdot MPa\cdot°K^{-Q_g}$	Q_g^{EDZ}	2.3	–

4.3.4 Calculation phases

In this model only the test input protocol needs to be applied. This was done by prescribing the evolutions of the megapacker pressure and of the liquid and gas injection rates, which were transformed into mass rates of species water and species air.

4.3.5 Sensitivity analysis results

A sensitivity analysis with respect to a number of parameters was carried out for the liquid injection tests, using an early (one phase flow) version of the 1D simplified model. Table 4-6 below shows the model parameters that were varied, indicating the couple of values considered. The corresponding changes induced in the evolution of the liquid phase pressure at the test section are shown in the accompanying figures.

Table 4-6. Model parameters considered in the sensitivity analysis.

case	parameter	value 1	value 2	units	graph
1	E'^{OPA}	4000	8000	MPa	Figure 4-18
2	E'^{EDZ}	400	800	MPa	Figure 4-19
3	k_{matrix}^{EDZ}	1×10^{-16}	2×10^{-16}	m^2	Figure 4-20
4	b_0^{EDZ}	1×10^{-7}	2×10^{-7}	m	Figure 4-21
5	a^{EDZ}	1×10^{-3}	2×10^{-3}	m	Figure 4-22
6	b_{max}^{EDZ}	1×10^{-5}	2×10^{-5}	m	Figure 4-23
7	$\varepsilon_{vol,0}^{EDZ}$	-2.5×10^{-3}	-5.0×10^{-3}	–	Figure 4-24
8	r_e	0.70	0.90	m	Figure 4-25

Note that r_e, the external radius of the EDZ (a geometric model parameter), has also been varied. Since the thickness of the EDZ is $r_e - r_i$, where $r_i = 0.50\,\text{m}$ is the internal radius of the EDZ (the tunnel radius), $r_e = 0.70\,\text{m}$ corresponds to a thickness of the EDZ of 0.20 m and $r_e = 0.90\,\text{m}$ corresponds to a thickness of the EDZ of 0.40 m.

From the aforementioned figures, it may be concluded that

- $E'^{OPA} = 4000MPa \rightarrow 8000MPa$ increases p_l at the test section.
- $E'^{EDZ} = 400MPa \rightarrow 800MPa$ strongly decreases p_l at the test section.
- $k_{matrix}^{EDZ} = 1\times10^{-16}m^2 \rightarrow 2\times10^{-16}m^2$ decreases p_l at the test section.
- $b_0^{EDZ} = 1\times10^{-7}m \rightarrow 2\times10^{-7}m$ slightly decreases p_l at the test section.
- $a^{EDZ} = 1\times10^{-3}m \rightarrow 2\times10^{3}m$ decreases p_l at the test section.
- $b_{max}^{EDZ} = 1\times10^{-5}m \rightarrow 2\times10^{-5}m$ has no influence on p_l at the test section.
- $\varepsilon_{vol,0}^{EDZ} = -2.5\times10^{-3} \rightarrow -5.0\times10^{5}$ strongly decreases p_l at the test section.
- $r_e = 0.70m \rightarrow 0.90m$ strongly decreases p_l at the test section.

$E'^{OPA} = 4000\ MPa \quad \rightarrow \quad E'^{OPA} = 8000\ MPa$

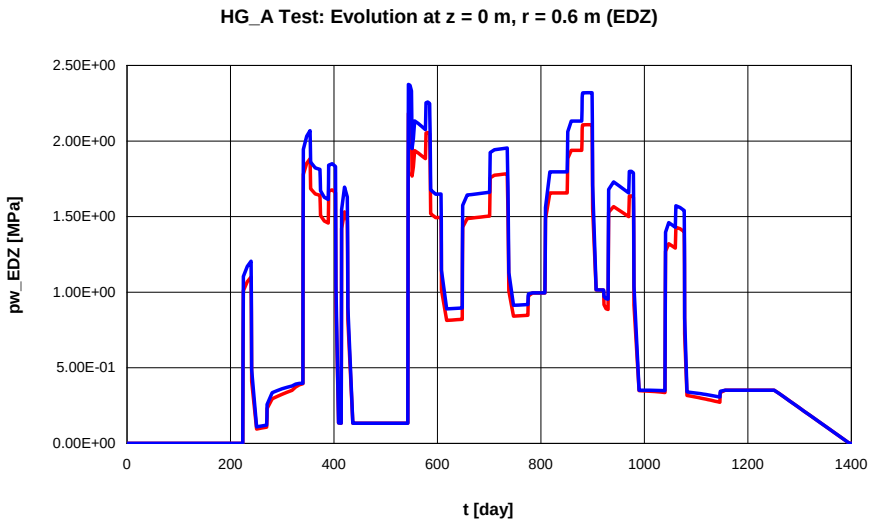

Figure 4-18. Variation of the evolution of the liquid phase pressure at the test section end with respect to E'^{OPA}.

$E'^{EDZ} = 400\ MPa \quad \rightarrow \quad E'^{EDZ} = 800\ MPa$

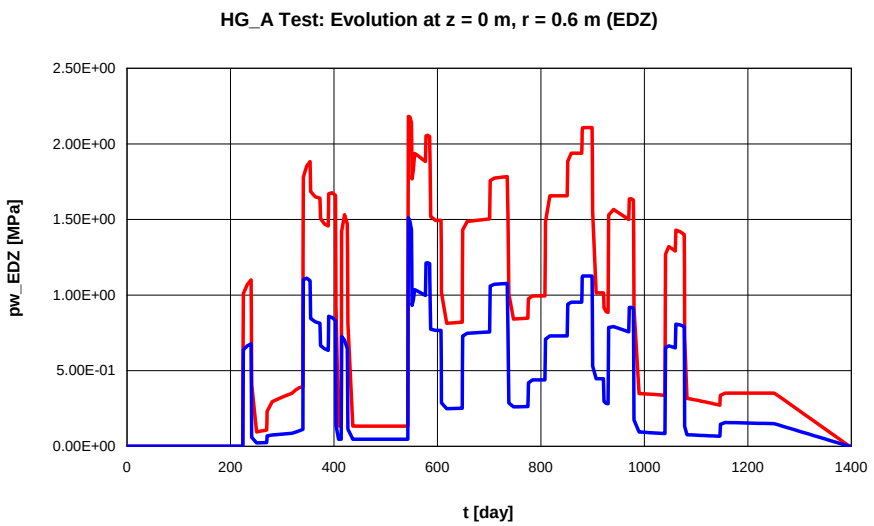

Figure 4-19. Variation of the evolution of the liquid phase pressure at the test section end with respect to E'^{EDZ}.

$k_{matrix}^{EDZ} = 1\times10^{-16}\ m^2 \quad \rightarrow \quad k_{matrix}^{EDZ} = 2\times10^{-16}\ m^2$

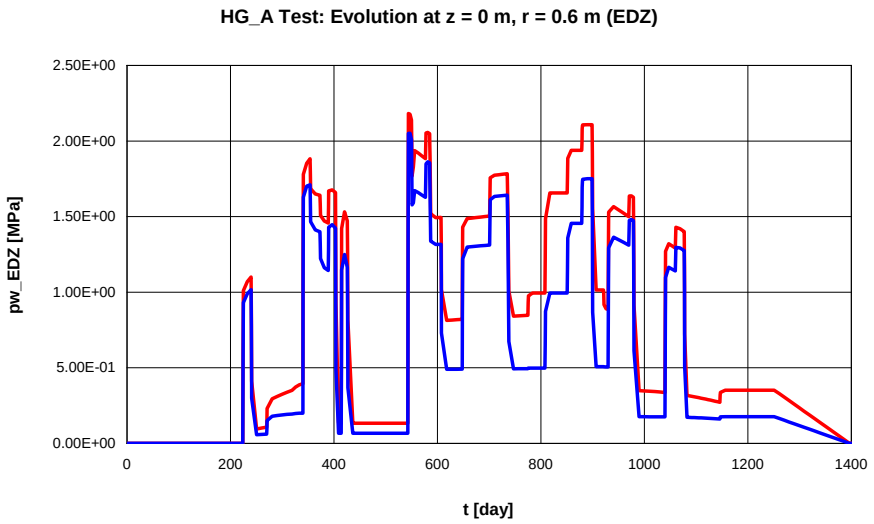

Figure 4-20. Variation of the evolution of the liquid phase pressure at the test section end with respect to k_{matrix}^{EDZ}.

$b_0^{EDZ} = 1\times10^{-7}\ m \quad \rightarrow \quad b_0^{EDZ} = 2\times10^{-7}\ m$

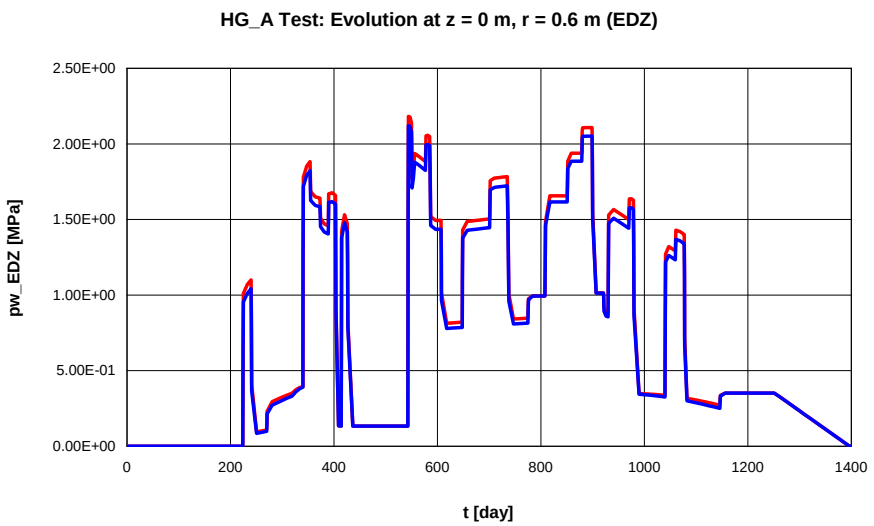

Figure 4-21. Variation of the evolution of the liquid phase pressure at the test section end with respect to b_0^{EDZ}.

$a^{EDZ} = 1\times10^{-3}\ m \quad \rightarrow \quad a^{EDZ} = 2\times10^{-3}\ m$

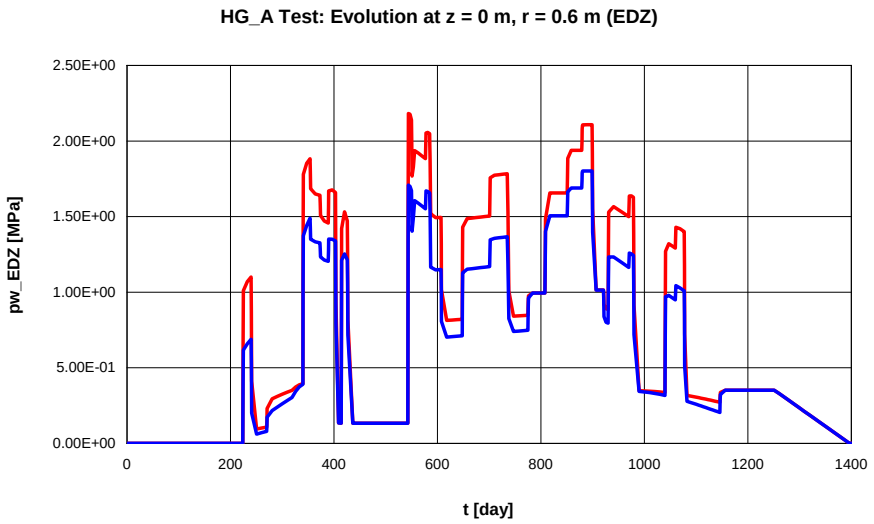

Figure 4-22. Variation of the evolution of the liquid phase pressure at the test section end with respect to a^{EDZ} .

$b_{\max}^{EDZ} = 1\times10^{-5}\ m \quad \rightarrow \quad b_{\max}^{EDZ} = 2\times10^{-5}\ m$

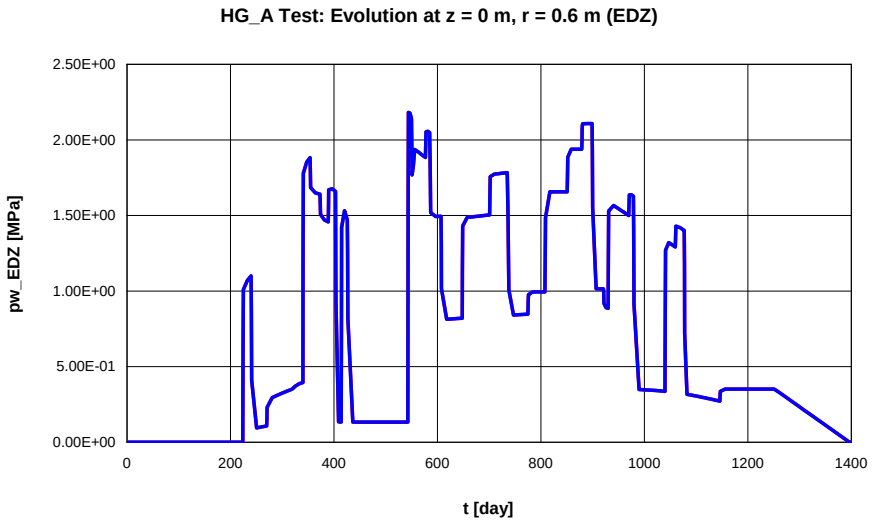

Figure 4-23. Variation of the evolution of the liquid phase pressure at the test section end with respect to b_{max}^{EDZ} .

$\varepsilon_{vol,0}^{EDZ} = -2.5\times10^{-3} \quad \rightarrow \quad \varepsilon_{vol,0}^{EDZ} = -5.0\times10^{-3}$

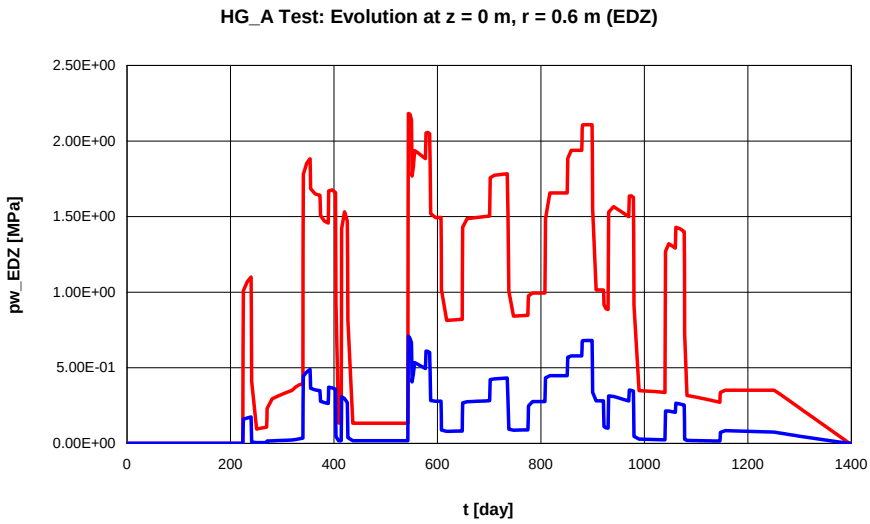

Figure 4-24. Variation of the evolution of the liquid phase pressure at the test section end with respect to $\varepsilon_{vol,0}^{EDZ}$.

$r_e = 0.70\ m \quad \rightarrow \quad r_e = 0.90\ m$

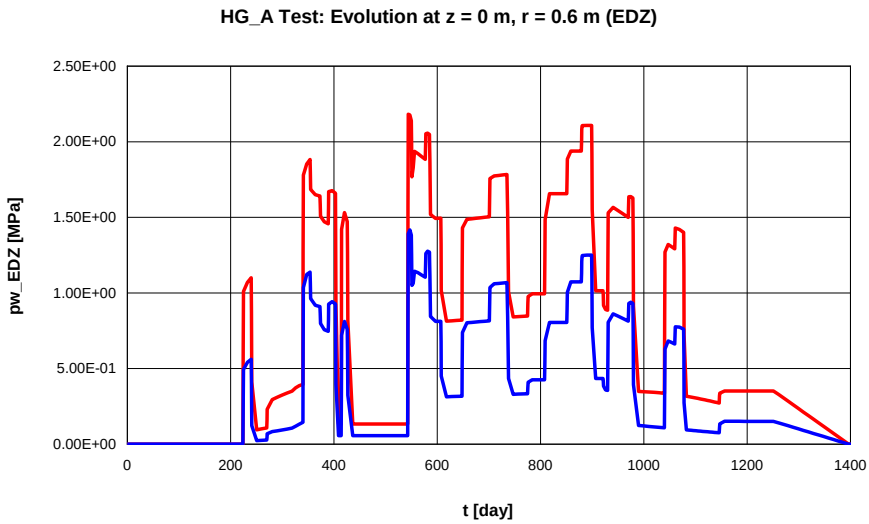

Figure 4-25. Variation of the evolution of the liquid phase pressure at the test section end with respect to r_e.

4.3.6 Best fit results

The results corresponding to the best fit model parameters (the same as those used in cases 6 (unsat), G1 (unsat), G2 (unsat) and G3 (unsat) of the 2D axisymmetric model) are summarized in Figure 4-26.

- Part a) shows the comparison of the evolution of the computed effective fluid pressure $p^* = \max(p_l, p_g)$ with the evolution of sensor M-PEFloor (located at the bottom of the test section, close to the megapacker). It may be appreciated that the computed evolution reproduces the main features of the measured response, but there is an increasing trend in the evolution of pressures that could not be modelled.

- Part b) shows the evolution of the computed evolutions of the liquid phase and gas phase pressures. It may be seen that the considered point remains saturated ($p_l \geq p_g$) during the liquid injection tests, but desaturates ($p_l < p_g$) during the gas injection tests.

- Part c) shows the evolution of the intrinsic permeability at the considered point. Note that the large observed variations of about one order of magnitude are an important feature of the model.

From these results, we may consider the 1D simplified model as suitable for modelling the HG-A test.

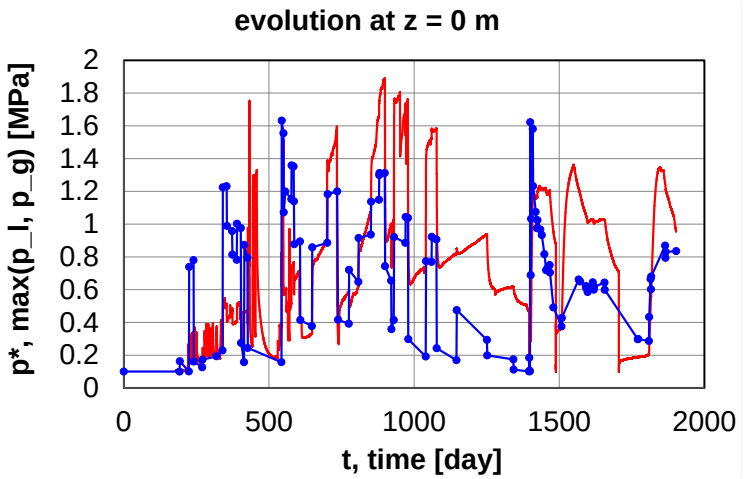

a)

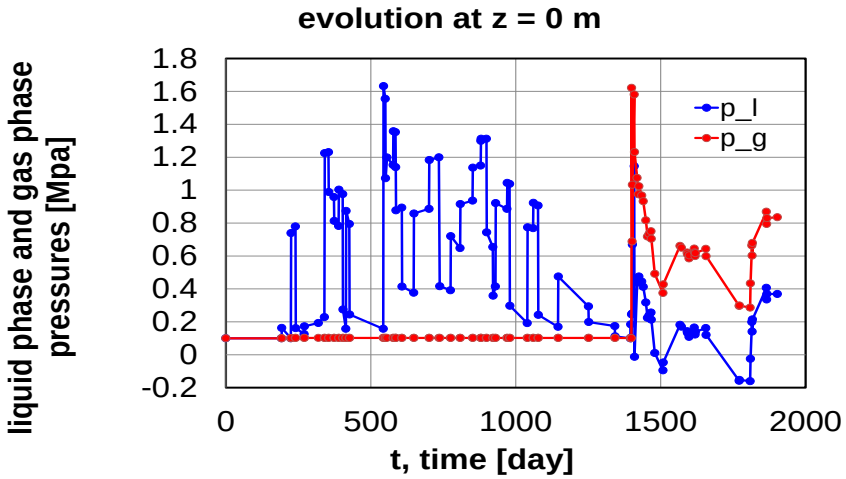

b)

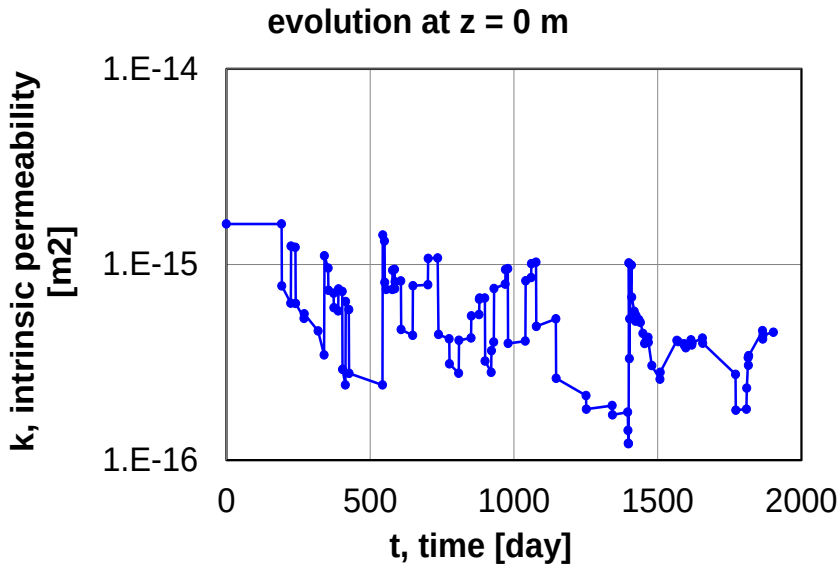

c)

Figure 4-26. Evolutions at the megapacker end close to the test section of: a) effective fluid pressure (blue) and sensor M-PEFloor (red); b) liquid phase pressure (red) and gas phase pressure (red); and c) intrinsic permeability.

4.3.7 Comparison with 2D axisymmetric model

It is of interest to compare the results obtained using the 1D simplified model with the results obtained using the 2D axisymmetric model. If results using both models are similar (thereby providing a cross check of these models), then the pertinence of the additional simplifying assumptions made to obtain the 1D simplified model is validated.

Using the 1D simplified model and the 2D axisymmetric model, Figure 4-27 shows the evolution of the liquid phase pressure at the test section and Figure 4-28 shows the evolution of the intrinsic permeability in the EDZ, close to the contact between the megapacker end the tests section. It may be seen that the results using both models are similar, at least during the considered time period.

On the other hand, Figure 4-29 shows the distributions of displacements, strains and volume flow of the liquid phase around the megapacker half close to the test section at day 900 (hydraulic tests) obtained using the 2D axisymmetric model. It is apparent that, except for a small zone close to the megapacker end, the aforementioned additional simplifying assumptions tend to be appropriate, that is: (1) displacements are radial in the EDZ and in the (undamaged) Opalinus clay (to a lesser extent); (2) plain strain conditions in the EDZ and in the (undamaged) Opalinus clay; and (3) volume flow of the liquid phase is parallel to the tunnel axis in the EDZ and zero (undrained conditions) in the (undamaged) Opalinus clay.

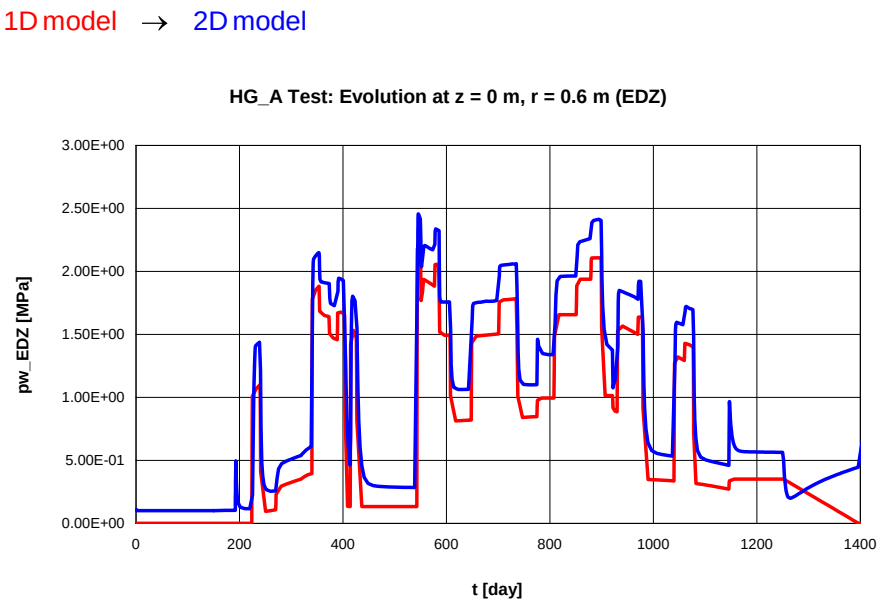

Figure 4-27. Evolution of the liquid phase pressure at the test section.

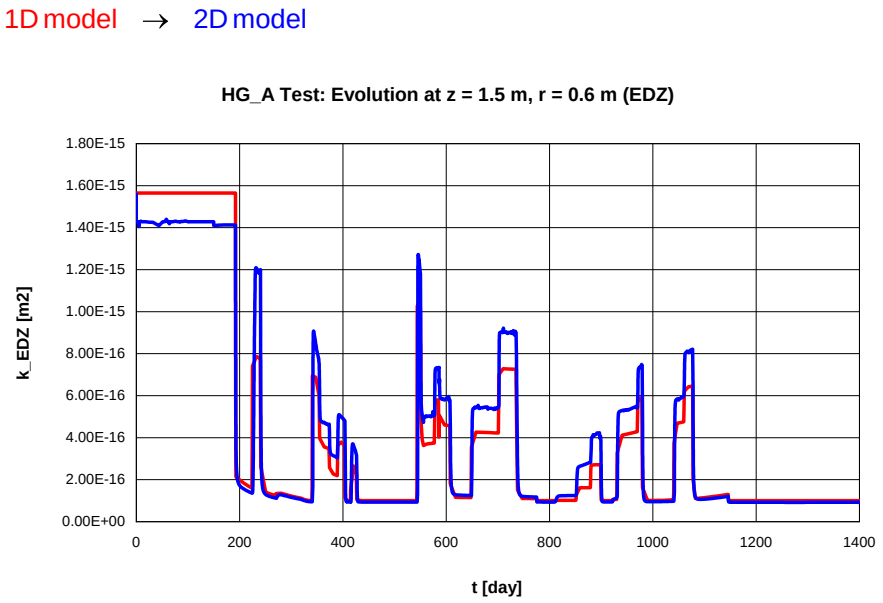

Figure 4-28. Evolution of the intrinsic permeability in the EDZ, close to the contact between the megapacker and the test section.

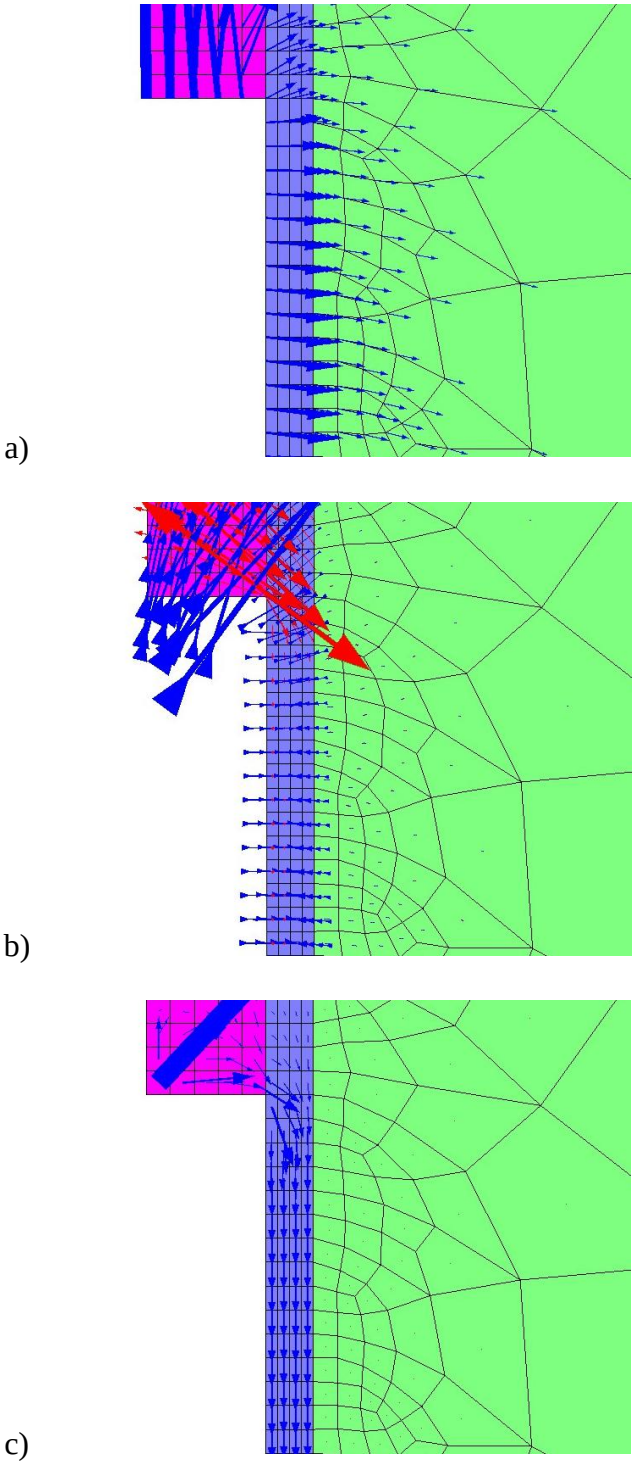

Figure 4-29. Results of the 2D axisymmetric model at day 900 (hydraulic tests) on the zone around the megapacker half close to the test section: a) displacements (radial); b) strains (plane strain); and c) volume flow of liquid phase (axial on EDZ, zero on the (unsamaged) Opalinus clay).

5 Conclusions

The modelling of the HG-A in situ test has been done using the general framework of multiphase flow in deformable porous media. Two main aspects have been addressed: the excavation of the tunnel and the liquid and gas injection tests. For the tunnel excavation, a 3D model has been made using CODE_BRIGHT. For the liquid and gas injection tests, two models have been made: a 2D axisymmetric model using CODE_BRIGHT and a 1D simplified model implemented in an Excel spreadsheet.

- **3D model.** The model considers saturated conditions and a linear cross-anisotropic poroelastic material with cross-anisotropic constant permeability, whereby the isotropy planes were parallel to the bedding planes of the Opalinus clay. The model has been able to reproduce the main features of the observed liquid phase pressure evolution (with a fast increase during the tunnel excavation and a subsequent decrease due to liquid drainage) and the zones with largest predicted increases of porosity coincided quite well with the zones of greatest damage observed in the EDZ.

- **2D axisymmetric model.** The model considers axisymmetry about the tunnel axis, and isotropic and homogeneous poroelastic behaviour for the EDZ (with a constant thickness), the (undamaged) Opalinus clay and the gravel in the test section. These assumptions imply that the model considered an average behaviour of the EDZ. An important feature of the model is a deformation-dependent intrinsic permeability in the EDZ. The model has been able to reproduce the observed general features of the liquid phase pressure evolution at the test section during the years of test operation. However, some features have not been satisfactorily reproduced and would require a more detailed knowledge of the geometry and material behavior of the EDZ. Aspects such as the initial saturation of the test section and the elimination of gas entrapped in the test section have been analyzed using the model.

- **1D simplified model.** The model considers additional simplifying assumptions with respect to the 2D axisymmetric model. In essence, it is assumed that slices perpendicular to the tunnel axis can move independently and in plane strain but they are hydraulically (liquid and gas) connected. Constitutive relations are the same as in the 2D axisymmetric model, in particular the deformation-dependent intrinsic permeability in the EDZ. The model provides results similar to the 2D axisymmetric model, which also shows the pertinence of the additional simplifying assumptions for the modeling of the HG-A test, thereby allowing gaining insight into the HG-A test. The model has been used to carry out sensitivity analyses with respect to model parameters, which proved helpful in the calibration of the 2D axisymmetric model.

The comments concerning the 2D axisymmetric model and the 1D simplified model can be illustrated graphically. In Figure 5-1 the evolutions of the liquid phase pressure in the test section and of the intrinsic permeability in the EDZ close to the contact between the megapacker and the test section obtained both using the 2D axisymmetric model and the 1D simplified model are compared. Note the similarities of those results and the large variations in the evolution of the intrinsic permeability in the EDZ. Finally, Figure 5-2 highlights the increasing trend in the evolution of the liquid pressure in the test section, which could not be reproduced.

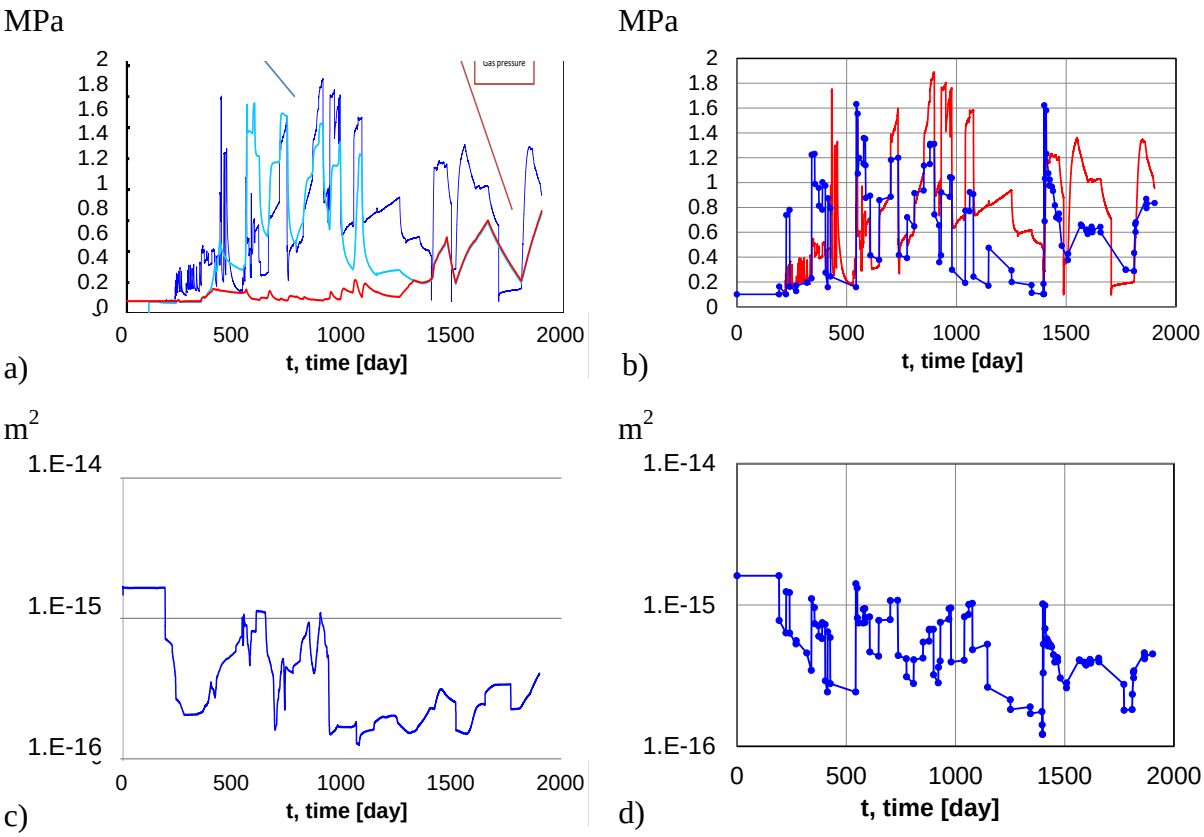

Figure 5-1. Evolutions near the contact of EDZ with the test section and the megapacker: a) 2D axisymmetric model: sensor M-PEFloor (dark blue), liquid phase pressure (light blue), gas phase pressure (red); b) 1D simplified model: sensor M-PEFloor (red), effective fluid pressure (blue); c) 2D axisymmetric model: intrinsic permeability; and d) 1D simplified model: intrinsic permeability.

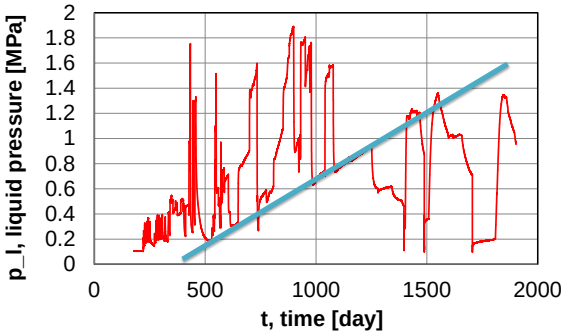

Figure 5-2. The observed increasing trend (blue line) in the evolution of pressure measured by sensor M-PEFloor (red) could not be reproduced.

6 References

[1] Alcoverro, J. Olivella, S., Alonso, E.E. (2012) Basic Formulation for Modelling Water and Gas Flow through the EDZ. Application to HGA in situ Test. D4.12 Progress report – definition of constitutive laws and initial simulations. FORGE EU-FP7 PROJECT.

[2] Lanyon, G.W., Marschall, P., Trick, T., de La Vaissière, R., Shao, H., Leung, H. (2008) Hydromechanical Evolution and Self-Sealing of Damage Zones around a Microtunnel in a Claystone Formation of the Swiss Jura Mountains. American Rock Mechanics Association ARMA 09-333.

[3] Marschall, P., Distinguin, M., Shao, H., Bossart, P., Enachescu, C., Trick, T. (2006) Creation and Evolution of Damage Zones Around a Microtunnel in a Claystone Formation of the Swiss Jura Mountains. SPE International, SPE-98537-PP.

[4] Marschall, P., Horseman, S., Gimmi, T. (2005) Characterisation of Gas Transport Properties of the Opalinus Clay, a Potential Host Rock Formation for Radioactive Waste Disposal. Oil & Gas Science and Technology – Rev. IFP Vol. 60, No. 1, pp. 121-139.

[5] Marschall, P., Trick, T., Lanyon, G.W., Delay, J., Shao, H. (2008) Hydro-Mechanical Evolution of Damaged Zones around a Microtunnel in a Claystone Formation of the Swiss Jura Mountains. American Rock Mechanics Association ARMA 08-193.

[6] Olivella, S., Alonso, E.E. (2008) Gas flow through clay barriers. Géotechnique 58, No. 3, 157-176.

[7] Olivella, S., Carrera, J., Gens, A., Alonso, E.E. (1994) Nonisothermal Multiphase Flow of Brine and Gas through Saline Media. Transport in Porous Media 15, 271-293.

[8] Trick, T., Marschall, P., Rösli, U., Lettry, Y., Bossart, P., Enachescu, C. (2007) Instrumentation for a gas path through host rock and along sealing experiment. FMGM 2007: Seventh International Simposium on Field Measurements in Geomechanics, ASCE.